1-1-2006

A numerical study of free convective heat transfer in a double-glazed window with a between-pane Venetian blind

Tony Avedissian
Ryerson University

A NUMERICAL STUDY OF FREE CONVECTIVE HEAT TRANSFER IN A DOUBLE-GLAZED WINDOW WITH A BETWEEN-PANE VENETIAN BLIND

by

Tony Avedissian

Bachelor of Engineering (B.Eng.)

Ryerson University, Toronto, 2004

A thesis

presented to Ryerson University

in partial fulfillment of the

requirements for the degree of

Master of Applied Science

in the Program of

Mechanical Engineering

Toronto, Ontario, Canada, 2006

AUTHOR'S DECLARATION

I hereby declare that I am the sole author of this thesis. I authorize Ryerson University to lend this thesis to other institutions or individuals for the purpose to scholarly research.

I further authorize Ryerson University to reproduce this thesis by photocopying or by other means, in total or in part, at the request of other institutions or individuals for the purpose of scholarly research.

BORROWER

Ryerson University requires the signature of all persons using or photocopying this thesis.

Please sign below, and give address and date.

ABSTRACT

A Numerical Study of Free Convective Heat Transfer in a Double-Glazed Window with a Between-Pane Venetian Blind

Tony Avedissian, M.A.Sc., 2006
Department of Mechanical Engineering, Ryerson University

The free convective heat transfer in a double-glazed window with a between-pane Venetian blind has been studied numerically. The model geometry consists of a two-dimensional vertical cavity with a set of internal slats, centred between the glazings. Approximately 700 computational fluid dynamic solutions were conducted, including a grid sensitivity study. A wide set of geometrical and thermo-physical conditions was considered. Blind width to cavity width ratios of 0.5, 0.65, 0.8, and 0.9 were studied, along with three slat angles, 0° (fully open), ±45° (partially open), and 75° (closed). The blind to fluid thermal conductivity ratio was set to 15 and 4600. Cavity aspect ratios of 20, 40, and 60, were examined over a Rayleigh number range of 10 to 10^5, with the Prandtl number equal to 0.71. The resulting convective heat transfer data are presented in terms of average Nusselt numbers. Depending on the specific window/blind geometry, the solutions indicate that the blind can either reduce or enhance the convective heat transfer rate across the glazings. The present study does not consider radiation effects in the numerical solution. Therefore, a post-processing algorithm is presented that incorporates the convective and radiative influences, in order to determine the overall heat transfer rate across the window/blind system.

ACKNOWLEDGEMENTS

The author of this thesis would like to express his sincerest appreciation for Dr. David Naylor. His invaluable input and guidance led to the successful completion of this thesis. His knowledge and enthusiasm provided ongoing motivation, and a sense of greater responsibility as an Engineer. Also, the author would like to thank Dr. Paul Walsh for his assistance with the computational fluid dynamics setup.

The author would like to acknowledge the support of the Natural Sciences and Engineering Research Council of Canada.

The author wishes to thank his family who has given ongoing support and encouragement. Also, a special thanks to Rossanna for her love and support during the course of this thesis.

TABLE OF CONTENTS

LIST OF TABLES

LIST OF FIGURES

Figure Title **Page**

NOMENCLATURE

Symbol	Description
A	Cavity aspect ratio
A_g	Glazing area [m^2]
Bi	Biot number
Br	Brinkman number
c	Constant
c_b	Blind curvature [m]
c_p	Specific heat at constant pressure [J/kg K]
E	Emissive power [W/m^2]
F	View factor
g	Gravitational acceleration [m/s^2]
G	Irradiation [W/m^2]
Gr	Grashof number
h	Convective heat transfer coefficient [W/m^{2}K]
H	Vertical cavity length [m]
H_c	Cavity height [m]
J	Radiosity [W/m^2]
k_b	Blind thermal conductivity [W/m K]
k_f	Fluid thermal conductivity [W/m K]
L	Surface length [m]
N	Number of surfaces within enclosure
n	Normal unit vector, constant
n_s	Number of slats
n_{Wc}	Number of nodes across W_c
Nu	Nusselt number
P	Slat pitch [m]
p	Pressure [N/m^2]
p'	Pressure defect [N/m^2]
Pr	Prandtl number
q	Heat transfer rate [W]
q''	Heat flux [W/m^2]
R	Thermal resistance [K/W]
Ra	Rayleigh number
r_s	Slat radius of curvature [m]
s_c	Slat tip to cold glazing spacing [m]
s_h	Slat tip to hot glazing spacing [m]

t	Slat thickness [m]
T	Absolute temperature in the flow field [K]
T_b	Blind absolute temperature [K]
T_c	Cold glazing absolute temperature [K]
T_h	Hot glazing absolute temperature [K]
T_m	Mean absolute temperature [K]
u, v, w	Velocity components [m/s]
US	Uncrossed string length [m]
U	Thermal transmittance (U-value) [W/m^{2}K]
W	Characteristic length [m]
W_b	Blind width [m]
W_c	Cavity width [m]
x, y, z	Global rectangular coordinates [m]
XS	Crossed string length [m]
y offset	Blind *y* offset [m]
W_b^{eff}	Effective blind width [m]

Greek Symbol	**Description**
α	Thermal diffusivity [m^2/s], absorptivity
β	Volumetric thermal expansion coefficient [K^{-1}]
ε	Emissivity
μ	Dynamic viscosity [N s/m^2]
ν	Kinematic viscosity [m^2/s]
ρ	Mass density [kg/m^3], reflectivity
σ	Stefan-Boltzmann constant [W/m^{2}K^4]
τ	Shear stress [N/m^2], transmissivity
Φ	Blind slat angle [Degrees]
ψ	Stream function [m^2/s]
λ	Wavelength [μm]

Subscript	**Description**
1 to 4	Surface designation
b	Blind
b-c	Blind to cold glazing
c	Cavity, cold glazing
cond	Conduction
conv	Convection

ew	End-wall
f	Fluid
g	Glazing
h	Hot glazing
h-b	Hot glazing to blind
h-c	Hot glazing to cold glazing
j, k	Surface indices
net	Net energy balance
rad	Radiation
ref	Reference
s	Slat
Wb	Blind width as characteristic length
Wc	Cavity width as characteristic length

Superscript	**Description**
*	Dimensionless quantity
corr	Corrected
crit	Critical
eff	Effective
est	Estimate
i	Iteration level
loc	Local
m, n	Constants
max	Maximum
MZI	Experimental using MZI
num	Numerical
SM	Simplified Model

Abbreviations

ASHRAE	American Society of Heating, Refrigerating and Air-Conditioning Engineers
CFD	Computational fluid dynamics
CFL	Courant-Friedrichs-Levy number
CSA	Canadian Standards Association
CV	Control volume
GHP	Guarded heater plate

GIS	Grid interval spacing
IGU	Insulated glazing unit
IND	Independent
low-e	Low-emittance
LTP	Linear temperature profile
MZI	Mach-Zehnder interferometer
NFRC	National Fenestration Rating Council
PDE	Partial differential equation
S2S	Surface-to-surface
SHG	Solar heat gain
ZHF	Zero heat flux

1

GENERAL REVIEW

1.1 Introduction

The importance of energy conservation and efficiency has become a great concern to society. In most building structures, large amounts of heat gain in the summer and heat loss in the winter have added to energy consumption and costs. Windows are the weakest heat insulators and can make up a large portion of a building's perimeter wall. As a result, the topic of thermal performance of windows is receiving increasing attention from researchers. This research has led to further technological advancements in the fenestration industry.

The thermal performance of a window or an insulated glazing unit (IGU) is rated on the ability to restrict the transfer of energy in the form of heat. This is a measure of the thermal transmittance or U-value. The U-value is the overall heat transfer coefficient for the entire system. It is defined as follows:

$$U_{IGU} = \frac{1}{A_g R_{IGU}} \tag{1.1}$$

where A_g is the glazing area and R_{IGU} is the total thermal resistance of the IGU, defined as:

$$R_{IGU} = \frac{(T_h - T_c)}{q_{IGU}} \tag{1.2}$$

where q_{IGU} is the heat transfer rate across the IGU, with a glazing temperature difference of $(T_h - T_c)$.

Studies have led to the improvement of the thermal insulation or the reduction in the U-value of glazing systems. Various features, such as multi-glazed units, spectrally selective low-emittance (low-e) coatings, and low thermal conductivity cavity fill-gases have been considered [1]. Multi-glazed units form a sealed cavity which is filled with an insulating gas, forming an insulated glazing unit. The fill-gas is typically air, argon, or krypton. The latter two heavier monatomic gases have a lower thermal conductivity than air, making them better insulators. The low-e coating reduces the emissivity of the radiating glazing surface. Some coatings consist of an extremely thin (transparent in the visible spectrum) metallic oxide. These are called *pyrolytic* coatings. A *sputtered* coating consists of a thin layer of pure metal that is sprayed only on the inner glazing surface of the cavity. Incorporating some of these advanced features can significantly improve the energy-saving performance of windows.

Commercial software is available for window design. VISION [2] is used by the Canadian Standards Association (CSA), and WINDOW [3] is used by the National Fenestration Rating Council (NFRC). These programs determine the one-dimensional heat transfer by simulating various environmental conditions for a variety of glazing systems. The program provides the user with a U-value and a solar heat gain (SHG) coefficient.

The chapter on window analysis in the ASHRAE Fundamentals Handbook [1] describes an ideal fenestration unit as a system that is able to permit optimum light, heat transmission, and visibility, while minimizing moisture and sound transfer between the exterior and the interior, and producing a suitable physiological and psychological environment. Adding to this, in extreme winter conditions, the accumulation of condensation and frost on the indoor surface should be kept to a minimum.

Studies show that the use of a shading device, such as a Venetian or horizontal louvered blind, will improve the thermal performance of a window, and provide control over the SHG and privacy. Several manufacturers offer window designs with between-pane Venetian blinds, where the blind is located between the two glass panes inside the enclosed cavity of the window. Many of these windows that are found on the market appear to be designed more based on aesthetics rather than for peak thermal performance.

This study deals with the thermal and hydrodynamic interaction of a double-glazed window with a between-pane Venetian blind. The blind is composed of an array of evenly spaced slats. Figure 1.1 exemplifies a typical three-dimensional model, and Figure 1.2 shows its cross-section. There have been some studies done on windows with between-pane blinds. However, for window design purposes, the available information is limited. At present, the thermal interaction between the blind and the window is not well understood and is difficult to predict. Consequently, neither software, VISION nor WINDOW, can incorporate shading devices in their calculation of U-value. The main difficulty lies in determining the heat transfer by free convection, which is heavily influenced by the blind.

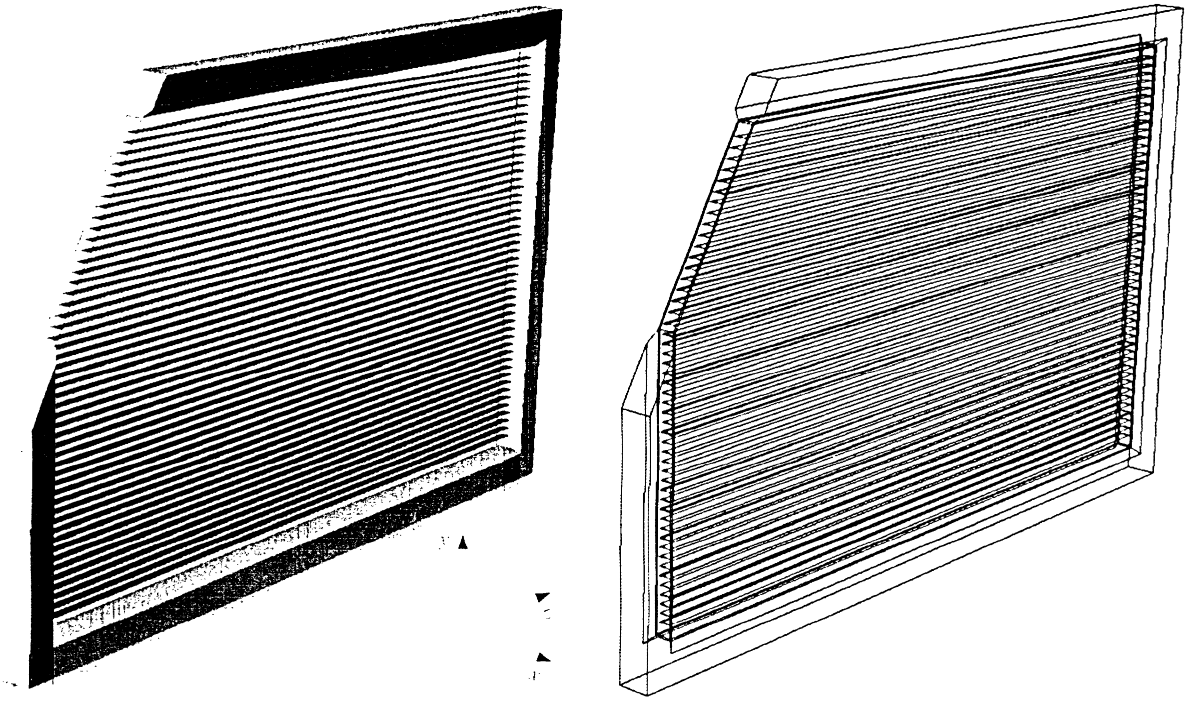

Figure 1.1: A three-dimensional model of an in frame double-glazed window with a between-pane blind

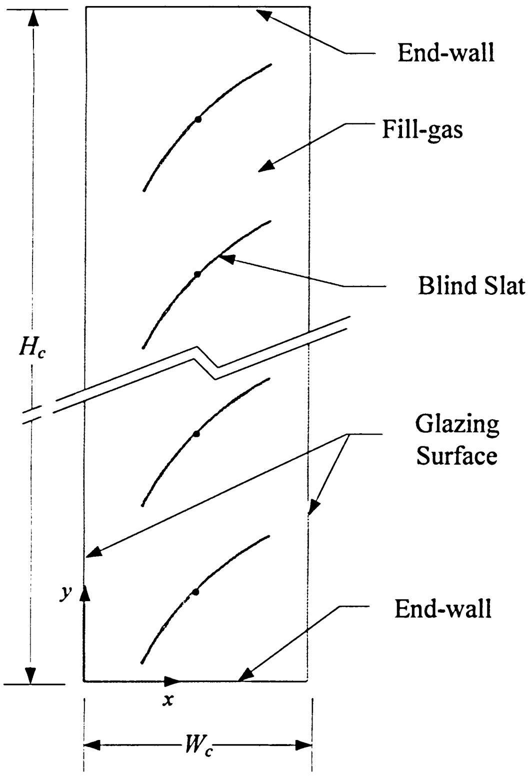

Figure 1.2: A cross-section of a double-glazed window with a between-pane blind (no frame or glazing)

1.2 Buoyancy-Driven Flow

Free or natural convection is a result of buoyancy-driven flow. Flow is initiated when an uneven concentration of density is in the presence of a gravitational field. The density variation is a result of a temperature difference in the fluid. Therefore, the driving force is subjected on the fluid body. Buoyancy-induced flows are a conjugate fluid mechanic and heat transfer phenomenon. They are particularly complex because of the fundamental coupling between the flow and heat transport.

1.3 Dimensionless Numbers

The dimensionless numbers involved in free convection are briefly reviewed in order to establish their significance and relation. The four main dimensionless numbers are: Grashof number (Gr_W), Prandtl number (Pr), Rayleigh number (Ra_W), and Nusselt number (Nu_W).

The buoyancy forces on the fluid are opposed by the viscous forces within the fluid. The dimensionless Grashof number characterizes the ratio of these two opposing forces and defines the strength of the body-force on the fluid, which is proportional to the flow strength (flow rate). The Grashof number is analogous to the Reynolds number for a forced convection problem. It is defined as follows:

$$Gr_W = \frac{\beta g (T_h - T_c) W^3}{\nu^2} \tag{1.3}$$

where β is the volumetric thermal expansion coefficient, g is the gravitational acceleration, W is the characteristic length, and $\nu \equiv \mu / \rho$ is the kinematic viscosity.

The Prandtl number is a dimensionless fluid property that characterizes the relative effectiveness of momentum and heat transport by diffusion in the velocity and thermal boundary layers, respectively. The Prandtl number is defined as follows:

$$Pr \equiv \frac{\mu c_p}{k_f} \equiv \frac{\nu}{\alpha} \tag{1.4}$$

where $\alpha \equiv k_f / \rho c_p$ is the thermal diffusivity of the fluid.

The Rayleigh number is the product of the Grashof number and the Prandtl number, and is defined as follows:

$$Ra_W = Gr_W \, Pr = \frac{g\beta\left(T_h - T_c\right)W^3}{\nu\alpha} \tag{1.5}$$

It expresses the strength of the body-force on the fluid and could be used to determine the onset of unsteady flow.

The Nusselt number is a dimensionless number that characterizes the ratio of heat transferred by convection to the heat transfer that would occur by conduction alone in a quiescent fluid. It is defined as follows:

$$Nu_W = \frac{q_{conv}}{q_{cond}} = \frac{hW}{k_f} \tag{1.6}$$

where $q_{conv} = h A_g (T_h - T_c)$, $q_{cond} = k_f A_g \partial T/\partial x$, h is the convective heat transfer coefficient, and k_f is the fluid thermal conductivity evaluated at the mean temperature: $T_m = (T_h + T_c)/2$. The Nusselt number is heavily influenced by the above dimensionless quantities. Their relation is further discussed in Chapter 2.

1.4 Literature Review

The geometry of a double-glazed window is basically a tall (vertical) rectangular cavity. Heat transfer by natural convection in these cavities is highly complex and yet fundamental; therefore, it has been extensively researched [4, 5] and forms the basis of this study. A blind placed near the indoor surface of a window has also been researched and is of interest to the current study. Preliminary studies of a between-pane blind are also reviewed. The major theoretical, experimental, and numerical findings are outlined below.

1.4.1 Natural Convection in Tall Enclosures

A double-glazed window consists of two parallel glass panes that are separated by edge-spacers or end-walls. As mentioned, the fill-gas is sealed inside the cavity between the two glazings, forming an IGU. Because of a temperature difference in the two glazings, convection is induced causing a recirculating flow. Since the force of gravity is acting downward, for a vertically arranged cavity, the gas near the hotter pane is forced upward while the gas near the colder pane is forced downward. The cavity aspect ratio, A (H_c / W_c), considerably influences the heat transfer rate, mainly below a value equal to 10. For a fixed glazing temperature, as the cavity width is increased, the conductive heat transfer rate is reduced, but the advective heat transfer rate or the strength of the flow is increased. Clearly, there is an optimum gas-layer thickness. Of course, the thermo-physical properties of the fill-gas and the magnitude of the temperature difference also influence the strength of the buoyancy-driven flow. As mentioned, these parameters combine to form the Rayleigh number. The *conduction*, *transition*, and *boundary layer* are the three consecutive flow regimes that describe the dominant mode of heat transfer. The three regimes progressively induce greater convective heat transfer across the cavity [6].

For the conduction regime, the temperature difference across the air layer is small. This regime occurs below $Ra_{Wc} \approx 6\times10^3$, and is a function of the cavity aspect ratio. Even though a weak primary circulating flow develops, the temperature profile across the cavity is linear, and the vertical temperature gradient is approximately equal to zero. For this regime, the average Nusselt number (Nu_{Wc}) is equal to one. For all other regimes, the average Nusselt number is always greater than one. The optimum cavity width (or gas-layer thickness) is found to be near the shift from the conduction to the transition regime ($7000 < Ra_{Wc} < 10^4$). In the lower range of these Rayleigh numbers, secondary flows, which co-rotate with the primary flow, develop in the core region. In the upper range, the secondary flows become unstable [7].

If the temperature difference increases, resulting in a higher Rayleigh number in the range of $10^4 < Ra_{Wc} < 5 \times 10^4$, the transition regime is reached. In this regime, the primary circulating flow strengthens and the two increasingly independent boundary layers develop along the glazings. The boundary layer thickness is proportional to $Ra_{Wc}^{-1/4}$. The heat transfer is now a combination of approximately equal amounts of conduction across the core and convection in the boundary layers. The secondary flows within the core are now chaotic and fully turbulent. In this regime, the Nusselt number is independent of cavity aspect ratio. [8]

At a Rayleigh number slightly greater than 5 x 10^4, the boundary layer regime is reached. The boundary layers become more distinct from the core region, where their thickness is proportional to $Ra_{Wc}^{-1/3}$. The mode of heat transfer is dominantly convective, due to the thinning boundary layer flow, resulting in a weaker conduction across the core. Therefore, the horizontal temperature gradient is much higher in the two boundary layers than in the core. Because the boundary layer regime transfers a higher amount of heat across the cavity, it is of interest to the window designer to hinder this regime, possibly by the inherent flow inhibiting effects from the use of shading devices.

As the Rayleigh number further increases past 5 x 10^4, hydrodynamic instabilities arise in the boundary layers. At a higher Rayleigh number, a time-dependant unsteady flow is initiated and eventually turbulent boundary layers develop. In very tall and narrow cavities, the flow can become turbulent immediately after the conduction regime, without making a transition to the laminar boundary layer regime [6]. Unstable flow generally results in an enhancement in the convective heat transfer.

For a tall vertical rectangular enclosure, Korpela et al. [8] have developed a correlation that predicts the onset of secondary recirculating flow, as follows:

$$Gr_{Wc}^{crit} = 8000\left(1+\frac{5}{A}\right) \tag{1.7}$$

where Gr_{Wc}^{crit} is the critical Grashof number and A is the cavity aspect ratio of the enclosure. The recirculating secondary flow within the core region is contained and driven by the primary recirculating flow. In large aspect ratio enclosures, it has been observed that the transition to unsteady flow in the core region starts at a Grashof number slightly higher than the critical Grashof value [7, 9].

Figure 1.3 illustrates the temperature contours obtained from a Mach-Zehnder laser interferometer (MZI) by Lai [10], for a cavity with an aspect ratio of about 9.5. As indicated, possible (developing) secondary recirculating flows exist in the core region, because the critical Grashof number is well exceeded. Hence, the two boundary layers, which are moving in a clockwise direction, where the flow is well into the boundary layer regime. It can be seen that, near the top right corner of the cavity, a high temperature gradient exists due to the *crossover* of the hot fluid to the cold glazing side. And similarly, near the bottom left corner of the cavity, a high temperature gradient exists due the crossover of the cold fluid to the hot glazing side. During winter conditions, this is the primary cause of condensation and frost accumulation on the indoor glazing surface.

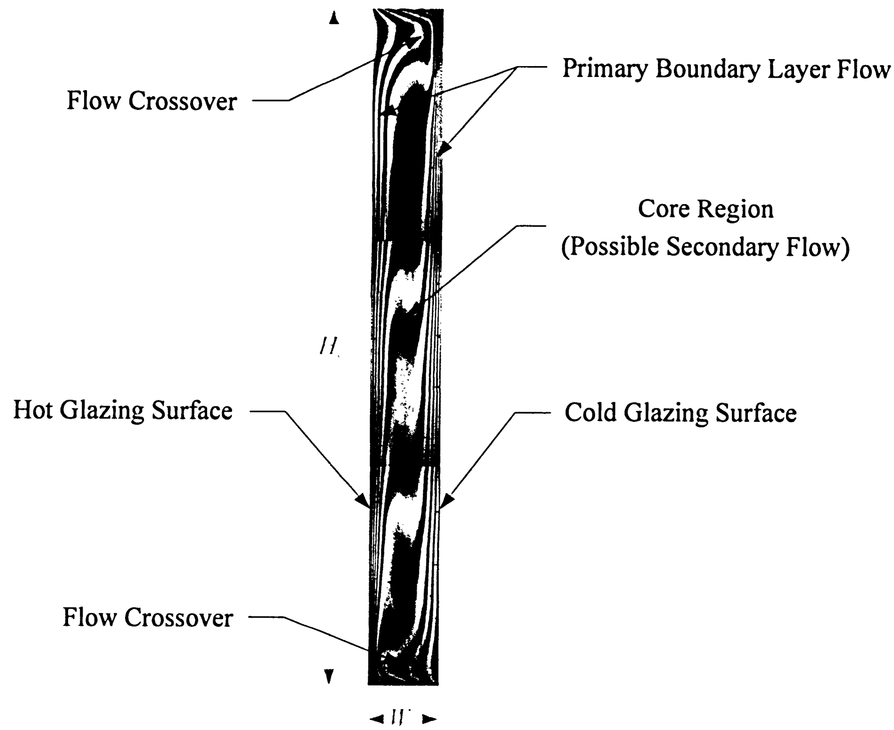

Figure 1.3: Temperature contours from a MZI apparatus, Lai [10] (Ra_{Wc} = 1.31 x 10^5, Pr = 0.71, A = 9.5)

Figures 1.4 and 1.5 show the temperature and stream function contours (defined in Section 3.8.1) for an empty cavity with an aspect ratio of 20 and 40, respectively, at a Rayleigh number of 10^5. A full cavity is shown along with an enlarged view of the top and bottom sections. At the same conditions, a higher aspect ratio cavity clearly illustrates the secondary flow in the core region. These results were obtained for qualitative purposes using a commercial computational fluid dynamics (CFD) package. The details of the numerical model are discussed in Chapter 3.

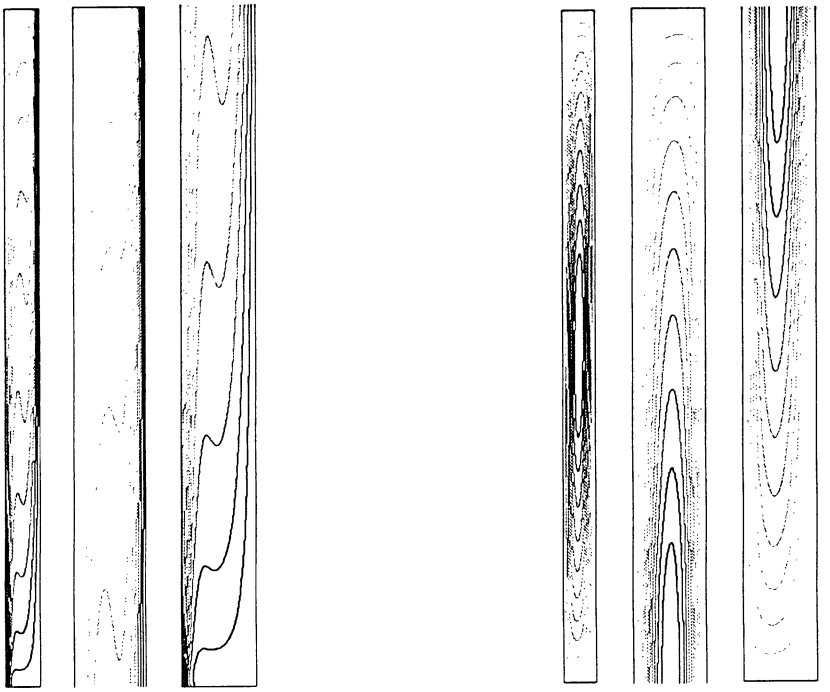

(a) T (b) ψ

Figure 1.4: (a) Temperature contours, (b) stream function contours ($Ra_{Wc} = 10^5$, $Pr = 0.71$, $A = 20$)

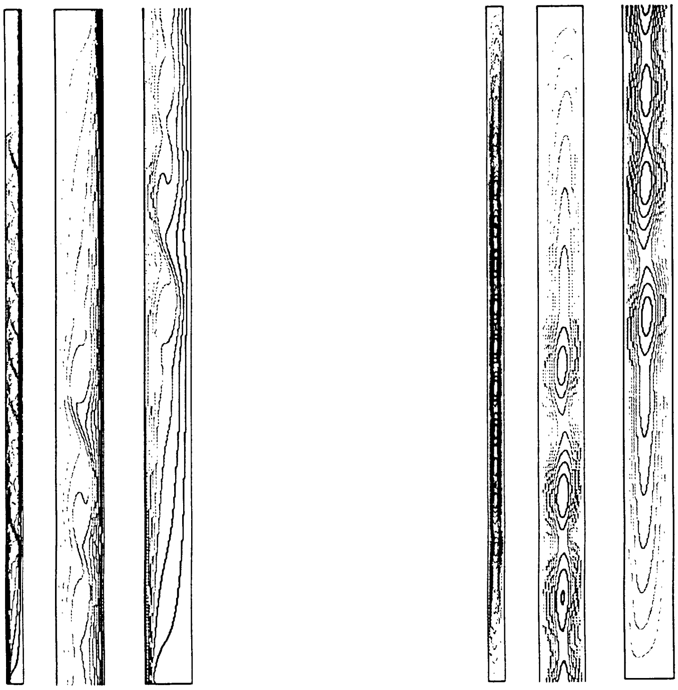

(a) T (b) ψ

Figure 1.5: (a) Temperature contours, (b) stream function contours ($Ra_{Wc} = 10^5$, $Pr = 0.71$, $A = 40$)

The temperature difference that induces the convective flow also causes long-wave ($\lambda >$ 3 μm) radiative heat exchange between the glass panes. Thermal radiation from an untreated window accounts for about two thirds of the heat transfer. Most studies consider a moderate temperature difference between the glazings ($(T_h - T_c) \leq 20$ K). At the end-walls, a zero heat flux (ZHF, adiabatic) or a linear temperature profile (LTP) is considered. In a real world situation, where glazing surfaces do not have a fixed temperature, thermal radiation is influenced by pane spacing. This is not due to participating medium effects, or the reduction in view factor, but by the increase in the Rayleigh number, which causes an increase in the convective heat transfer. Therefore, coupling between convection and radiation is important in this situation only. When considering fixed glazing temperatures, the convective and radiative heat transfers are not coupled, unless there is a thermally interacting body such as a blind. If the end-walls are set to be adiabatic, then they would also couple the two modes of heat transfer. For large aspect ratio enclosures, the coupling effect is weak.

Extensive studies show that the Nusselt number is a function of the Rayleigh number, the Prandtl number, and geometry. In this case, the geometrical influence on the Nusselt number is the cavity aspect ratio. This is expressed as follows:

$$Nu = f\left(Ra_{Wc}, Pr, A\right) \qquad (1.8)$$

For common fill-gases, the independent effect of the Prandtl number is usually ignored because it does not significantly differ from the value of about 0.71 (air at 300 K). Therefore, correlations are commonly in the form of Equation 1.9.

$$Nu = cRa_{Wc}^{m} A^{n} \tag{1.9}$$

where c is a constant, m is a fraction usually between a quarter (laminar flow) and a third (turbulent flow), and n has a magnitude similar to m, but is it negative.

The cavity aspect ratio is the parameter that is easily controlled and is of significant interest from a design perspective. ElSherbiny et al. [11] have proposed a correlation that is based on experiments carried out over a wide range of Rayleigh numbers and aspect ratios. The correlation determines the Nusselt number using the Rayleigh number and, in some cases, aspect ratio. They reported that the Nusselt number has a weak dependence on aspect ratio when the aspect ratio is greater than 25. Therefore, the Nusselt number is a function of aspect ratio for short windows, or windows with large pane spacing. The correlation is as follows:

$$Nu_{Wc1} = 0.0605 Ra_{Wc}^{1/3} \tag{1.10 a}$$

$$Nu_{Wc2} = \left(1 + \left(\frac{0.104 Ra_{Wc}^{0.293}}{1 + \left(\frac{6310}{Ra_{Wc}} \right)^{1.36}} \right)^{3} \right)^{1/3} \tag{1.10 b}$$

$$Nu_{Wc3} = 0.242 \left(\frac{Ra_{Wc}}{A} \right)^{0.272} \tag{1.10 c}$$

$$Nu_{Wc} = Max\left(Nu_{Wc1}, Nu_{Wc2}, Nu_{Wc3} \right) \tag{1.10 d}$$

where *Max* is a function that returns the largest value in a set of values.

Wright [12] developed a new correlation based on the data obtained by ElSherbiny et al. [11]. The new correlation is independent of aspect ratio and is said to be more accurate for a cavity aspect ratio greater than 40. The correlation is as follows:

$$Nu_{Wc} = 0.0673838 Ra_{Wc}^{1/3} \qquad Ra_{Wc} > 5\times10^4 \qquad (1.11\ a)$$

$$Nu_{Wc} = 0.028154 Ra_{Wc}^{0.4134} \qquad 10^4 < Ra_{Wc} \leq 5\times10^4 \qquad (1.11\ b)$$

$$Nu_{Wc} = 1 + 1.75967\times10^{-10} Ra_{Wc}^{2.2984755} \qquad Ra_{Wc} \leq 10^4 \qquad (1.11\ c)$$

Aydin [13] has done some numerical studies on the optimum air-layer thickness in double-pane windows. His findings show that as the glazing temperature difference is increased, the pane spacing should be reduced to decrease the heat transfer. This reduces the Rayleigh number, and forces a more conductive dominated heat transfer. Aydin found that the optimum glazing spacing range for $Ra = 10^9$ is 18-21 mm. For $Ra = 4\text{x}10^9$, the optimum thickness is 12-15 mm. The ASHRAE Fundamentals handbook [1] states that a cavity width greater than 13 mm has no significant effect on the centre-glass U-value. The centre-glass region is where the glazing surface (A_g) is generally isothermal.

As mentioned, many researchers have studied heat transfer in an empty cavity. The work done by Batchelor [5], Wright et al. [6, 7, 12], Korpela et al. [8], and Ostrach [14, 15] provides a detailed review.

1.4.2 Natural Convection with a Blind Adjacent to the Indoor Glazing Surface

In northern climates, most shading devices are placed adjacent to the indoor surface of a window. These devices interact with the free convective flow and shield the long-wave radiative heat exchange between the internal glazing and the indoor environment. Shading devices also reduce the short-wave ($\lambda < 3$ μm) radiative heat gain by simple blocking of the solar transmission. The beam transmission also includes reflection from the shading device. The absorbed portion of the solar irradiance that is not reflected will increase the temperature of the shading device, resulting in an increase in the *inward-flowing fraction* [16]. The decrease in the radiative heat transfer rate, due to the presence of the blind, can considerably improve occupant thermal comfort. This is of importance for *daytime* conditions.

A Venetian blind, adjacent to the indoor glazing surface, is a common form of a shading device. As a result, a lot of literature can be found on experimental and numerical studies. Some important experimental and numerical investigations were carried out in a collaborative effort to generate valuable data that can be incorporated in a window modeling program. Some of the more fundamental findings are outlined below.

Machin et al. [17, 18, 19] were the first to study the convective flow and heat transfer from a window adjacent to a Venetian blind on the indoor surface. Their experimental study was conducted using a Mach-Zehnder laser interferometer (MZI) to visualize the temperature field and to measure the local convection coefficients for several slat angles and blind to glazing spacings. They concluded that standard aluminium blinds have a strong influence on the local convective heat transfer coefficient. The average convective heat transfer rate was only slightly lower than that of an isolated plate at the same Rayleigh number. The interaction of the blind with the free convective boundary layer produced a periodic variation in the convective heat transfer coefficient (on the glazing surface) with a spatial frequency equal to the slat pitch. Also, the blind's thermal conductivity had a strong effect on the local maxima of the convective heat transfer coefficient. These maxima were presumed to also be caused by the fluid velocity increase as it passed through the reduced cross-sectional area imposed by the blind slat. Machin et al. also discovered secondary cellular flow between the louvers at slat angles of 0° and 45°.

Ye [20] has conducted a finite element numerical study of a Venetian blind next to an isothermal surface. Neither radiative heat transfer nor the curvature of the slats was considered in the model. The flat blind slats were treated as zero thickness baffles, on which the *no-slip* and impermeability conditions were applied. Ye found that the slat tip-to-glazing distance and the slat angle have a strong effect on the flow and the heat transfer. The smaller the slat tip-to-glazing distance, a stronger effect was observed. The way in which a blind is closed was also studied. Ye found a negligible difference in the U-values between positive (cold-side-up) and negative (hot-side-up) slat angles when the blind to glazing distance is large. However, at close blind to glazing spaces, the orientation of the slats has a strong influence on the average heat transfer coefficient. For the negative angle case, the average convective heat transfer coefficient was 13% lower than that of the corresponding positive angle.

In a similar study, Phillips et al. [21, 22] improved on the modeling of Ye [20] by including the effects of thermal radiation exchange, heat conduction, and curvature in the slats.

This conjugate heat transfer model showed that a blind can also provide a substantial amount of radiation shielding. The numerical results of Phillips et al. agreed well with the experimental results of Machin et al. [17, 18, 19]. It was concluded that radiation effects are significant and that a numerical model requires the incorporation of the coupled radiative heat transfer. They found that placing the blind near the window causes a decrease in the fluid velocity adjacent to the glazing, since some of the rising air must travel a tortuous path. This effect reduced the average convective heat transfer rate, however; the thermal conductivity of the blind slats enhanced the local convective heat transfer rate. The slats also produce a strong periodic variation in the local radiative heat transfer rate due to the periodic variation of the view factor blocking effect of the slats. In conclusion, for all of the parameters studied, the blind reduced the radiative heat transfer rate from the window by up to 33%, even when the louvers were in the open position. Depending on the exact conditions, it was found that the average convection coefficient could either increase of decrease. It was also discovered that the total heat transfer at the indoor glazing is strongly coupled to the radiative heat transfer to the blind and the surrounding environment.

Duarte [23], Naylor et al. [24], and Duarte et al. [25] have done an experimental interferometric study involving heated Venetian blinds in order to mimic the solar irradiance during daytime summer conditions. They concluded that as the blind slats' heat flux is increased, the glazing's heat transfer rate decreases, and in some cases becomes negative, resulting in a net heat transfer to the glazing. For an open blind, the small blind to glazing spacing had a strong influence on the (periodic) local and average heat transfer rates.

Oosthuizen et al. [26] have done work on the effect of free convective heat transfer on Venetian, vertical, and plane blinds. Their numerical analysis and the experimental results used for validation agreed well. They concluded that in the numerical modeling of Venetian and vertical blinds, it is necessary to include conduction in the slats and radiant heat transfer in the analysis. They also found that in plane blinds, there is an optimal blind to glazing spacing that yields a minimum convective heat transfer rate from a window.

Collins et al. [27, 28] have done a numerical study on the convective and radiative heat transfer on a blind that is heated to mimic solar irradiance. The convective and radiative heat transfer rates were of the same magnitude. They concluded that the radiative heat transfer can be controlled by manipulating the emissive properties of the glass and the blind. The numerical analysis was validated by experimental measurements. The local and average convective heat transfer coefficients were found to agree closely, both in magnitude and trend.

Naylor et al. [29] have also done a study on the thermal interaction between a window and a blind. Their method considers a one-dimensional heat transfer model, where the radiative heat transfer is post-processed and *recoupled* with the data from the numerical *convection-only* simulation. As the name suggests, convection-only simulations do not include radiation effects. Their findings show that the lowest blind emissivity results in the least reduction in the radiative heat flux when the blind is open. This is due to an increase in the amount of radiation that strikes the blind and reflects into the room. They reported a trade-off when the blind to glazing spacing was reduced. This improved the U-value but caused an increase in the radiative heat exchange, which could consequently affect occupant comfort level. They also reported that a low emissivity blind in the closed position reduces the overall heat transfer rate through a standard double-glazed window by as much as 37%. The blind was found to have less effect on *high performance* windows (i.e. low-e, argon fill-gas). Regular blinds reduced the radiative heat exchange with the room interior by up to 60%.

Shahid and Naylor [30] have done a similar study to Naylor et al. above [29]. A two-dimensional numerical model was developed that considered all modes of heat transfer for a single and double-glazed window. Only the centre-glass region was considered for the U-value calculations. Their findings confirmed that Venetian blinds can significantly improve the window energy-saving performance. Also, the slat tip-to-glazing spacing and the slat angle had a significant effect on the overall heat transfer rate. When the blind was placed far from the glazing, less convective interaction was observed. The best window/blind thermal performance was found when the blind was placed close to the window with the louvers in the closed position.

1.4.3 Natural Convection in a Cavity with a Between-Pane Blind

Double-glazed windows with a between-pane Venetian blind interact similarly to a blind adjacent to the indoor glazing surface in terms of the reduction in the radiative heat exchange. However, because of the complexity of the buoyancy-driven flow, a solid conclusion of the thermal performance has not been established. Some studies have been done on between-pane blinds; the more fundamental ones are outlined below.

Ye [20] has conducted a finite element numerical study of a between-pane Venetian blind. This study was done in parallel to the one mentioned in the previous section, but all modes of heat transfer where considered. Ye reported that the slat angle affects the thermal performance. When the blind is in the closed position, it blocks the long-wave radiation between the panes and in turn reduces the heat transfer.

Garnet et al. [31, 32] performed an experiment to determine the centre-glass U-values at various slat angles using a guarded heater plate (GPH) apparatus. It was reported that the blind blocks some of the long-wave radiation crossing the window cavity, even when the blind is in the open position. Also, they reported that the blind's thermal conductivity increased the heat transfer when the slat tip-to-glazing spacing was small. This effect diminished as this spacing was increased. In all cases, the window performance improved as the blind was closed. This was due to the blocking effect of the long-wave radiation, and the greater slat tip-to-glazing spacing (i.e. weak conduction effect). The hot-side-up slat orientation outperformed the cold-side-up by up to 7%. This was postulated to be due to the deflection of the primary flow around the perimeter into a secondary flow between the slats. The closer the blind tip-to-glazing spacing and the slat angle midway between the open and closed position, the more deflection was observed. The weaker the primary flow, the less local heat transfer occurred at the top and bottom of the cavity (i.e. weak crossover effect). This can improve condensation and frost resistance.

Yahoda and Wright [33] have done a theoretical study of the one-dimensional centre-glass heat transfer of a between-pane Venetian blind using correlations for an empty cavity

(Equation 1.11). The thermal radiation effect of the blind was calculated by using a six-surface enclosure that included the two glazings and the top and bottom of adjacent slats. Similar to Naylor et al. [29], the effects of the blind and the thermal radiation were later recoupled in order to have a realistic model for comparison to the experimental results of Garnet et al [31]. Despite the crude convection model, the U-values (including the glazing resistance) agreed within 10%. This shows that the convection and the long-wave radiation can be decoupled and a simple one-dimensional model can be used to determine the heat transfer rate of a window/blind system.

Naylor and Collins [34] have developed a full numerical model that considers the conjugate conduction, convection, and radiation heat transfer through the window/blind enclosure. They have numerically determined the U-value for a range of slat angles using a full CFD model and verified the results obtained from a *Simplified Model*. In the Simplified Model, similar to Naylor et al. [29], the results of a convection-only solution is obtained from the computational fluid dynamics simulation and recoupled with the thermal radiative influences determined theoretically. This Simplified Model yielded results with an accuracy that is within 1.5% of a full CFD model. The decoupling of the radiation reduced many additional variables from the problem, allowing for a more general solution. This one-dimensional radiation model is similar to Yahoda et al. [33], but considers a four surface enclosure instead of six. In the current study, simulations that do not consider radiation are referred to as a convection-only solution and simulations that consider radiation are referred to as a full (CFD) model. The Simplified Model is employed and explained in detail in Chapter 5.

Huang [35] has calculated the U-value through the centre-glass region of a window/blind enclosure using a guarded heater plate apparatus. He reported that increasing the pane spacing resulted in the improvement of the thermal performance. However, depending on some variables, the window performed better with a smaller pane spacing at large slat angles. The influence of the slat angle was less evident at a larger pane spacing. In general, the window performance always improved as the blind was closed, due to the long-wave radiation blocking. Huang found that the positive and negative slat angle orientations had a difference of about 7% on the U-value. Out of the various angles studied (0°, ±30°, ±60°, ± 75°), the positive slat angle of 60° (cold-side-up) showed the greatest amount of crossover, by the deflection of the primary flow. Huang's [35] experimental measurements are used to validate the numerical results obtained in the current study.

The recent work of Lai [10] involved a study of the convective heat transfer through the window/blind enclosure using a Mach-Zehnder laser interferometer. Three cavity widths and three slat angles were considered. It was reported that the between-pane blind has a significant effect on the local convective heat transfer rate. Also, the distribution of the local Nusselt number depends strongly on the slat angle. The variation of the cavity width clearly changed the fluid flow pattern inside the cavity. With the exception of one case, where the slat tip-to-glazing space was the smallest, the average Nusselt numbers obtained from the experiment were lower than the values computed from the correlation by ElSherbiny et al. [11], at the corresponding Rayleigh number and aspect ratio. This shows that a between-pane Venetian blind can enhance the thermal performance of a double-glazed window by reducing the convective heat transfer. Two types of flows were evident when the blind was open: a primary flow around the cavity perimeter and a secondary flow between the slats. For a small cavity width, the conduction in the slats, observed in the temperature contours, created periodic maxima in the local Nusselt number on both hot and cold glazings. Lai's [10] experimental measurements are used to validate the numerical results obtained in the current study.

1.5 Scope of Research

Because of the increasing popularity of double-glazed windows with a between-pane blind, the thermal performance of these complex fenestration systems are becoming a major engineering interest. This research is a continuation of an ongoing effort to increase energy conservation. The main objective of the current study is to determine the free convective heat transfer rate across a double-glazed window with a between-pane Venetian blind. A parametric approach is taken, where a wide range of geometrical and thermo-physical conditions is considered. A numerical method is used to solve for the convection-only heat transfer rates, which are presented in terms of Nusselt numbers. These results were studied on the notion that the radiative influences can be post-processed (recoupled), using the Simplified Model, to obtain an accurate full solution. The results from this study will help in the development of correlations which can be incorporated into fenestration thermal analysis programs. There is a need for future software release that is capable of incorporating shading devices, such as a Venetian blind, for determining a window's thermal performance. This research is part of a joint effort between Ryerson University, Queen's University, and the University of Waterloo. To the author's knowledge, an extensive study has not been done involving a wide range of parameters for a double-glazed window with a between-pane Venetian blind.

2

PROBLEM MODELING

2.1 Introduction

In order to determine the effect of the between-pane blind on the convective heat transfer rate across the cavity, a wide range of geometrical and thermo-physical conditions was selected for the parametric study. The equations that govern fluid dynamics and heat transfer were also simplified and tailored specifically for the problem at hand.

2.2 Model Geometry

The window/blind model geometry considered in this study is shown in Figure 2.1. The heat transfer is driven by the temperature difference across the isothermal and constant temperature glazings or vertical walls which are separated by adiabatic end-walls. This forms a vertical enclosure, with height H_c and width W_c, containing the fill-gas. The vertical walls are labelled T_h for the *hot* glazing and T_c for the *cold* glazing. The model assumes a unit length in the z direction (i.e. $A_g = H_c$).

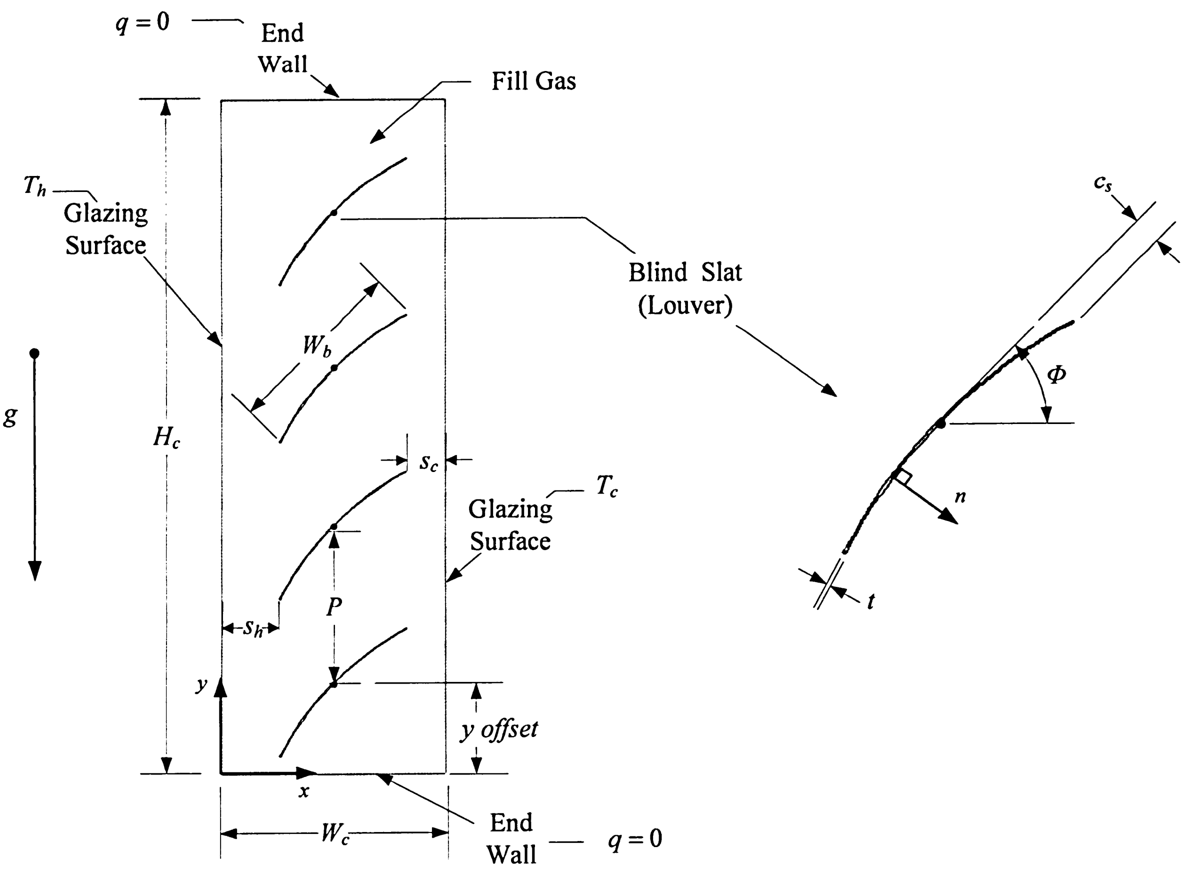

Figure 2.1: Model geometry and thermal boundary conditions

The blind is comprised of louvers or slats which are centred at their pivot points between the vertical glazings. The slats have a width W_b, curvature c_s, thickness t, are spaced with pitch P, and rotatable about their centre at angle Φ. The number of slats, n_s, depends on the height of the cavity and the slat width. It is defined by the following expression:

$$n_s = Int\left(\frac{H_c - 2(y\,offset)}{P+1}\right) \tag{2.1}$$

where *Int* is a function that rounds a number down to the nearest integer, and P is defined as:

$$P = \frac{7}{8} W_b \tag{2.2}$$

This is a common slat pitch for a commercial Venetian blind. The slat curvature and thickness were also set as a function of blind width in order to obtain typical curvature and thickness values:

$$c_s = 0.075 W_b \tag{2.3}$$

$$t = 0.0075 W_b \tag{2.4}$$

The *y offset* value has been set such that when the blind is rotated to the closed position ($\Phi \approx 75°$), a seal is created with the bottom end-wall:

$$y\ offset \approx \frac{W_b}{2} \tag{2.5}$$

2.3 Parameters

When a blind is placed in a cavity, the thermal and hydrodynamic complexity of the system is greatly increased. As shown in Figure 2.2, the blind is involved in all three modes of heat transfer:

1. Conductive heat transfer in the blind slats.
2. Convective heat transfer due to the blind's interaction with the flow.
3. Radiative heat transfer due to blocking as a result of the blind (in a full CFD solution).

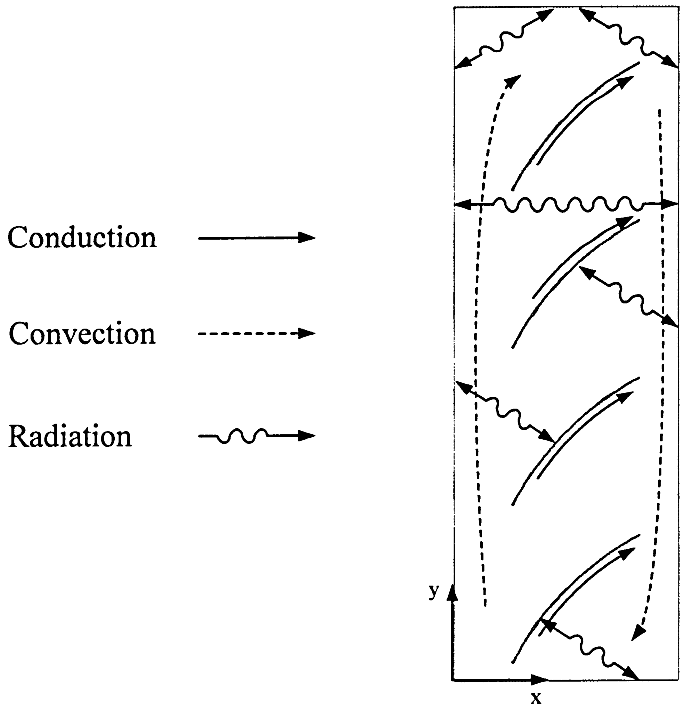

Figure 2.2: Modes of heat transfer in a window/blind system

Using dimensional analysis, the parameters hypothesized to be the most influential on the Nusselt number for a window/blind system are as follows:

$$Nu_{Wc} = f\left(Ra_{Wc},\ Pr,\ H_c/W_c,\ W_b/W_c,\ k_b/k_f,\ \Phi\right) \tag{2.6}$$

where H_c / W_c is the cavity aspect ratio, W_b / W_c is the blind width to cavity width ratio, k_b / k_f is the blind to the fluid thermal conductivity ratio, and Φ is the slat angle. All geometrical lengths have been non-dimensionalized using the cavity width (W_c) as the scaling length. The curvature, c_s, and thickness, t, have been omitted from Equation 2.6. The curvature is believed to have a small effect on the flow and the average Nusselt number. When t is a linear function of W_b, it has a very small effect on the blind's thermal resistance, R_b, and the average Nusselt number. This can be demonstrated in one-dimension (longitudinal) as follows:

$$R_b = \frac{W_b}{k_b t} = \frac{W_b}{k_b\left(0.0075 W_b\right)} = \frac{1}{0.0075 k_b} \qquad (2.7)$$

A range of Rayleigh numbers has been considered in order to vary the body force on the fluid: 10 to 10^4 for simulating a conduction dominated regime, and 10^4 to 10^5 for a convection dominated regime. For the same fill-gas and cavity width, this simulates a range of glazing temperature differences or weather conditions. As mentioned above, for common gases, the Prandtl number is usually near 0.71 for typical average window fill-gas temperatures; therefore, only one Prandtl number has been considered. Three typical cavity aspect ratios have been chosen: 20, 40, and 60. The range of 0.5 to 0.9 has been considered for the blind width to cavity width ratios, which is the most important geometrical dimension. Two typical blind to fluid thermal conductivity ratios were studied: $k_b / k_f = 4600$ for aluminium to air [18], $k_b / k_f = 15$ for plastic to air. The results from the relatively low k_b / k_f ratio can also be used to determine the non-conductive effects of the blind. Three louver angles were studied: 0° (fully open), 45° (partially open), and 75° (closed, but not sealed). The range of the above values is fairly common for a window/blind system. Table 2.1 lists the parameters considered.

Table 2.1: Parameters considered in present numerical study

Ra_{Wc}	10, 100, 1000, 10^4, 2×10^4, 4×10^4, 10^5
Pr	0.71
H_c / W_c	20, 40, 60
W_b / W_c	0.5, 0.65, 0.8, 0.9
k_b / k_f	15, 4600
Φ **[degrees]**	0°, ± 45°, 75°

The blind couples the conductive, convective, and radiative heat transfer of the system. The coupling occurs because the blind's temperature is interactively influenced by all three modes. The long-wave radiative heat transfer, which occurs between all surfaces within the cavity, was not included in the convection-only CFD solution. As mentioned in Section 1.4.3, using a post-processing method, the radiative heat transfer can be recoupled into the convection-only solution to obtain a full solution [34]. The details of this method are further discussed in the Chapter 5. The current study only deals with *nighttime* conditions, where no incident solar irradiation is considered. Therefore, the solar heat gain equals zero in the total heat transfer equation:

$$q_{IGU} = U_{IGU} A_g (T_h - T_c) \tag{2.8}$$

2.4 Physical Model Formulation

Conventionally, the governing equations that define fluid dynamics and heat transfer were simplified and tailored specifically for the problem at hand. In order to simplify these equations, typical assumptions were made in regards to: two-dimensional flow, Newtonian fluid, Boussinesq approximation, incompressible flow, viscous dissipation, physical properties, and boundary and operating conditions. Systematic generalizations should have an insignificant effect on the overall solution. The following sections will state the assumptions made and discuss their validity.

2.4.1 Two-Dimensional Flow

The fluid motion is assumed to be two-dimensional, where any hydrodynamic or thermal effects in the z direction are neglected (i.e. $w = \partial u/\partial z = \partial v/\partial z = \partial p/\partial z = \partial T/\partial z = 0$). For studies that involve natural convection in tall cavities, this is accepted and reasonable. Furthermore, the general heat transfer is in the x direction and the force of gravity driving the flow is in the y direction. Curcija [36] has done numerical work that justifies this assumption. He reported that the overall U-value between the two-dimensional and three-dimensional studies yielded a difference less than 0.1% for typical window depth to height ratios. This assumption is further acceptable for large cavity aspect ratios.

2.4.2 Newtonian Fluid

The fluid inside the cavity is assumed to be Newtonian, where the shear stress, τ, is linearly proportional to the shear rate or the velocity gradients. This assumption is well accepted for almost all gases. Equation 2.9 defines shear stress, τ, for a Newtonian fluid.

$$\tau_{xy} = \tau_{yx} = \mu\left(\frac{\partial u}{\partial y} + \frac{\partial v}{\partial x}\right) \tag{2.9}$$

where μ is the dynamic viscosity of the fluid.

2.4.3 Boussinesq Approximation – Incompressible Flow

The fluid is assumed incompressible, which naturally results in the assumption that the fluid has a constant density. This may be the case, but the density variation (due to thermal expansion) is essential and important only in the gravitational body-force term of the governing equations. The density appearing in any other term is simply held constant and assumed to have a negligible effect on the conservation of mass, momentum, and energy (heat capacity). This technique is called the Boussinesq approximation, which simplifies the solution of the governing equations.

The density in the body-force term, which is now approximated to vary linearly with temperature, is an unknown. Therefore, the energy equation is required to solve the y momentum equation (i.e. $g = g_y$). This develops the coupling between the flow and heat transport, which requires a simultaneous calculation of the governing equations. These equations are presented in Section 2.5.

For the validity of the Boussinesq approximation, the temperature difference in the hot and cold walls should be small. This is expressed as follows:

$$\beta\left(T - T_c\right) << 1 \tag{2.10}$$

where T is the temperature anywhere in the flow field and β is the volume expansion coefficient, expressed as follows:

$$\beta = -\frac{1}{\rho}\left(\frac{\partial \rho}{\partial T}\right)_{p=const} \approx \frac{1}{T_m} \tag{2.11}$$

where T_m is the mean temperature within the flow field. For an ideal gas, β defines the percent expansion per degree for an isobaric process. Gray and Giorgini [37] studied the validity of the approximation and concluded that the approximation is valid for any Newtonian fluid, where $(T - T_c) \leq 28.6°C$.

The assumption that the fluid is incompressible also implies that pressure does not have an effect on the fluid density. This is a good assumption because, in common buoyancy-driven flow, the thermal expansion effects have a greater influence on density than pressure. In buoyancy driven flow, the velocity derivatives are fairly small and result in a negligible pressure change, even at stagnation points. Further details regarding the Boussinesq approximation can be found in Oosthuizen and Naylor [38].

2.4.4 Viscous Dissipation

Viscous dissipation or frictional heating is assumed negligible; as mentioned above, the expected velocities are small compared to the temperature difference. This characteristic is defined by the dimensionless Brinkman number [39], which defines the ratio of thermal energy production to the thermal energy transport:

$$Br = \frac{\mu u^2}{k_f (T_h - T_c)} << 1 \qquad (2.12)$$

For the problem at hand, due to the small velocity differences, the Brinkman number is small and viscous dissipation is negligible.

2.4.5 Physical Properties

All thermo-physical properties of the blind and fluid are assumed constant over the temperature range of the current problem (i.e. $dc_p / dT = d\mu / dT = dk_b / dT = dk_f / dT = 0$). The error introduced in the solution is assumed to be small because the temperature differences in the flow field are small.

2.4.6 Boundary and Operating Conditions

The classical cavity model considers isothermal vertical walls and adiabatic end-walls as the boundary conditions. This idealized representation cannot perfectly mimic the complexity of a commercial real world double-glazed window. The temperature variations (frame effects) in the edge-of-glass region and the heat transfer at the end-walls have an effect on the overall heat transfer rate across the window. Curcija and Goss [40] state that the typical edge-of-glass band is taken to be 63.5 mm, which is obtained from a computer model analysis. As mentioned, the centre-of-glass region is where the glazing surface is generally isothermal and the heat transfer path is almost one-dimensional. For large glazing surface areas (long in both y and z directions) the edge-of-glass region has a small effect on the heat transfer. Typical window end-walls have a short length compared to the height of the vertical glazings. Therefore, the end-wall conductive heat gain or loss is minimal, especially for large cavity aspect ratios. Therefore, to reduce the edge-of-glass and end-wall effects on the overall heat transfer of the system, the following assumptions were made: The glazing surface is large such that the isothermal centre-of-glass region is much greater than the edge-of-glass region, and the aspect ratio of the cavity is large such that the end-wall length is much shorter than the vertical wall height.

Only laminar flow and steady solutions are considered, where time derivatives of the dependent variables are equal to zero (i.e. $\partial u/\partial t = \partial v/\partial t = \partial T/\partial t = 0$). There are no heat sources within the domain including incident solar heat gain on the blind. Finally, at all (stationary) solid to fluid interfaces, the no-slip and impermeability conditions are applied (i.e. $u = v = 0$).

2.5 Governing Equations

The governing equations that define fluid dynamics and heat transfer are based on the conservation of mass, momentum (Newton's second law of motion), and energy (first law of thermodynamics). These partial differential equations (PDE) are second-order non-linear and are required to be solved simultaneously, especially for buoyancy-driven flow (due to the coupling between the momentum and energy equations). Even for simple geometries, such as a rectangular enclosure, no exact analytical solution exists. For this reason, a numerical method is required to solve for the distribution of the dependent variables: velocity, pressure, and temperature. From the solution of these variables, other quantities, such as the convective heat transfer coefficient, can be obtained. Taking in account the assumptions made for the problem at hand, the following hyperbolic-elliptic equations were considered, where the force of gravity acts in the negative y direction [38]:

The continuity equation:

$$\frac{\partial u}{\partial x} + \frac{\partial v}{\partial y} = 0 \qquad (2.13\text{ a})$$

The momentum equations (Navier-Stokes):

$$\rho\left(u\frac{\partial u}{\partial x}+v\frac{\partial u}{\partial y}\right)=-\frac{\partial p}{\partial x}+\mu\left(\frac{\partial^2 u}{\partial x^2}+\frac{\partial^2 u}{\partial y^2}\right) \tag{2.13 b}$$

$$\rho\left(u\frac{\partial v}{\partial x}+v\frac{\partial v}{\partial y}\right)=-\frac{\partial p}{\partial y}+\mu\left(\frac{\partial^2 v}{\partial x^2}+\frac{\partial^2 v}{\partial y^2}\right)-\rho g \tag{2.13 c}$$

The energy equation:

$$\rho c_p\left(u\frac{\partial T}{\partial x}+v\frac{\partial T}{\partial y}\right)=k_f\left(\frac{\partial^2 T}{\partial x^2}+\frac{\partial^2 T}{\partial y^2}\right) \tag{2.13 d}$$

By implementing the Boussinesq approximation, density will vary with temperature only in the last term of the y momentum equation. This buoyancy force term couples the momentum and energy equations. In order to set a reference for the density change, the local pressure (p) resulting from the fluid motion is measured relative to the local hydrostatic pressure (p_c) for a quiescent fluid at T_c. This is known as the pressure defect (p'), which is defined as:

$$p' = p - p_c = p - \rho_c g y \tag{2.14}$$

By using the volumetric thermal expansion coefficient, density can be defined in terms of temperature:

$$(\rho_c - \rho) g \approx \rho g \beta (T - T_c) \tag{2.15}$$

By implementing Equations 2.14 and 2.15, the modified pressure and body-force term in Equation 2.13 results in following x and y momentum equations:

$$\rho\left(u\frac{\partial u}{\partial x}+v\frac{\partial u}{\partial y}\right)=-\frac{\partial p'}{\partial x}+\mu\left(\frac{\partial^2 u}{\partial x^2}+\frac{\partial^2 u}{\partial y^2}\right) \tag{2.16 a}$$

$$\rho\left(u\frac{\partial v}{\partial x}+v\frac{\partial v}{\partial y}\right)=-\frac{\partial p'}{\partial y}+\mu\left(\frac{\partial^2 v}{\partial x^2}+\frac{\partial^2 v}{\partial y^2}\right)+\rho g\beta\left(T-T_c\right) \tag{2.16 b}$$

The boundary conditions for the convection-only model are as follows:

Left vertical (hot) wall

$$u=v=0,\quad T=T_h \quad \text{at} \quad x=0 \quad \text{for} \quad 0\le y\le H_c \tag{2.17 a}$$

Right vertical (cold) wall

$$u=v=0,\quad T=T_c \quad \text{at} \quad x=W_c \quad \text{for} \quad 0\le y\le H_c \tag{2.17 b}$$

Bottom adiabatic end-wall

$$u=v=0,\quad \frac{\partial T}{\partial y}=0 \quad \text{at} \quad y=0 \quad \text{for} \quad 0\le x\le W_c \tag{2.17 c}$$

Top adiabatic end-wall

$$u=v=0,\quad \frac{\partial T}{\partial y}=0 \quad \text{at} \quad y=H_c \quad \text{for} \quad 0\le x\le W_c \tag{2.17 d}$$

The steady-state conduction of the blind slats, with a constant thermal conductivity (k_b), is represented by Laplace's equation as follows:

Energy diffusivity:

$$\frac{\partial^2 T}{\partial x^2} + \frac{\partial^2 T}{\partial y^2} = 0 \tag{2.18}$$

At the blind-fluid interface, the no-slip and impermeability conditions are applied, as well as a convection-only heat flux balance, shown as follows:

Energy balance:

$$\left.\frac{\partial T}{\partial n}\right|_f = \frac{k_b}{k_f} \left.\frac{\partial T}{\partial n}\right|_b \tag{2.19}$$

where n is the normal unit vector from the blind surface (see Figure 2.1).

To validate the CFD solution of the above governing equations, a comparison was made with published experimental results (see Section 3.9). This obviously requires a full solution that involves radiative effects. Therefore, the full solution model boundary conditions for the end-walls and the blind are also presented. Equations 2.20 and 2.21 express the heat flux balance at the adiabatic end-walls and the blind, respectively:

Energy balance:

$$q''_{rad} + q''_{conv} = 0 \tag{2.20 a}$$

Bottom adiabatic end-wall:

$$q''_{rad} = k_f \left.\frac{\partial T}{\partial y}\right|_{y=0} \tag{2.20 b}$$

Top adiabatic end-wall:

$$q''_{rad} = -k_f \left.\frac{\partial T}{\partial y}\right|_{y=Hc} \tag{2.20 c}$$

where q''_{rad} is the local radiative heat flux from the end-wall. In the above convection-only boundary conditions, the q''_{rad} term equals zero.

Energy balance at the blind surface:

$$-k_b \left.\frac{\partial T}{\partial n}\right|_b = -k_f \left.\frac{\partial T}{\partial n}\right|_f + q''_{rad} \tag{2.21}$$

where n is the normal unit vector from the blind surface, and q''_{rad} is the local radiative heat flux also from the blind surface. All other boundary conditions that are not mentioned are similar to the convection-only boundary conditions.

2.5.1 Non-Dimensionalization

To obtain a general solution that is not specific to one case, the problem at hand has been non-dimensionalized. Therefore, a dimensionless form of the governing equations is required. The variables in the governing equations can be represented by the following dimensionless quantities [21]:

$$x^* = \frac{x}{W_c}, \quad y^* = \frac{y}{W_c}, \quad u^* = \frac{u}{u_{ref}}, \quad v^* = \frac{v}{u_{ref}}, \quad T^* = \frac{(T - T_c)}{(T_h - T_c)}, \quad p^* = \frac{p' W_c}{\mu u_{ref}} \tag{2.22}$$

where,

$$u_{ref} = \frac{\alpha \, Pr \, Gr^{1/2}}{W_c} = \frac{\nu}{W_c} Gr^{1/2} \tag{2.23}$$

By substituting Equation 2.22 into Equation 2.13, a dimensionless form of the governing equations is obtained as follows:

The dimensionless continuity equation:

$$\frac{\partial u^*}{\partial x^*} + \frac{\partial v^*}{\partial y^*} = 0 \tag{2.24 a}$$

The dimensionless momentum equations:

$$Gr^{1/2}\left(u^* \frac{\partial u^*}{\partial x^*} + v^* \frac{\partial u^*}{\partial y^*} \right) = -\frac{\partial p^*}{\partial x^*} + \left(\frac{\partial^2 u^*}{\partial x^{*2}} + \frac{\partial^2 u^*}{\partial y^{*2}} \right) \tag{2.24 b}$$

$$Gr^{1/2}\left(u^* \frac{\partial v^*}{\partial x^*} + v^* \frac{\partial v^*}{\partial y^*} \right) = -\frac{\partial p^*}{\partial y^*} + \left(\frac{\partial^2 v^*}{\partial x^{*2}} + \frac{\partial^2 v^*}{\partial y^{*2}} \right) + Gr^{1/2} T^* \tag{2.24 c}$$

The dimensionless energy equation:

$$Gr^{1/2} Pr \left(u^* \frac{\partial T^*}{\partial x^*} + v^* \frac{\partial T^*}{\partial y^*} \right) = \left(\frac{\partial^2 T^*}{\partial x^{*2}} + \frac{\partial^2 T^*}{\partial y^{*2}} \right) \tag{2.24 d}$$

The above governing equations no longer contain dimensional quantities but are still identical to their dimensional form (Equation 2.13). Commercial CFD software solve the dimensional governing equations. To obtain a dimensionless solution, the dimensionless variables must be entered as fluid properties and boundary conditions. Comparing the coefficients in Equations 2.13 to Equation 2.24, it can be see that:

$$\rho \equiv Gr^{1/2}, \quad c_p \equiv Pr, \quad k_f \equiv \mu \equiv \beta \equiv 1, \quad g \equiv -1, \quad T_h \equiv 1, \quad T_c \equiv 0 \tag{2.25}$$

Therefore, the dimensional coefficients are represented by these convenient dimensionless quantities. For the current parametric study, only the ρ input value in the numerical solver is modified to vary the Rayleigh number. Of course, the model geometry in Figure 2.1 must also be non-dimensionalized. The cavity width, W_c, has been used as the characteristic length to non-dimensionalize all geometrical lengths, including the following:

$$W_c{}^* = \frac{W_c}{W_c} = 1 \tag{2.26}$$

$$H_c{}^* = \frac{H_c}{W_c} = A \tag{2.27}$$

$$W_b{}^* = \frac{W_b}{W_c} \tag{2.28}$$

Figure 2.3 shows the dimensionless model geometry along with the convection-only boundary conditions as outlined in Equation 2.29.

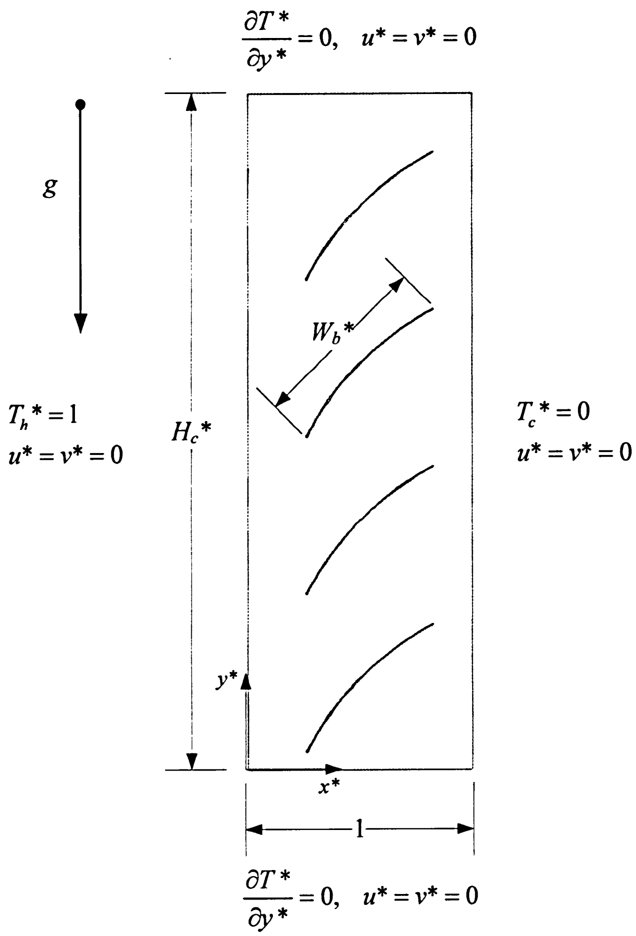

Figure 2.3: Dimensionless model geometry and boundary conditions

Left vertical (hot) wall

$$u^* = v^* = 0, \quad T^* = 1 \quad \text{at} \quad x^* = 0 \quad \text{for} \quad 0 \le y^* \le H_c{}^* \tag{2.29 a}$$

Right vertical (cold) wall

$$u^* = v^* = 0, \quad T^* = 0 \quad \text{at} \quad x^* = 1 \quad \text{for} \quad 0 \le y^* \le H_c{}^* \tag{2.29 b}$$

Bottom adiabatic end-wall

$$u^* = v^* = 0, \quad \frac{\partial T^*}{\partial y^*} = 0 \quad \text{at} \quad y^* = 0 \quad \text{for} \quad 0 \le x^* \le 1 \tag{2.29 c}$$

Top adiabatic end-wall

$$u^* = v^* = 0, \quad \frac{\partial T^*}{\partial y^*} = 0 \quad \text{at} \quad y^* = H_c^* \quad \text{for} \quad 0 \le x^* \le 1 \tag{2.29 d}$$

The dimensionless thermal diffusivity equation for the blind slat is now defined as:

Energy diffusivity:

$$\frac{\partial^2 T^*}{\partial x^{*2}} + \frac{\partial^2 T^*}{\partial y^{*2}} = 0 \tag{2.30}$$

The dimensionless heat flux balance equation for the blind is now defined as:

Energy balance:

$$\left.\frac{\partial T^*}{\partial n^*}\right|_f = k_b^* \left.\frac{\partial T^*}{\partial n^*}\right|_b \tag{2.31}$$

where k_b^* is the thermal conductivity ratio:

$$k_b^* = \frac{k_b}{k_f} \tag{2.32}$$

When the dimensionless properties from Equation 2.25 are entered into the numerical solver, a dimensionless convective heat transfer rate, q^*, is obtained. The relation between the dimensional and dimensionless convective heat transfer rate is expressed as follows:

$$q = k_f \left(T_h - T_c\right) q^* \tag{2.33}$$

where q^* for the hot and cold glazings equals:

$$q^* = -\int_0^{H_c^*} \left.\frac{\partial T^*}{\partial x^*}\right|_{x^*=0} dy^* = \int_0^{H_c^*} \left.\frac{\partial T^*}{\partial x^*}\right|_{x^*=W_c^*} dy^* \tag{2.34}$$

The Nusselt number can be calculated by substituting the dimensionless quantities from Equations 2.25 to 2.27 into Equation 1.6 from Chapter 1 (where $q_{conv} = q$, $A_g = H_c^*$, and $W = W_c^*$). The resulting average Nusselt number is expressed as follows:

$$Nu_{Wc} = \frac{q^*}{H_c^*} \tag{2.35}$$

2.6 Summary

The wide range of parameters chosen should provide results which will allow for a good understanding of the hydrodynamic and thermal interactions between the window and the blind. The non-dimensionalized model will apply to a wider range of conditions. This will also allow for the development of a practical correlation for the average Nusselt number for use in window design software. The customized governing equations presented, in theory, are hypothesized to capture the essential real world physical influences and define the problem in this study.

3

NUMERICAL MODELING AND ACCURACY

3.1 Introduction

Any paper reporting numerically obtained results considered for publication must address numerical uncertainty due to systematic truncation error and other inaccuracies. There is no single accepted method for reducing this uncertainty, but general guidelines should be considered in order to get a realistic numerical solution, if all important real world physical interactions of the flow are modeled correctly. For the present study, the following conditions are hypothesized to have a strong effect on truncation error and accuracy [41, 42]:

1. Numerical method used along with the choice of parameters selected.
2. Order of accuracy of the discretized governing equations.
3. Boundary, initial, and operating conditions.
4. Grid density / surface cluster density (for view factor calculations).
5. Grid topology.
6. Convergence criteria for the iterative calculations.

The following sections will explain the methods chosen to address the above conditions. The issue of flow stability is also briefly covered. For validation, a comparison is made to experimental results that have a known uncertainty.

3.2 Method, Parameters, and Order of Accuracy

The problem at hand has been solved using a commercial computational fluid dynamics package: FLUENT version 6.2. This software is capable of solving fluid dynamics problems by means of the control volume (CV) technique, using the governing equations outlined in Chapter 2. These conservation equations are numerically integrated about each CV or cell in the computational domain. This is made possible by representing the system of PDEs by algebraic approximations, which are often easily solved. For all simulations, the two-dimensional double-precision version of FLUENT was chosen along with a segregated solver and an implicit formulation for the discretization of the governing equations. The implicit linearization scheme should provide better stability in the iterative solution than the explicit scheme. For conjugate problems involving high thermal conductivity ratios and/or high aspect ratio grids, convergence and/or accuracy may be impaired with the single-precision solver due to inefficient transfer of boundary information [39].

The dimensionless quantities from Equation 2.25 were entered into their respective material property and boundary/operating condition sections in FLUENT. The Boussinesq approximation was selected for the density scheme. For the solution controls, the SIMPLEC algorithm was selected for the pressure-velocity coupling. The PRESTO! scheme was selected for the pressure discretization. This scheme is ideal for high Rayleigh number natural convective flow [39]. For the evaluation of the convective terms, a second-order upwind scheme was selected for the momentum and energy discretization. The second-order upwind scheme should be more sensitive to the flow direction, regardless of the grid topology, than other available methods. The use of a second-order accurate scheme will improve spatial accuracy in the computing of the quantities at the CV faces. The computation will be less susceptible to numerical diffusion by reducing the Taylor series truncation error. This error will simulate an increase in the effective diffusion constant. The diffusion terms in the governing equations are central-differenced and always second-order accurate.

The under-relaxation factors for the density, body forces, pressure, and energy were usually set to one, while the momentum under-relaxation factor was usually set to 0.7, depending on the Rayleigh number. For high Rayleigh numbers ($Ra_{Wc} > 4 \times 10^4$), the nonlinearity of the convective terms can cause convergence difficulties; therefore, the momentum under-relaxation factor was reduced to achieve stability. When using the segregated solver in FLUENT, no Courant (CFL) number input is available.

3.3 Boundary, Initial, and Operating Conditions

The study at hand involves natural convection in a sealed cavity (confined problem). Therefore, there is no direct (convective) interaction with any far-field boundary conditions. The vertical walls of the cavity have a Dirichlet or a fixed temperature boundary condition. The top and bottom cavity walls have a Neumann or an adiabatic (ZHF) boundary condition. Only steady-state solutions are required; therefore, no initial conditions (solutions) are necessary. These conditions are straight forward and need no special attention.

3.4 Grid Density

To determine a proper grid density, a grid sensitivity study was conducted. The study involved several simulations over a range of grid resolutions using different meshing schemes. This is the main method to systematically gain accuracy and reduce truncation error (numerical diffusion).

An initial simulation on a coarse, uniform, structured, quadrilateral mesh was done in order to get an idea of the overall characteristics of the temperature and flow field. This simple mesh type is a fail-safe approach, where no bias is created by concentrating the distribution of the CVs by grading of the mesh. To better estimate the governing equations, the grid was subsequently refined, equally in the x and y directions, until no significant difference (< 0.01 %) was observed in the vertical wall Nusselt number between successive simulations. This Nusselt number is taken to be grid independent.

For the grid sensitivity study, a typical Rayleigh number (for window applications) of 10^4 was used with a W_b / W_c ratio of 0.9 and slat angles of 0° and 75°. From examining the temperature field of the initial coarse grid simulation, these parameters showed the strongest thermal and hydrodynamic interaction (worst case scenario). For the 0° slat angle case, high thermal gradients were apparent between the small slat tip-to-glazing spacings (s_h and s_c). For the 75° slat angle case, higher velocities and thinner boundary layers were observed. Figure 3.1 shows the meshing scheme for the two configurations. Both cases have quadrilateral elements, but the 75° case mesh is unstructured, where the control volumes are paved instead of mapped.

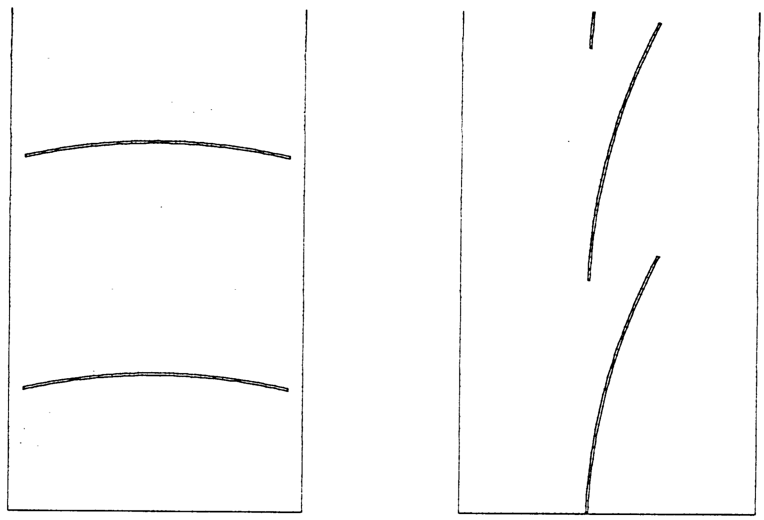

Figure 3.1: Quadrilateral meshing scheme, bottom of cavity (a) mapped grid for 0° slat angle (GIS = 0.015), (b) paved grid for 75° slat angle (GIS = 0.02)

Tables 3.1 and 3.2 show the results of the convection-only grid independence study. The percent error calculations are relative to the converged Nusselt number (i.e. $Nu_{Wc} = 2.840$ and 1.336). Richardson extrapolation was not used. The grid interval size (GIS) is a measure of grid density, it is defined as follows:

$$\text{GIS} = \frac{W_c}{n_{Wc}} \tag{3.1}$$

where n_{Wc} is the number of nodes across W_c.

The grid interval sizes of 0.015 and 0.025 were chosen as the largest grid interval size limits for cases with a slat angle of 0° and 75°, respectively. It is assumed that the for a slat angle of 45°, the required grid interval size will fall in these limits.

Table 3.1: Grid independence study results for a mapped grid
($Ra_{Wc} = 10^4$, $A = 20$, $W_b / W_c = 0.9$, $k_b / k_f = 4600$, $\Phi = 0°$)

GIS	CVs	Iterations	Nu_{Wc}	% Error
0.0200	50592	106	2.785	1.95%
0.0175	66294	116	2.802	1.35%
0.0150	**91767**	**144**	**2.832**	**0.29%**
0.0125	133757	202	2.837	0.12%
0.0100	202606	313	2.840	0.01%
0.0075	360045	1267	2.840	0.00%

Table 3.2: Grid independence study results for a paved grid
($Ra_{Wc} = 10^4$, $A = 20$, $W_b / W_c = 0.9$, $k_b / k_f = 4600$, $\Phi = 75°$)

GIS	CVs	Iterations	Nu_{Wc}	% Error
0.0300	22122	349	1.340	0.33%
0.0250	**32350**	**472**	**1.339**	**0.19%**
0.0200	50148	582	1.337	0.08%
0.0175	65926	680	1.336	0.03%
0.0150	90079	1147	1.336	0.00%

As a result of the high temperature gradients between the slat tip-to-glazing spacing for the 0° slat angle case, a non-uniform grid was developed. The grid density was concentrated at the location of these high temperature gradients, while a lower grid density was used in the core region. The results showed that the core region grid density is just as influential on the Nusselt number as the grid density between the slat tip-to-glazing spacing. Therefore, a non-uniform grid is not necessary. The details of this study have been omitted.

For the 75° slat angle case, the grid density required for a grid independent solution is much sparser than the 0° case. Therefore, for a small slat angle a higher grid density is required. Considering the computational overhead and accuracy of the solutions from the grid sensitivity study, the grid interval sizes in Table 3.3 were chosen. The average vertical wall Nusselt number values are estimated to be grid independent to better than 0.3%.

Table 3.3: Grid interval size for different slat angles and blind width to cavity width ratios

Angle [Degrees]	$W_b/W_c =$ 0.50	$W_b/W_c =$ 0.65	$W_b/W_c =$ 0.80	$W_b/W_c =$ 0.90
0°	0.0200	0.0175	0.0150	0.0150
45°	0.0250	0.0225	0.0200	0.0200
75°	0.0250	0.0250	0.0225	0.0200

3.5 Surface Cluster Density

Even though radiation effects are not considered in the parametric study, a separate study was done to evaluate the number of faces per surface cluster needed for an accurate evaluation of the radiative heat transfer. Clustering involves reducing the number of radiating surfaces (CVs) by grouping neighbouring faces for the purpose of view factor calculations. For comparison to experimental and to theoretical (Simplified Model) results, radiation effects are required for a full conjugate solution. In FLUENT, the *Surface-to-Surface* (S2S) radiation model was chosen for the calculation of the view factors. The S2S radiation model is ideal for enclosures that assume *gray-diffuse* surfaces with no participating medium effects from the fill-gas. For the flow boundary zones, 10 faces per surface cluster were initially used. In the View Parameters section of FLUENT, *Blocking* was chosen for the Surfaces option along with a *Least Square Smoothing* scheme. The Blocking option is required because the blind blocks the view between the two glazing surfaces. The Least Square Smoothing scheme enforces reciprocity and conservation of the view factor matrix. The radiosity convergence tolerance was set to 0.0001. Reducing the faces per surface cluster to 5 did not make a significant difference in the radiative heat transfer rate (< 1%). Therefore, 10 faces per surface cluster were used for all computations that require radiation effects. Some of the details of the radiative governing equations are covered in Chapter 5.

3.6 Grid Topology

The grid topology plays a significant role in the accuracy and stability of the computation. Uniform quadrilateral elements were used, while keeping skewness and high aspect ratio cells to a minimum, in order to avoid convergence difficulties. For slat angles of 45° and 75°, the quadrilateral elements were paved (unstructured) as opposed to mapped (structured) onto the computational domain (see Figure 3.1). Quadrilateral elements have a good alignment to the flow direction of the fluid near a boundary, as well as to the diffusive (i.e. velocity or thermal) gradient direction, which is perpendicular to the boundary. Figure 3.2 illustrates this, where $u \approx \partial v / \partial y \approx \partial T / \partial y \approx 0$. This yields greater accuracy in the solution by minimizing numerical diffusion. The modeling and mesh generating software, GAMBIT version 2.2, was used for meshing the computational domain. A program was developed to generate the window geometry (see Appendix C).

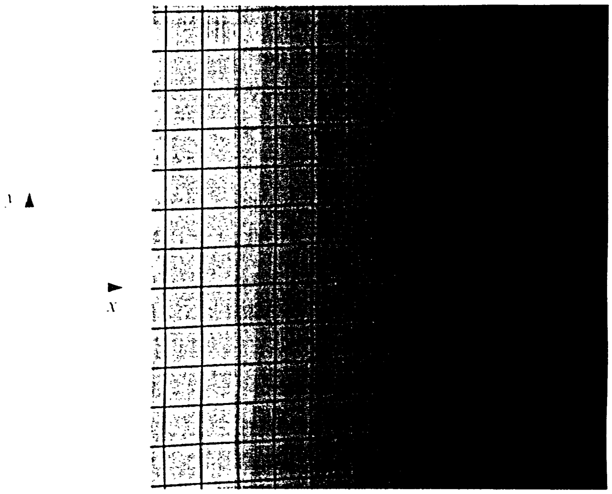

Figure 3.2: A superimposed mesh on temperature or velocity gradient at a boundary or glazing surface

3.7 Convergence Criteria

There is no universal method for determining convergence. Residuals of the governing equations that are acceptable for one class of problems are sometimes misleading for other class of problems [41, 42]. Therefore, judging convergence should not only be done by examining residual values, but by monitoring relevant integrated quantities such as heat transfer rate. In this study, the residuals for the continuity, x and y momentum, and energy equations are poor indicators of a converged heat transfer rate. Generally, it is difficult to judge convergence by examining these residuals, since scaling is not possible for a buoyancy-driven flow in a cavity where there is no inlet flow rate to compare to. In all cases, the heat transfer rate for the vertical walls was monitored and used as the stopping criteria. The computation was stopped when no significant difference was observed between successive iteration levels (i) (pseudo time advancements), such that:

$$\frac{q^{*i-1} - q^{*i}}{q^{*i}} < 0.001 \qquad (3.2)$$

Regardless of the criterion in Equation 3.2, the residuals for the continuity, x and y momentum, and energy equations were allowed to converge to less than 10^{-3}.

3.8 Flow Stability

Thermal instabilities within the buoyancy-driven flow can cause unsteadiness when some critical Rayleigh number is reached. As mentioned, unsteady flow enhances the convective heat transfer rate. Because the flow in this study is assumed strictly steady, numerical solutions could under-predict Nusselt number, typically at high Rayleigh numbers.

For a gas filled rectangular enclosure with no blind, there are empirical data available for a critical Grashof or Rayleigh number (e.g. Equation 1.7). However, no experimental data exist for a cavity with a between-pane blind to predict the onset of unsteady flow. This is an important issue and should be addressed. The following analysis was done, as a guide, to determine the extent of the discrepancy between the Nusselt number obtained from a CFD solution and an empirical correlation for a cavity with no blind.

3.8.1 Critical Rayleigh Number

ElSherbiny et al. [11] and Wright's [12] empirical correlations (Equations 1.10 and 1.11) were used to calculate the Nusselt number for an empty cavity for comparison to a numerically obtained value at the corresponding Rayleigh number. If the average of the two correlations agrees with the numerically obtained Nusselt number, then the numerical solution is acceptable, such that unsteadiness in the flow has a small effect on the heat transfer rate.

Table 3.4 contains Nusselt number data obtained from the empirical and numerical methods, mentioned above, for an empty cavity with an aspect ratio of 20. The data from Table 3.4 have been plotted in Figure 3.3 and show that the numerical Nusselt number is progressively under-predicted as Rayleigh number is increased past $Ra_{Wc} = 2 \times 10^4$. At a Rayleigh number of $Ra_{Wc} = 10^5$, the percent difference rises to 11.9%, which is likely due to unsteady flow. Using Equation 1.7, the critical Rayleigh number ($Pr = 0.71$) for the onset of secondary flow is calculated to only be 7.10×10^3. The numerically predicted solution could have difficulties in resolving secondary flow as Rayleigh number approaches 10^4 [7]. At higher Rayleigh numbers (under the steady flow assumption) the numerical solution will have difficulty converging and possibly yield a lower heat transfer rate. This discrepancy will be greater for taller cavities.

Table 3.4: Nusselt number comparison between empirical and numerical methods for an empty cavity with an aspect ratio of 20 (Ra_{Wc} = 100 to 10^5, A = 20)

Ra_{Wc}	Correlation Nu_{Wc} [11]	Correlation Nu_{Wc} [12]	Correlation Average Nu_{Wc}	Present Numerical Nu_{Wc}	% Difference
10^2	1.00	1.00	1.00	1.00	0.0%
10^3	1.00	1.00	1.00	1.02	2.2%
10^4	1.31	1.28	1.29	1.38	6.6%
2×10^4	1.69	1.69	1.69	1.71	1.0%
4×10^4	2.22	2.25	2.23	2.10	-6.1%
10^5	3.00	3.13	3.07	2.72	-11.9%

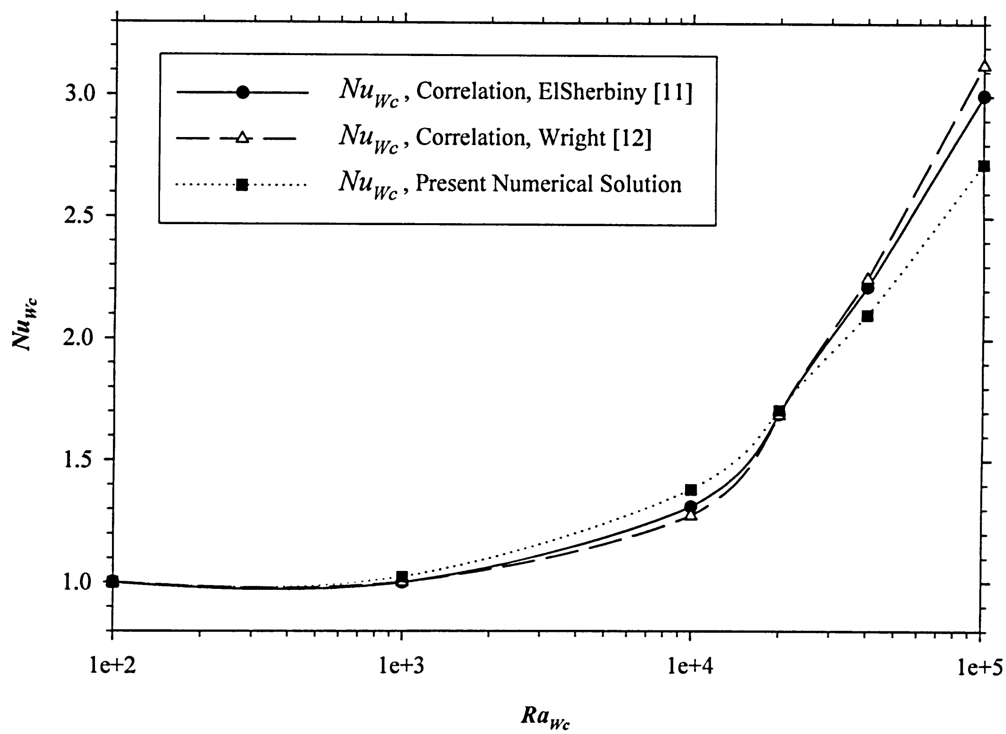

Figure 3.3: Plot of Nusselt numbers for an empty cavity with an aspect ratio of 20 (Ra_{Wc} = 100 to 10^5, A = 20)

When a blind is placed between two glazings, it is reasonable to expect that the buoyancy-driven flow will be inhibited to some extent, which could delay the onset of unsteady flow. The stream function is an integral quantity that characterizes the strength of the flow (flow rate) and defines streamlines. It is defined as follows:

$$u = -\frac{\partial \psi}{\partial y} \tag{3.3}$$

$$v = \frac{\partial \psi}{\partial x} \tag{3.4}$$

The stream function for different blind configurations, at a Rayleigh number of 10^5, is shown in Chapter 4, in Tables 4.1 and 4.2. For a slat angle of 0° (open blind), with a blind width to cavity width ratio near unity, the flow rate is about one order of magnitude less than that of a cavity with no blind. This should reduce the effect of unsteady flow. For slat angles at 75° (closed blind), the flow is not as inhibited. But, for this configuration, the window cavity is somewhat divided on the vertical centreline by the blind, forming two adjacent cavities. This arguably makes the effective Rayleigh number much smaller if the *semi-enclosure* cavity width (characteristic length) and the temperature difference are used in its calculation. Figure 3.4 illustrates the two sealed semi-enclosures. In this hypothetical case, the effective Rayleigh number limit approaches 1/16 times the full enclosure Rayleigh number. In most cases, this effective Rayleigh number will fall below the critical Rayleigh number for an empty cavity, predicted by Equation 1.7. More so, the blind will inherently push the critical Rayleigh number higher. In other words, for the same amount of body force on the fluid in a cavity with a blind will result in a weaker flow than an empty cavity.

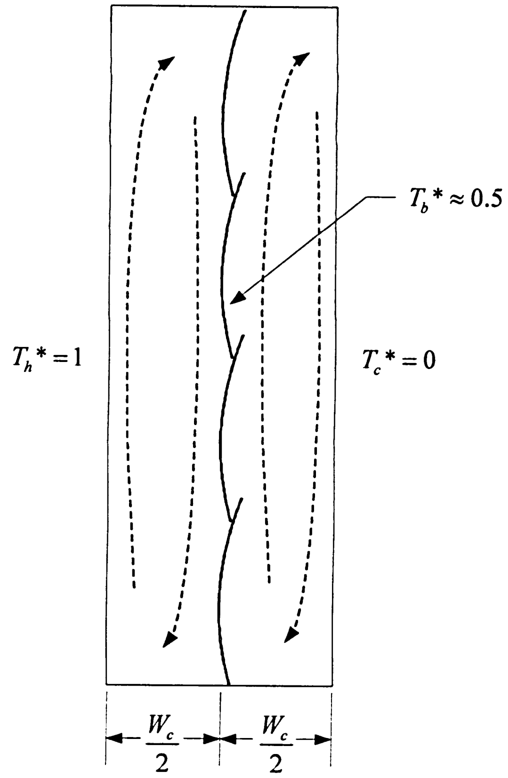

Figure 3.4: Semi-enclosure approximation (sealed, $\Phi = 87°$)

The validity of these arguments is supported by the close agreement of the current numerical results with the experimental measurements found in the following section. Therefore, the blind should fundamentally provide greater stability within the flow domain. In this study, it is assumed that the unsteadiness of the flow at high Rayleigh numbers will not have a significant effect on the resulting Nusselt number.

3.9 Validation

The best way to validate numerical results is to compare them to experimental measurements. Fortunately, Huang [35] and Lai [10] have done recent experimental work using a guarded heater plate apparatus and a Mach-Zehnder laser interferometer, respectively.

The exact geometry and conditions of Huang's [35] and Lai's [10] experiment have been modeled using the conditions mentioned above.

The GHP apparatus is sophisticated in its method of measuring one-dimensional total heat flux (q'') using a heat flux meter. The technique yields highly accurate measurements with a repeatability better than ±3%. The overall heat transfer data obtained from this method include both the convective and radiative constituents.

The MZI apparatus and method of obtaining convective heat transfer coefficients are highly complex. This technique provides a non-intrusive method of obtaining a full-field temperature visualization and local heat transfer data. The temperature visualization is well suited for qualitative comparison to numerical predictions. A curve-fitting algorithm was used by Lai [10] to calculate the temperature gradient normal to the hot plate, in order to obtain local convective heat transfer coefficient values using the following formula:

$$h_h = \frac{-k_{f,x=0} \left.\frac{\partial T}{\partial x}\right|_{x=0}}{\left(T_h - T_c\right)} \tag{3.5}$$

The error analysis done by Lai indicates that an average uncertainty for the local Nusselt number measurement is about ±7%. This method of measuring heat transfer rate only includes the convective portion.

Table 3.5 contains U-values obtained from the present numerical solution and Huang's [35] GHP experimental measurements for the centre-glass region of the window/blind system at a Rayleigh number of 1.39 x 10^4. In Huang's study, the centre-glass region had a length of 203 mm (8 inches), half way up the cavity height of 604 mm. The U-values of both studies show excellent agreement, with the largest difference being 3.3%. The U-values from Table 3.5 have been plotted in Figure 3.5.

Table 3.5: Centre-glass experimental and numerical U-value comparison for slat angles of 0°, 30°, 60°, and 75° (Ra_{Wc} = 1.39 x 10^4, A = 23.8, W_b / W_c = 0.58, k_b / k_f = 4615, Φ = 0°, 30°, 60°, and 75°, T_h = 302.59 K, T_c = 293.41 K, ε_g = 0.84, ε_b = 0.792, ε_{ew} = 0.84)

Angle, Φ [Degrees]	**Present Numerical U-value** [W/m²K]	**Experimental U-value [35]** [W/m²K]	**% Difference**
0°	4.69	4.66	0.64%
30°	4.41	4.33	1.83%
60°	3.71	3.59	3.29%
75°	3.34	3.31	0.90%

Tables 3.6 and 3.7 contain the average Nusselt numbers obtained from the present numerical solution and Lai's [10] MZI experimental measurements for the entire vertical hot wall for slat angles of 0° and 45°, respectively. The percent difference seems to be higher for the slat angle of 45° case. The Nusselt numbers from Table 3.6 and 3.7 have been plotted in Figure 3.6. Considering the dissimilarity of the two methods, a difference of about 10% in the average Nusselt numbers is quite acceptable. For the increase in the Rayleigh number, the glazing spacing was increased as follows: W_c = 28.7 mm, 32.7 mm, and 40.7 mm.

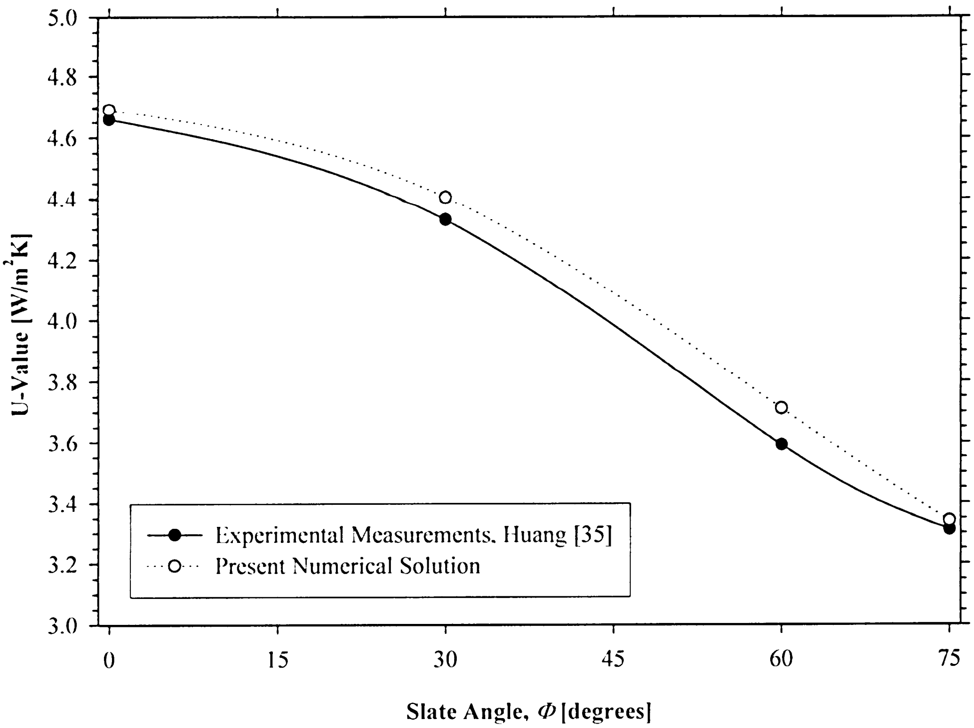

Figure 3.5: Centre-glass experimental and numerical U-value comparison for slat angles of 0°, 30°, 60°, and 75° (±3% error bar) (Ra_{Wc} = 1.39 x 10^4, A = 23.8, W_b / W_c = 0.58, k_b / k_f = 4615, Φ = 0°, 30°, 60°, and 75°, T_h = 302.59 K, T_c = 293.41 K, ε_g = 0.84, ε_b = 0.792, ε_{cw} = 0.84)

Table 3.6: Nusselt number comparison between experimental and numerical results for slat angle of 0° (Ra_{Wc} = 4.56 x 10^4, 6.75 x 10^4, and 1.30 x 10^5, A = 13.3, 11.6, and 9.3, W_b / W_c = 0.86, 0.76, and 0.61, respectively, k_b / k_f = 4617, Φ = 0°)

Ra_{Wc}	Present Numerical Nu_{Wc}	Experimental Nu_{Wc} [10]	% Difference
4.56 x 10^4	3.043	2.873	5.75%
6.75 x 10^4	2.616	2.485	5.14%
1.30 x 10^5	2.967	2.666	10.69%

Table 3.7: Nusselt number comparison between experimental and numerical results for slat angle of 45° (Ra_{Wc} = 4.56 x 10^4, 6.75 x 10^4, and 1.30 x 10^5, A = 13.3, 11.6, and 9.3, W_b / W_c = 0.86, 0.76, and 0.61, respectively, k_b / k_f = 4617, Φ = 45°)

Ra_{Wc}	Present Numerical Nu_{Wc}	Experimental Nu_{Wc} [10]	% Difference
4.56 x 10^4	1.927	2.112	- 9.16%
6.75 x 10^4	2.203	2.364	- 7.05%
1.30 x 10^5	3.131	2.802	11.09%

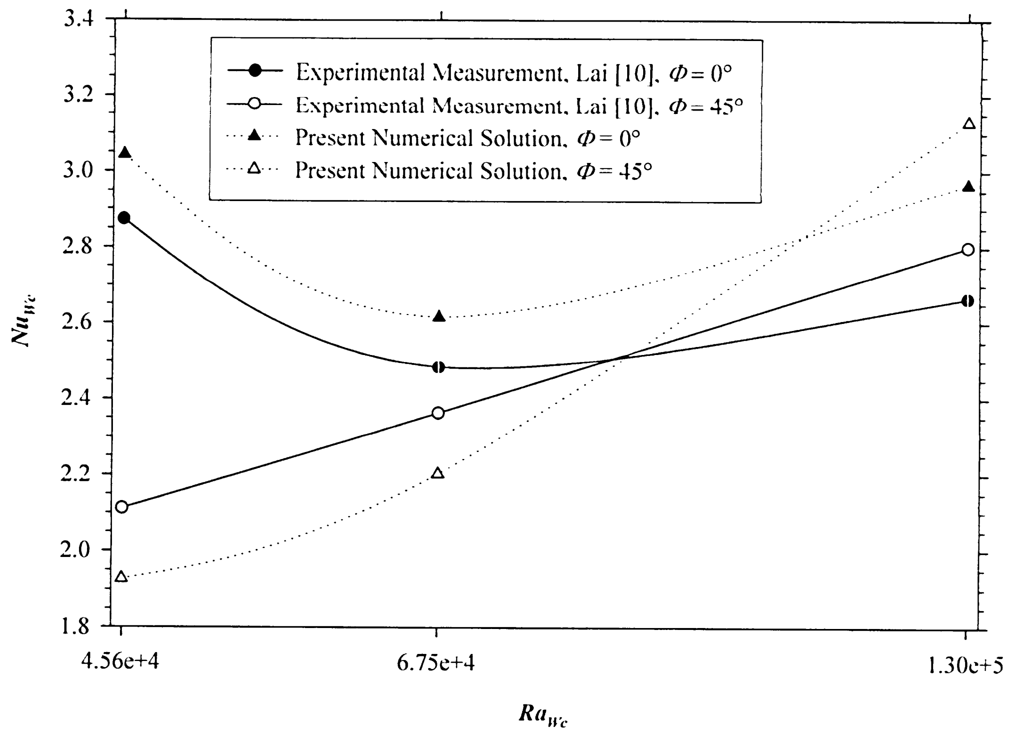

Figure 3.6: Average Nusselt number comparison between experimental and numerical results (±7% error bar) (Ra_{Wc} = 4.56 x 10^4, 6.75 x 10^4, and 1.30 x 10^5, A = 13.3, 11.6, and 9.3, W_b / W_c = 0.86, 0.76, and 0.61, respectively, k_b / k_f = 4617, Φ = 0° and 45°)

Figure 3.7 shows a plot of the present numerical and experimental local Nusselt numbers for the 0° slat angle and 28.7 mm cavity width case. The trend of the curves agrees very well, where the local Nusselt number maxima and minima are at the same spatial location and frequency. Figure 3.8 illustrates the temperature field and the stream function contours alongside the interferograms. A full cavity is shown along with an enlarged view of the top and bottom sections. The temperature fields show a very close agreement to one another.

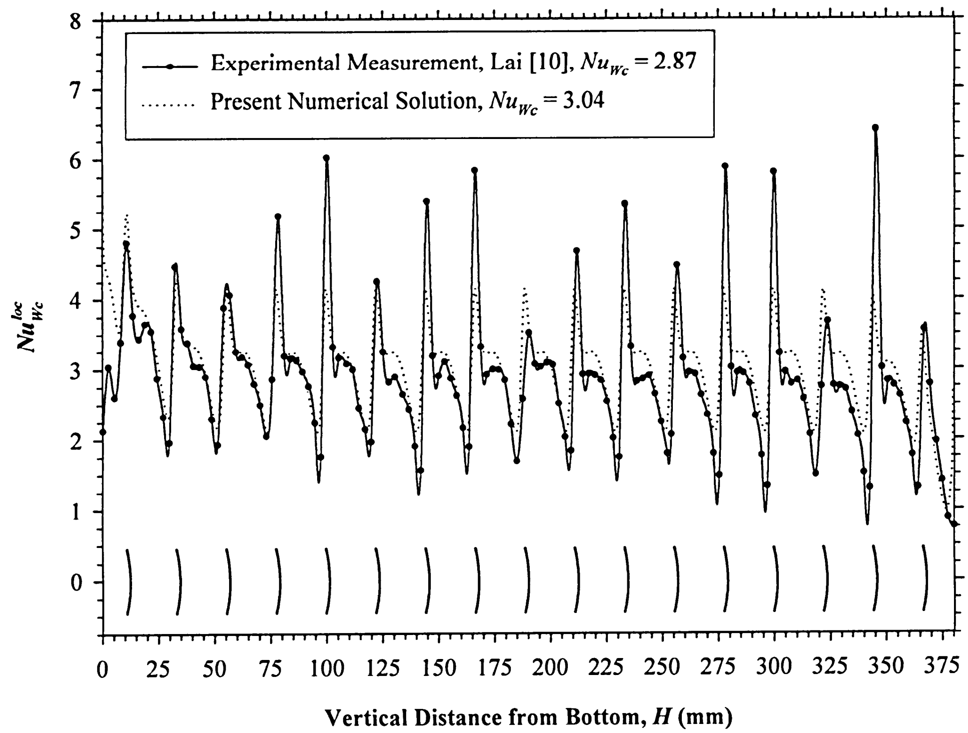

Figure 3.7: Local Nusselt number comparison between experimental and numerical results for a slat angle of 0° (Ra_{Wc} = 4.56 x 10^4, A = 13.3, W_b / W_c = 0.86, k_b / k_f = 4617, Φ = 0°)

Figure 3.9 shows a plot of the present numerical and experimental local Nusselt numbers for the 45° slat angle and 28.7 mm cavity width case. Unexpectedly, the experimental and the numerical Nusselt number distributions do not show a close agreement in trend. The experimental curve has a substantial variation in the local convective heat transfer rate which is not predicted numerically. A component of the flow could be unperceived for the 45° slat angle case, assuming the solution is grid independent. However, the average heat transfer rates are within 10%. When considering averaged values, including U-values, some error smoothing could be involved.

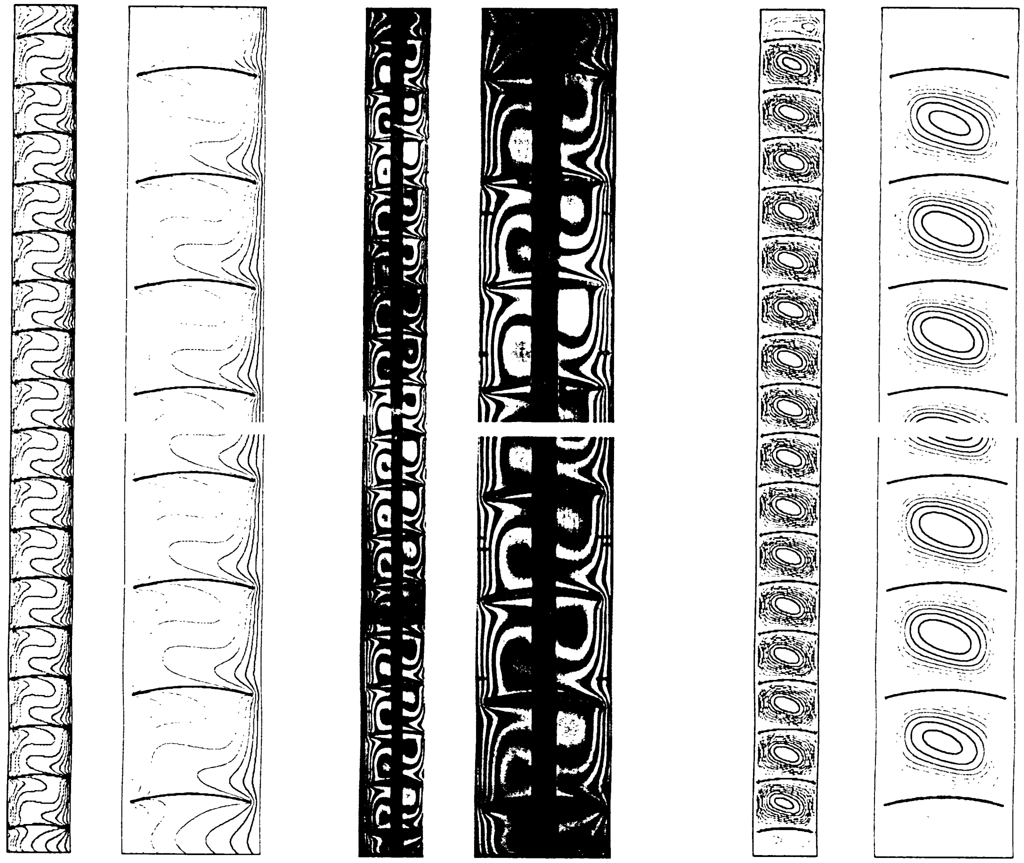

(a) T^{num} (b) T^{MZI} (c) ψ^{num}

Figure 3.8: (a) Numerical temperature field contours, (b) experimental temperature field contours, Lai [10], (c) stream function contours, for a slat angle of 0° ($Ra_{Wc} = 4.56 \times 10^4$, $A = 13.3$, $W_b / W_c = 0.86$, $k_b / k_f = 4617$, $\Phi = 0°$)

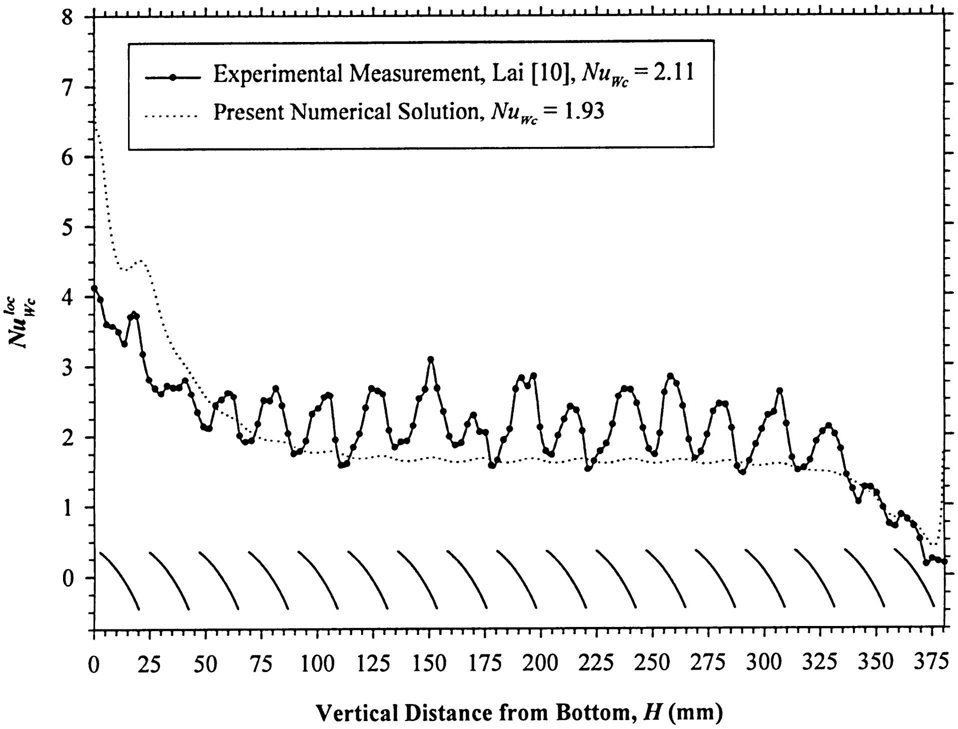

Figure 3.9: Local Nusselt number comparison between experimental and numerical results for a slat angle of 45° ($Ra_{Wc} = 4.56 \times 10^4$, $A = 13.3$, $W_b / W_c = 0.86$, $k_b / k_f = 4617$, $\Phi = 45°$)

Figure 3.10 illustrates the temperature field and stream function contours alongside the interferograms. There is a noticeable difference in the predicted temperature fields. The interferogram appears to show that the secondary recirculating flow between the blind slats is much stronger than what is predicted numerically. This may be the reason why the curves in Figure 3.9 do not agree well. Interestingly, an earlier finite element CFD model by Lai and Naylor [43] also showed a similar poor agreement. The cause of this small discrepancy is unclear at this time, but, it is postulated that the flow is slightly unsteady for this configuration (i.e. missing transients). It is possible that any unsteadiness was not noticed during Lai's [10] experiment because of the beam-averaging nature of interferometry. Beam-averaging tends to hide fluctuations in the flow field, especially those which are out of phase along the path of the laser [44]. This discrepancy is further discussed in Section 4.2.7.

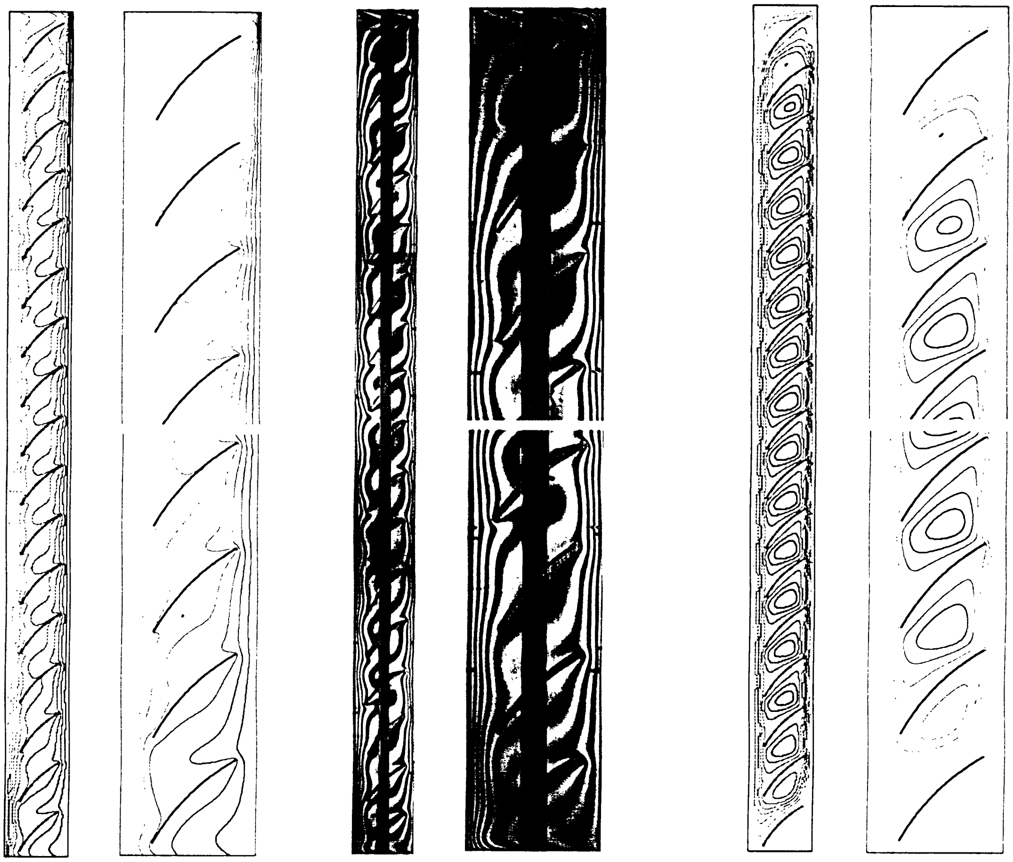

(a) T^{num} (b) T^{MZI} (c) ψ^{num}

Figure 3.10: (a) Numerical temperature field contours, (b) experimental temperature field contours, Lai [10], (c) stream function contours, for a slat angle of 45° ($Ra_{W_c} = 4.56 \times 10^4$, $A = 13.3$, $W_b / W_c = 0.86$, $k_b / k_f = 4617$, $\Phi = 45°$)

3.10 Summary

By careful consideration of the options and methods for the conditions outlined in Section 3.1, numerical uncertainty should be greatly reduced. Overall, the comparison of the numerical results to the experimental measurements confirms that the numerical model is valid and has been set up correctly. In the following chapter, the parametric study of the present window/blind system is conducted with confidence.

4

PARAMETRIC STUDY RESULTS AND DISCUSSION

4.1 Introduction

The free convective heat transfer rate of a double-glazed window with a between-pane blind has been determined under different geometrical and thermo-physical conditions. These parametric variations, presented in Table 2.1, have resulted in approximately 600 convection-only numerical simulations. These simulations include the effects of conduction in the blind slats, but exclude the effects of thermal radiation. In this chapter, the results and discussion from the parametric study are presented.

4.2 Numerical Results

The parametric approach taken in this study allows for a detailed analysis of the hydrodynamic and thermal features of a window/blind system. From observation of the numerical results, it is evident that, when a blind is placed in a cavity, the heat transfer rate is affected by the following three main phenomena:

1. The blind's thermal conduction across the glazings.
2. The blind's impeding effect on the (primary) buoyancy-driven flow.
3. The blind's enhancing or inhibiting effect on the cross-cavity flow by redirection of the two counter-flowing boundary layers.

In ascending order, the three factors increase in complexity and importance in regards to the thermal performance of a window/blind system, especially as Rayleigh number increases. The first factor helps increase the heat transfer rate, while the second factor helps decrease it. Depending on the blind configuration, the third factor can do either.

The local and average Nusselt numbers from the CFD solutions are plotted in the following sections. The analyses of the parameters that affect the Nusselt number are broken down into the following sections: blind width to cavity width ratio, slat angle, blind to fluid thermal conductivity ratio, cavity aspect ratio, and positive and negative slat angle. These configurations of a window/blind system will influence the extent of each of the three factors stated above.

For comparison purposes, in most of the graphs in this chapter an average Nusselt number curve for an empty cavity has been plotted using the average of the correlation by ElSherbiny et al. [11] and Wright [12] (Equations 1.10 and 1.11). The curve is labelled in the graph's legend as: *Empty Cavity (Correlation).* A general comparison between the present study and an empty cavity is made in Section 4.3. The average Nusselt number for the hot and cold glazings is very similar (typically within 0.01%); therefore, only the hot wall results are presented. The complete set of data can be found in Appendix A and B. More emphasis is given to data that consider a blind to fluid thermal conductivity ratio (k_b / k_f) equal to 4600, since this corresponds to a standard aluminium blind. In most of the graphs, only plots for an aspect ratio of 60 are presented. The general behaviour of the results for the other two aspect ratios is very similar. The effects of aspect ratio are discussed in Section 4.2.6.

4.2.1 Interpretation of Nusselt Number

For each numerical solution, the Nusselt number has been calculated based on the cavity width representing the characteristic length scale. This length scale is also used to non-dimensionalize the geometric lengths in the model, making the dimensionless cavity width equal to one for all cases (see Figure 2.3). As a result, its physical significance in regards to the thickness of the conductive layer can become obscured. Nusselt number is defined as the ratio between the convective heat transfer rate and the conductive heat transfer rate across a fluid layer with a thickness equal to the chosen length scale. If the cavity width is fixed and used as the length scale, a direct comparison of Nusselt number is possible to determine the change of the convective heat transfer rate as the blind width is varied. However, for a fixed blind width, in order to compare the convective heat transfer rate change as the cavity width is varied, the blind width should be used as the length scale. Therefore, a modified Nusselt number (Nu_{Wb}) is required and is defined as follows:

$$Nu_{Wb} = Nu_{Wc}\frac{W_b}{W_c} = \frac{hW_b}{k_f} \tag{4.1}$$

This definition of Nusselt number considers the thickness of the conductive layer and maintains a proper proportion between the two modes of heat transfer, making a direct comparison possible. As mentioned, in this study, only the dimensionless cavity width is held constant (i.e. $W_c^* = 1$) while the dimensionless blind width is varied. Similarly, a modified Rayleigh number (Ra_{Wb}) is required, since it also involves the cavity width:

$$Ra_{Wb} = Ra_{Wc}\left(\frac{W_b}{W_c}\right)^3 = \frac{g\beta(T_h - T_c)W_b^3}{\nu\alpha} \tag{4.2}$$

Figures 4.1 to 4.3 show the effect the two different length scales have on the average Nusselt number for blind width to cavity width ratios of 0.5 and 0.9, at slat angles of 0°, 45°, and 75°. When W_c is used as the length scale (typical for this study), the two curves for different values of W_b / W_c should be interpreted as the enclosure width (W_c) remaining constant, and the blind width (W_b) as variable. With this interpretation, the Nusselt number (Nu_{Wc}) will be proportional to the total convective heat transfer rate. Therefore, these curves can be used to examine the effect of variable blind widths for fixed glazing spacings.

Similarly, when W_b is used as the length scale, the two curves for different values of W_b / W_c should be interpreted as the blind width remaining constant, and the enclosure width as variable. With this interpretation, the Nusselt number (Nu_{Wb}) will be proportional to the total convective heat transfer rate. Therefore, these curves can be used to examine the effect of changing the glazing spacing for a fixed blind size. As stated above, curves with different length scales are not comparable.

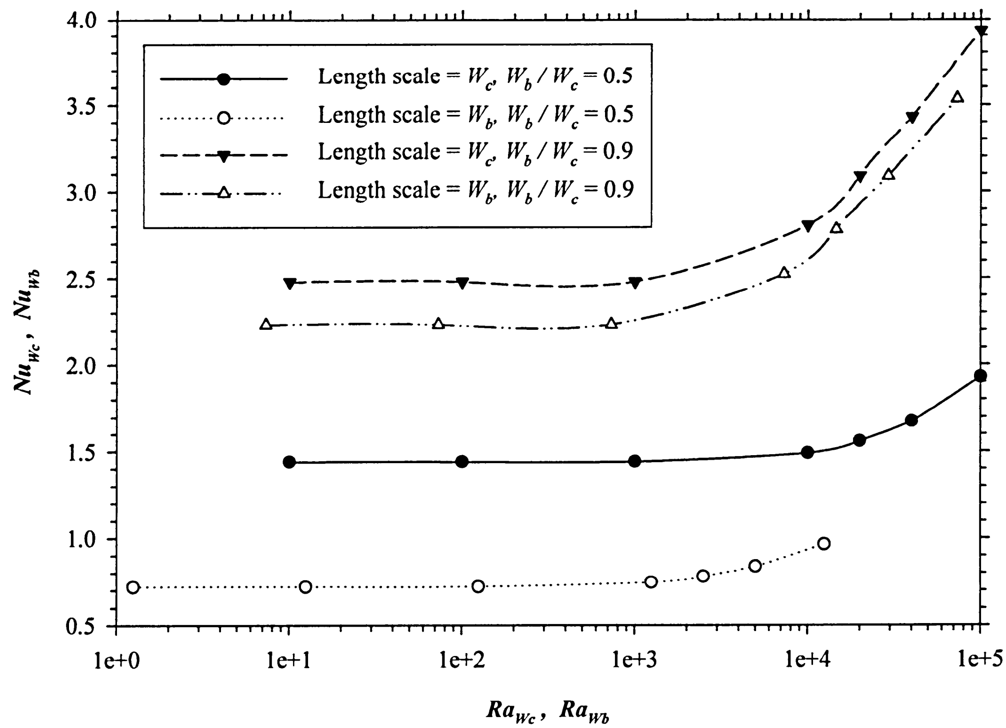

Figure 4.1: Effect of length scale on average Nusselt number for a slat angle of 0° (Ra_{Wc} = 10 to 10^5, A = 60, W_b / W_c = 0.5 and 0.9, k_b / k_f = 4600, Φ = 0°)

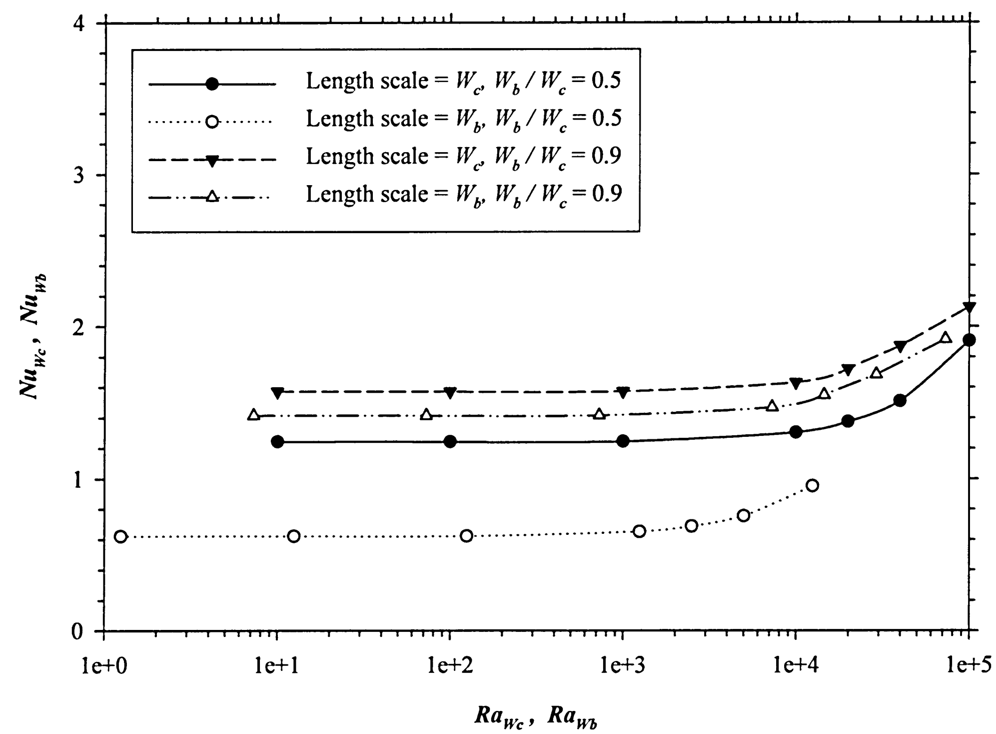

Figure 4.2: Effect of length scale on average Nusselt number for a slat angle of 45° (Ra_{Wc} = 10 to 10^5, A = 60, W_b / W_c = 0.5 and 0.9, k_b / k_f = 4600, Φ = 45°)

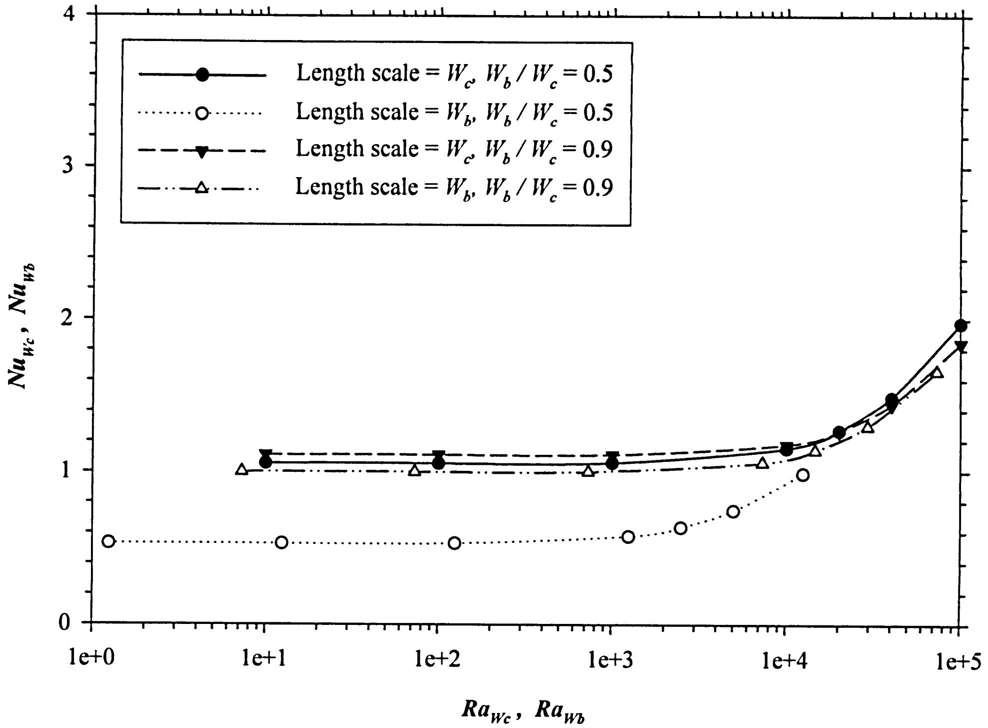

Figure 4.3: Effect of length scale on average Nusselt number for a slat angle of 75° (Ra_{Wc} = 10 to 10^5, A = 60, W_b / W_c = 0.5 and 0.9, k_b / k_f = 4600, Φ = 75°)

For example, in Figure 4.1, considering the two curves with W_c as the length scale, the W_b / W_c ratio changing from 0.9 to 0.5 can be interpreted as a reduction in the blind width (W_b) while the cavity width (W_c) remains constant. This change corresponds to a 44% to 50% reduction in the convective heat transfer rate across the enclosure. Now considering the two curves with W_b as the length scale, the W_b / W_c ratio changing from 0.9 to 0.5 can be interpreted as almost doubling the glazing spacing (W_c) while the blind width (W_b) remains constant. This change corresponds to a 70% reduction in the convective heat transfer rate across the enclosure.

The results in this study are presented using W_c as the characteristic length. Therefore, Equations 4.1 and 4.2 are required to rescale the data for a proper interpretation of the effect the glazing spacing has on the convective heat transfer rate, for a fixed blind geometry.

4.2.2 Blind Width to Cavity Width Ratio

The blind width to cavity width ratio has a strong influence on the three factors that affect the (non-radiative) heat transfer rate of a window/blind system. From a window designer's point of view, this parameter is of greatest interest. The increase in the slat angle (Φ) or the decrease in the W_b / W_c ratio has a similar effect on the Nusselt number. This is not surprising because both geometrical aspects determine the slat tip-to-glazing spacing (s_h and s_c). Figure 4.4 depicts the *effective blind width*, W_b^{eff}, of a rotated slat and shows its relation to W_b, s_h, and s_c.

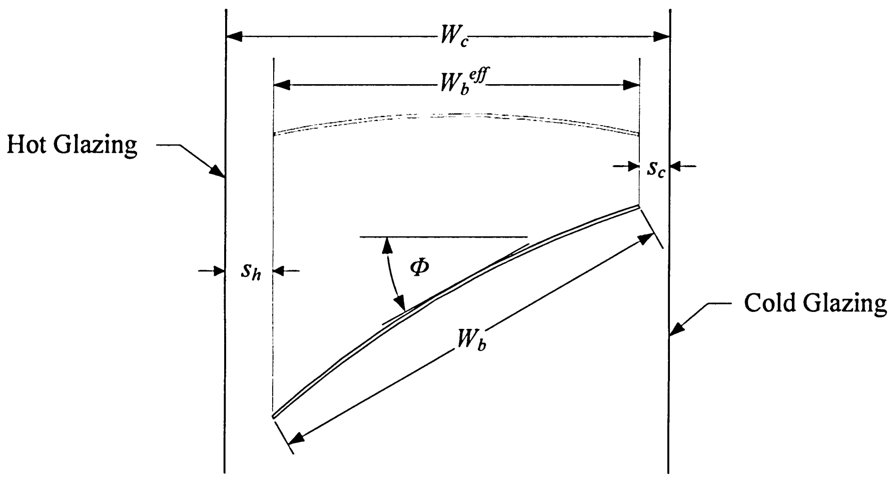

Figure 4.4: Effective width of a rotated slat

The dimensionless effective blind width can be calculated using equation 4.3. The main purpose of this expression is to develop a rough qualitative generalization for discussion purposes.

$$\frac{W_b^{eff}}{W_c} = \frac{W_c - (s_h + s_c)}{W_c} = \frac{W_b}{W_c}\cos(\Phi) \qquad (4.3)$$

The following graph shows the comparison between the average Nusselt numbers for W_b^{eff} / W_c in the range from 0.46 to 0.65 for slat angles of 0° and 45°. For example, if the slat angle is equal to 45°, a W_b / W_c ratio of 0.65, 0.8, and 0.9 would be equivalent to a W_b^{eff} / W_c ratio of 0.46, 0.57, and 0.64. For both Rayleigh numbers, 2 x 10^4 and 10^5, the two corresponding curves show a close agreement. This may also be of value for correlation purposes.

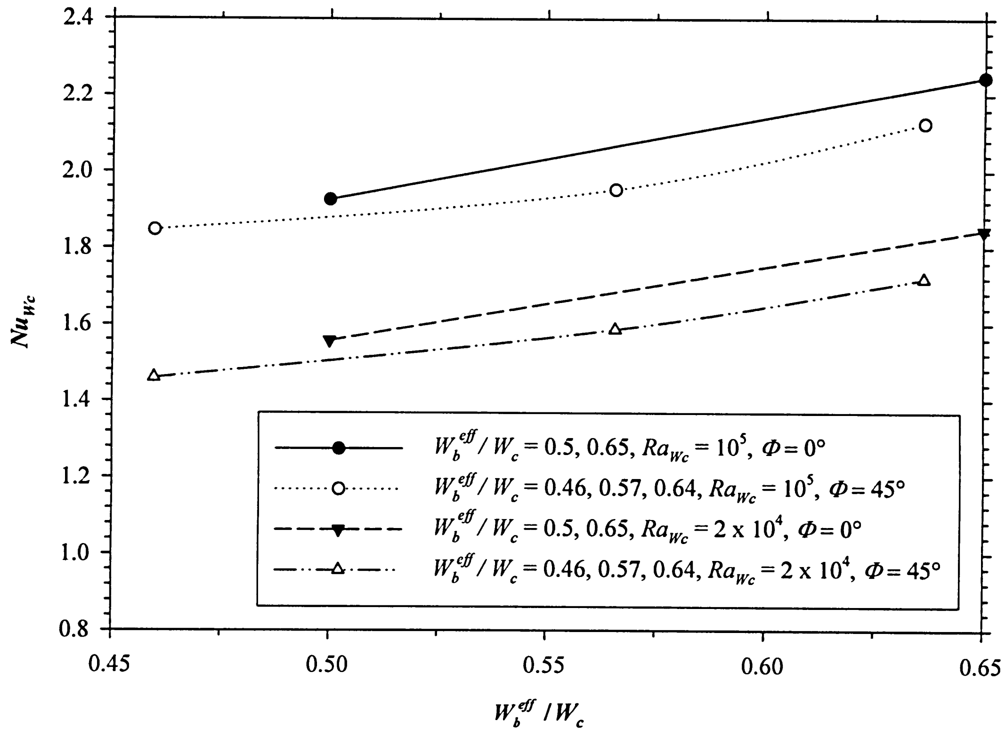

Figure 4.5: Effect of effective blind width on average Nusselt number for slat angles of 0° and 45° (Ra_{Wc} = 2 x 10^4 and 10^5, A = 60, W_b / W_c = 0.5 and 0.65, k_b / k_f = 4600, Φ = 0° and 45°)

Figures 4.6 to 4.8 illustrate the effect of the blind width to cavity width ratio on the Nusselt number for a wide range of Rayleigh numbers and slat angles of 0°, 45°, and 75°. Figure 4.6 (Φ = 0°) illustrates that Nusselt number increases as the W_b / W_c ratio increases, for the studied range of Rayleigh numbers. In Figure 4.7 (Φ = 45°), the trend of the curves is similar to the ones found in Figure 4.6 ($\Phi = 0°$), but there is an overall decrease and a closer distribution of Nusselt number. Figure 4.8 ($\Phi = 75°$) illustrates a very close distribution of Nusselt number for all W_b / W_c ratios. As might be expected, the W_b / W_c ratio has a very weak effect on Nusselt number for high slat angles.

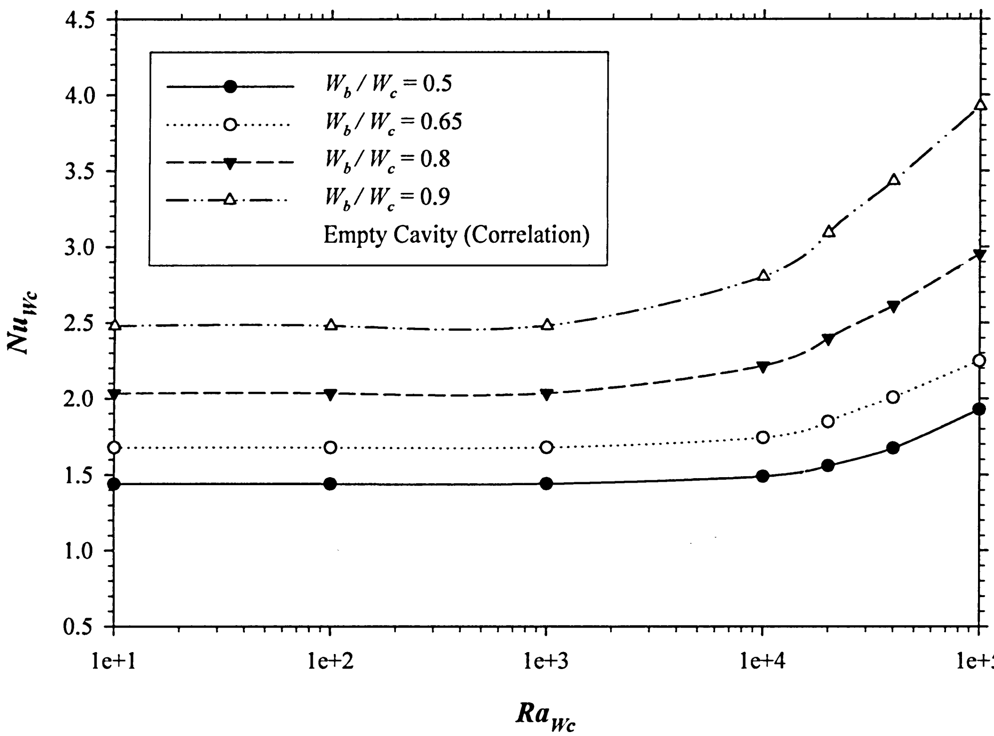

Figure 4.6: Effect of dimensionless blind width on average Nusselt number for a slat angle of 0° (Ra_{Wc} = 10 to 10^5, $A = 60$, $W_b / W_c = 0.5$ to 0.9, $k_b / k_f = 4600$, $\Phi = 0°$)

Interestingly, as Rayleigh number increases, the order of the curves from highest to lowest Nusselt number in the conduction regime is inverted at some point. This is evident in Figure 4.8 ($\Phi = 75°$) and can be seen in its early stages in Figure 4.7 ($\Phi = 45°$). If the aspect ratio is reduced to 20 (results not shown), this trend would be clearly evident at $\Phi = 45°$ and 75° and in its early stages for $\Phi = 0°$.

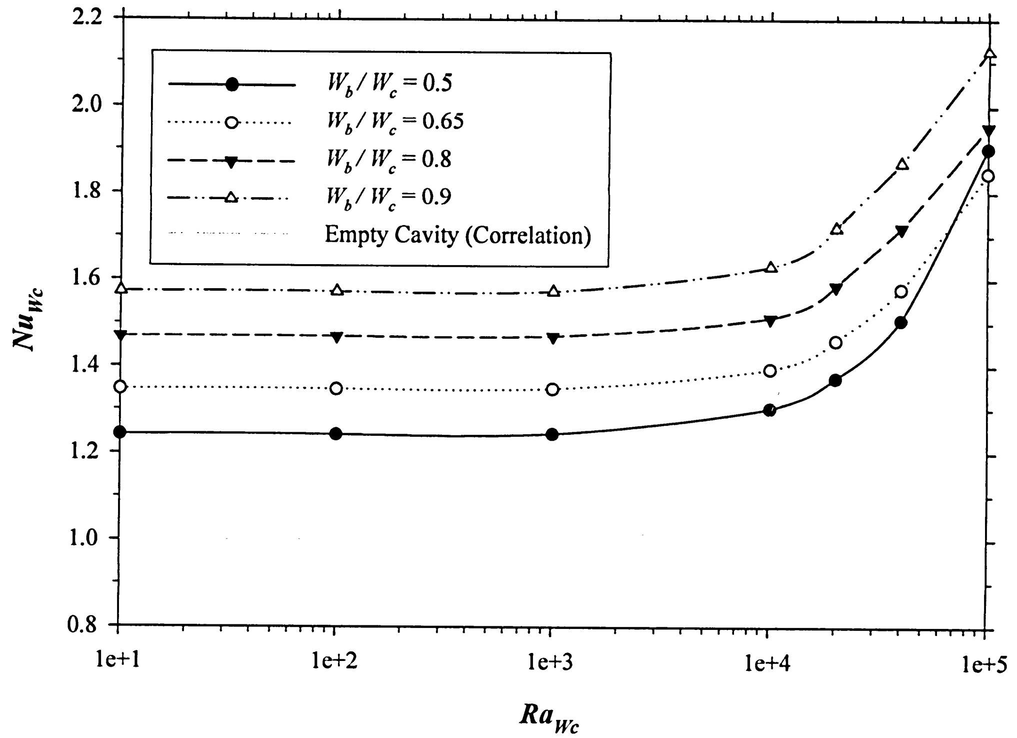

Figure 4.7: Effect of dimensionless blind width on average Nusselt number for a slat angle of 45° ($Ra_{Wc} = 10$ to 10^5, $A = 60$, $W_b / W_c = 0.5$ to 0.9, $k_b / k_f = 4600$, $\Phi = 45°$)

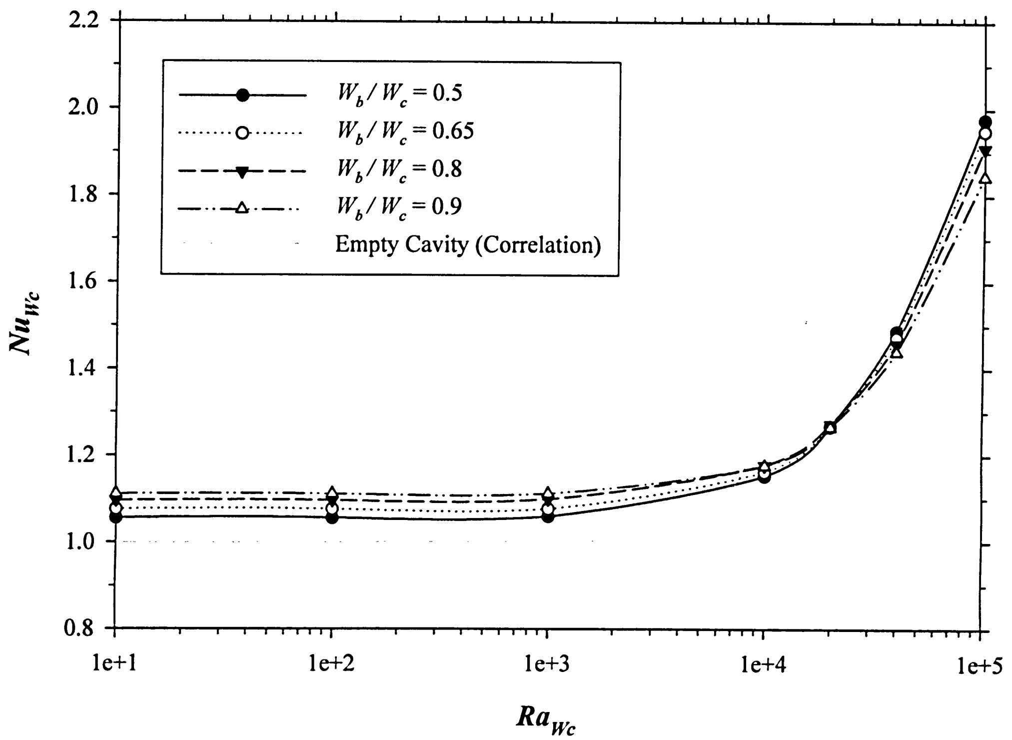

Figure 4.8: Effect of dimensionless blind width on average Nusselt number for a slat angle of 75° ($Ra_{Wc} = 10$ to 10^5, $A = 60$, $W_b / W_c = 0.5$ to 0.9, $k_b / k_f = 4600$, $\Phi = 75°$)

Figures 4.9 to 4.14 illustrate the corresponding temperature and stream function contours for a Rayleigh number of 10^5 and W_b / W_c ratios of 0.5 and 0.9 at the three slat angles studied. A full cavity is shown along with an enlarged view of the top and bottom sections. Table 4.1 shows the corresponding maximum dimensionless stream function.

The temperature contours in Figure 4.9 ($W_b / W_c = 0.5$, $\Phi = 0°$) show that the blind's influence on the development and interaction between the two boundary layers is relatively weak near the top and bottom of the cavity. As the two boundary layers grow, the blind's influence becomes more apparent. In the stream function contours, the outer primary flow seems to be the dominant flow path.

The temperature and stream function contours in Figure 4.10 ($W_b / W_c = 0.9$, $\Phi = 0°$) clearly demonstrate the three factors that affect the heat transfer rate. In the temperature contours, a high gradient is apparent between the slat tip-to-glazing spacings due to the thermal conduction in the near isothermal blind slats. The slats act like a *thermal bridge* across the two glazings, thereby increasing the heat transfer. From Table 4.1, the $W_b / W_c = 0.9$ and $\Phi = 0°$ configuration indicates a relatively low maximum non-dimensional stream function value ($\psi^*_{max} = 0.0465$), which signifies a strong impeding effect on the buoyancy-driven flow, about four times less than the $W_b / W_c = 0.5$ and $\Phi = 0°$ configuration ($\psi^*_{max} = 0.190$). But, due to the blind redirecting the two counter-flowing boundary layers, a distinct secondary recirculating flow is well developed between adjacent slats. This enhances the thermal boundary layer interaction, as well as the cross-cavity flow. These two factors, along with the thermal bridging effect, more than compensate for the relatively weak buoyancy-driven flow. This results in the highest Nusselt number curve for both low and high Rayleigh numbers, as shown in Figure 4.6.

The temperature contours in Figure 4.11 ($W_b / W_c = 0.5$, $\Phi = 45°$) show that the blind's influence on the development and interaction between the two boundary layers is fairly weak near the top and bottom of the cavity. As the two boundary layers grow, the blind's influence becomes slightly more apparent. In the stream function contours, the outer primary flow seems to be the dominant flow path.

The temperature contours in Figure 4.12 ($W_b / W_c = 0.9$, $\Phi = 45°$) show that the blind's influence on the development and interaction between the two boundary layers is quite strong, even in the top and bottom of the cavity. Despite having a W_b / W_c ratio near unity, the isotherms do not show a strong thermal bridging effect due to the relatively wide slat tip-to-glazing spacing. From Table 4.1, the impeding effect on the buoyancy-driven flow is about 2.5 times less than the case above ($W_b / W_c = 0.5$, $\Phi = 45°$). Due to the blind's redirection of the two boundary layers, the secondary recirculating flow between the slats is developed. This again enhances the cross-cavity flow, which more than compensates for the relatively weak buoyancy-driven flow, thereby increasing the Nusselt number, as shown in Figure 4.7.

Figures 4.13 ($W_b / W_c = 0.5$, $\Phi = 75°$) and 4.14 ($W_b / W_c = 0.9$, $\Phi = 75°$) have very similar temperature contours. This is expected, as shown in Figure 4.8, the corresponding Nusselt number distributions are also very similar. The development of the two boundary layers is not influenced much when the slat angle is at 75°; however, their interaction is heavily influenced. When buoyancy-driven flow in an empty cavity is observed, it is apparent that the two adjacent boundary layers interact as they grow along the vertical walls (see Figures 1.3 to 1.5). The slats in this case act like a barrier between the two boundary layers, where their cross-cavity interaction is rather restricted or inhibited. This is apparent in the stream function contours in Figure 4.14, especially near the mid-height range of the cavity, where the stagnation pressure is assumed to be relatively low. Contrary to the two previous cases ($\Phi = 0°$ and 45°), for slat angle of 75°, the blind decreases the heat transfer by inhibiting the cross-cavity flow. Due to the comparatively wide slat tip-to-glazing spacing, especially for W_b / W_c ratio equal to 0.5, the thermal bridging effect is very low. As a result, at a slat angle of 75°, the Nusselt number is lower for almost all Rayleigh numbers (see Figures 4.15 to 4.18), despite the fact that the primary recirculating flow is the strongest (see Table 4.1).

As mentioned in Section 2.2, the *y offset* of the blind is set such that a seal is created with the bottom end-wall of the cavity when the blind is closed. However, a gap could exist between the blind and the top end-wall. This gap length varies for different cavity aspect ratio and blind width combinations, but it is always less than the blind width. It is worth mentioning that the extremes of the top gap length have a small effect (< 1%) on the convective heat transfer rate.

Table 4.1: Maximum dimensionless stream function, ψ^* ($Ra_{W_c} = 10^5$, $A = 20$ and 60, $W_b / W_c = 0.5$ and 0.9, $k_b / k_f = 4600$, $\Phi = 0°$, 45°, and 75°)

	$\Phi = 0°$	$\Phi = 45°$	$\Phi = 75°$	**Empty Cavity (Numerical)**
$W_b / W_c = 0.5$	0.190 (0.204)	0.284 (0.280)	0.352 (0.560)	0.427 (-)
$W_b / W_c = 0.9$	0.0465 (0.0475)	0.114 (0.114)	0.310 (0.405)	

Note: ( ) denotes a cavity aspect ratio of 60.

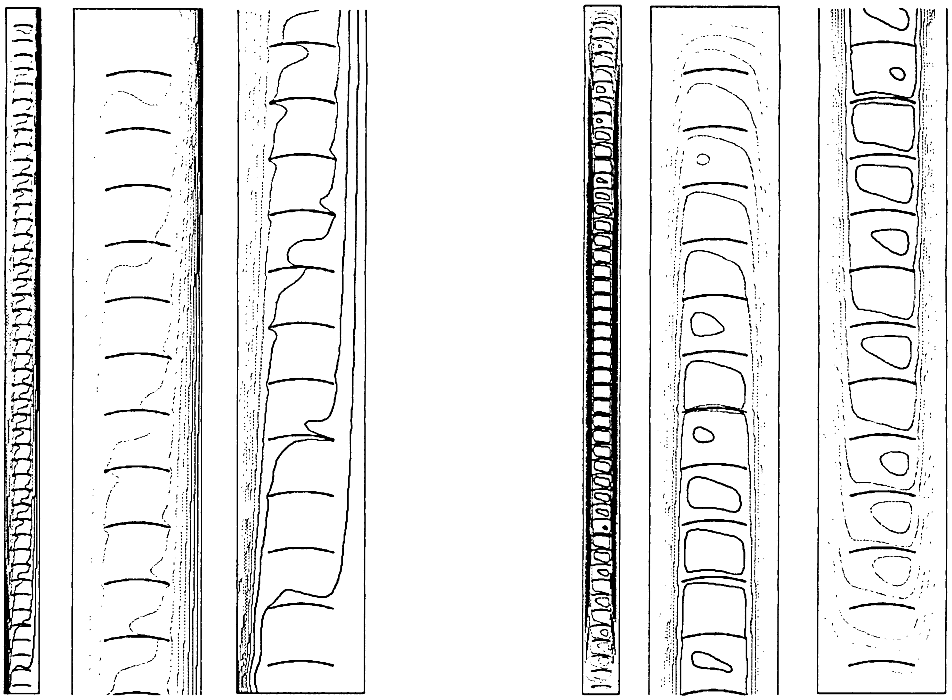

(a) T (b) ψ

Figure 4.9: (a) Temperature contours, (b) stream function contours ($\psi^*_{max} = 0.190$) ($Ra_{W_c} = 10^5$, $A = 20$, $W_b / W_c = 0.5$, $k_b / k_f = 4600$, $\Phi = 0°$)

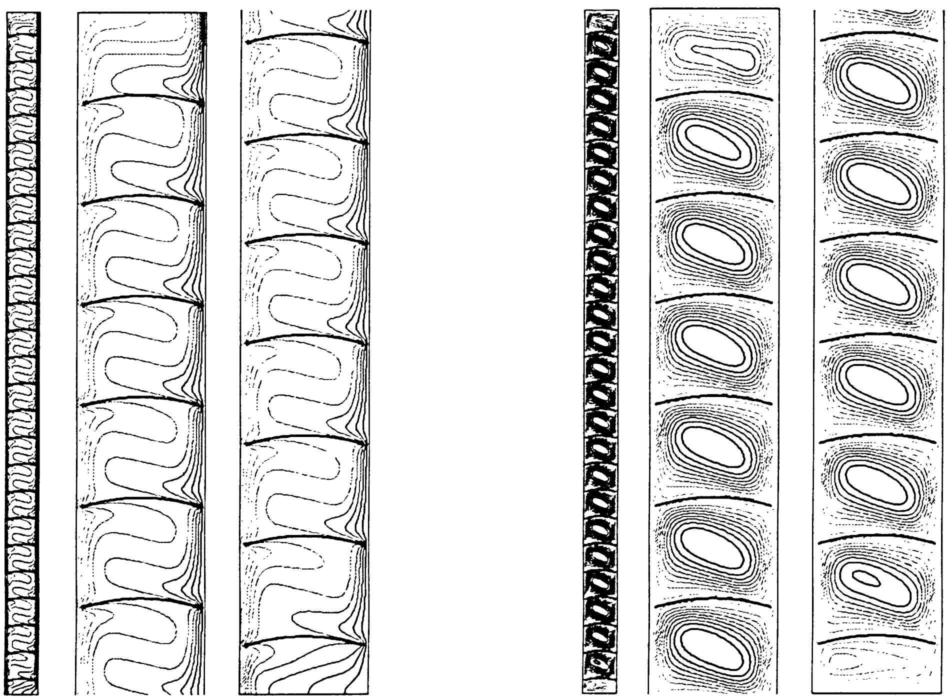

(a) T (b) ψ

Figure 4.10: (a) Temperature contours, (b) stream function contours ($\psi^*_{max} = 0.0465$) ($Ra_{W_c} = 10^5$, $A = 20$, $W_b / W_c = 0.9$, $k_b / k_f = 4600$, $\Phi = 0°$)

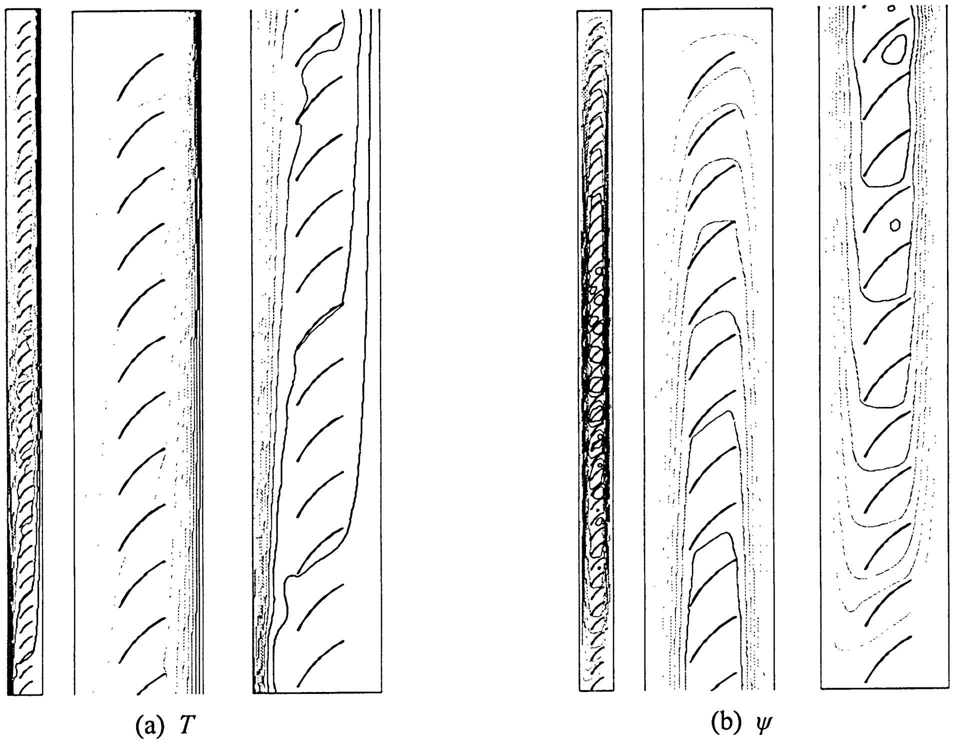

Figure 4.11: (a) Temperature contours, (b) stream function contours ($\psi^*_{max} = 0.284$) ($Ra_{Wc} = 10^5$, $A = 20$, $W_b / W_c = 0.5$, $k_b / k_f = 4600$, $\Phi = 45°$)

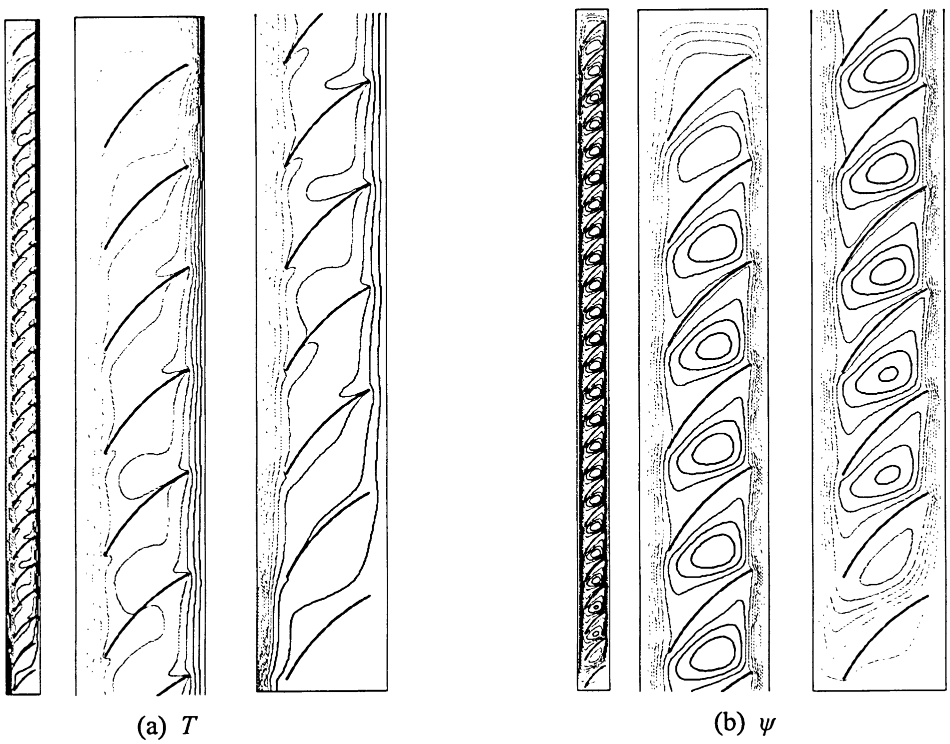

Figure 4.12: (a) Temperature contours, (b) stream function contours ($\psi^*_{max} = 0.114$) ($Ra_{Wc} = 10^5$, $A = 20$, $W_b / W_c = 0.9$, $k_b / k_f = 4600$, $\Phi = 45°$)

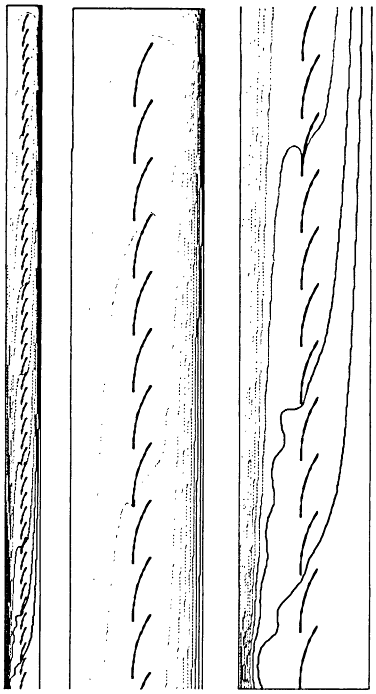

(a) T

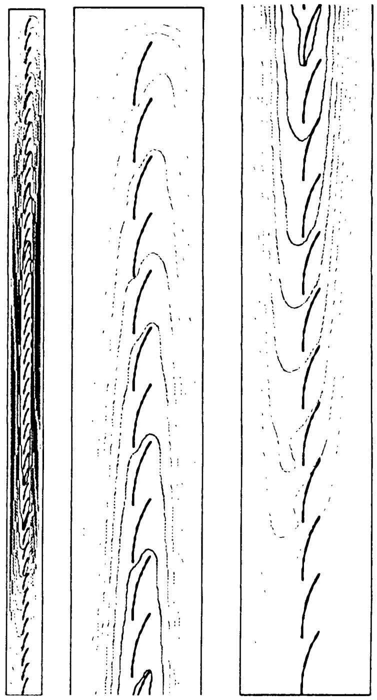

(b) ψ

Figure 4.13: (a) Temperature contours, (b) stream function contours ($\psi^*_{max} = 0.352$) ($Ra_{Wc} = 10^5$, $A = 20$, $W_b / W_c = 0.5$, $k_b / k_f = 4600$, $\Phi = 75°$)

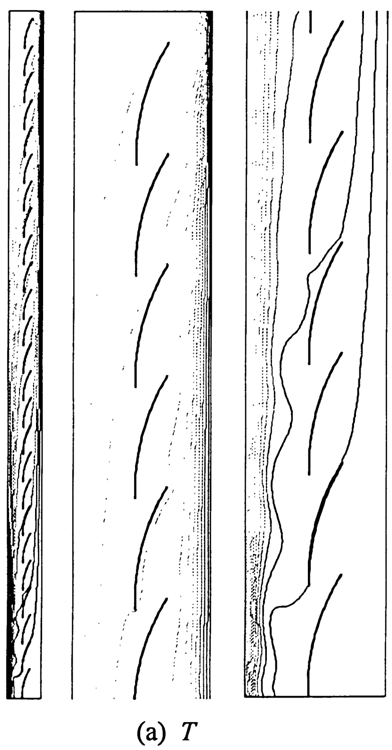

(a) T

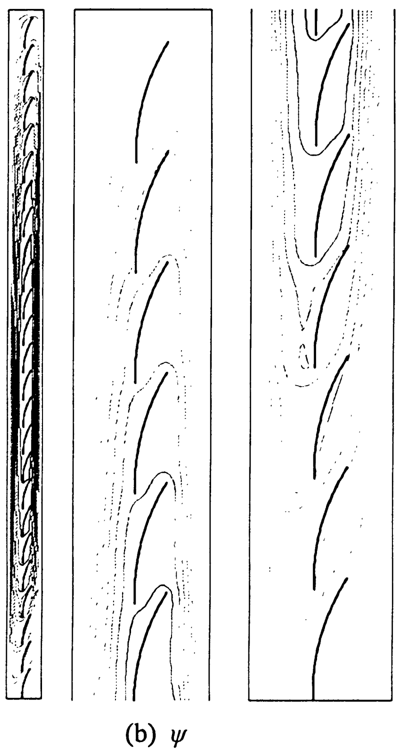

(b) ψ

Figure 4.14: (a) Temperature contours, (b) stream function contours ($\psi^*_{max} = 0.310$) ($Ra_{Wc} = 10^5$, $A = 20$, $W_b / W_c = 0.9$, $k_b / k_f = 4600$, $\Phi = 75°$)

4.2.3 Slat Angle Effect

Figures 4.15 to 4.18 illustrate the effect of the slat angle on the Nusselt number for a wide range of Rayleigh numbers and W_b / W_c ratios from 0.5 to 0.9. Only plots for an aspect ratio of 60 are presented. When comparing Figures 4.15 to 4.18 to Figures 4.6 to 4.8 from the previous section, a close resemblance can be seen, including the curve order inverting from the conduction regime to the convection dominated regime. This is due to the effective blind width generalization stated above. Therefore, the findings from the previous section, in regards to the Nusselt number behaviour, can apply for this section.

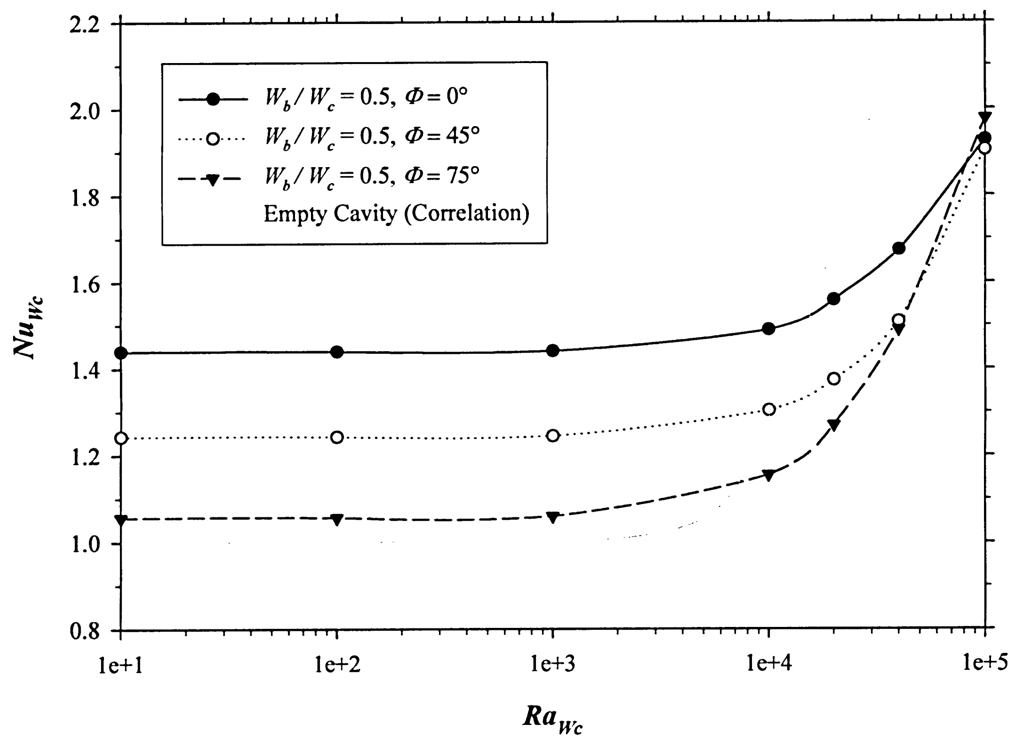

Figure 4.15: Effect of slat angle on average Nusselt number for a dimensionless blind width of 0.5 (Ra_{Wc} = 10 to 10^5, A = 60, W_b / W_c = 0.5, k_b / k_f = 4600, Φ = 0°, 45°, and 75°)

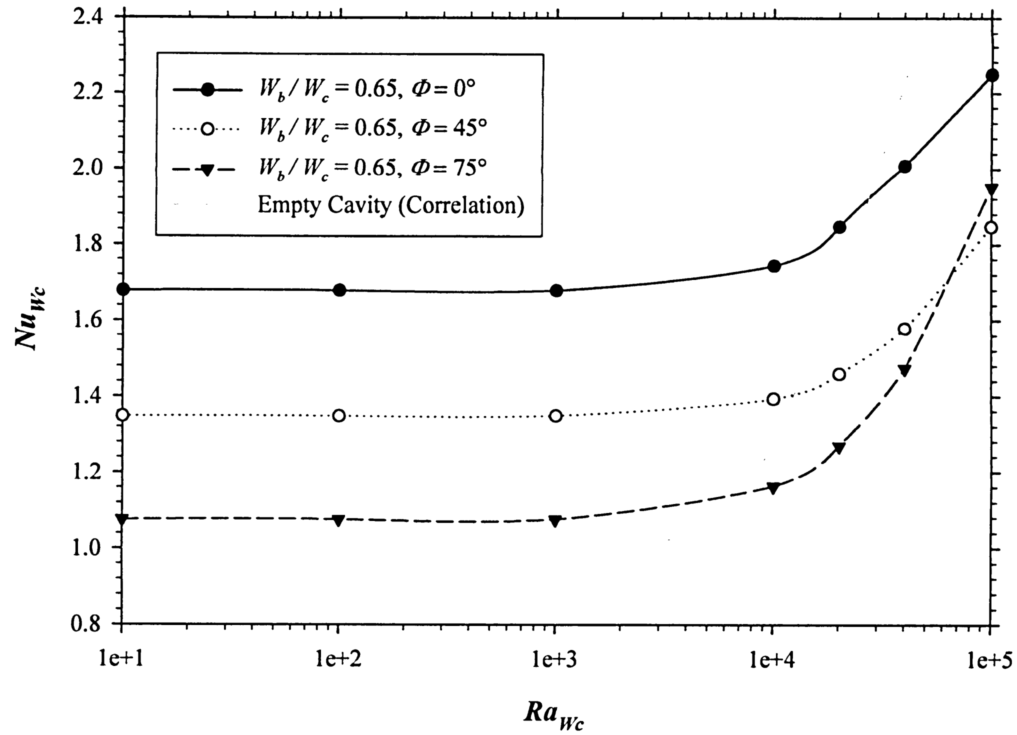

Figure 4.16: Effect of slat angle on average Nusselt number for a dimensionless blind width of 0.65 (Ra_{Wc} = 10 to 10^5, $A = 60$, $W_b / W_c = 0.65$, $k_b / k_f = 4600$, $\Phi = 0°$, 45°, and 75°)

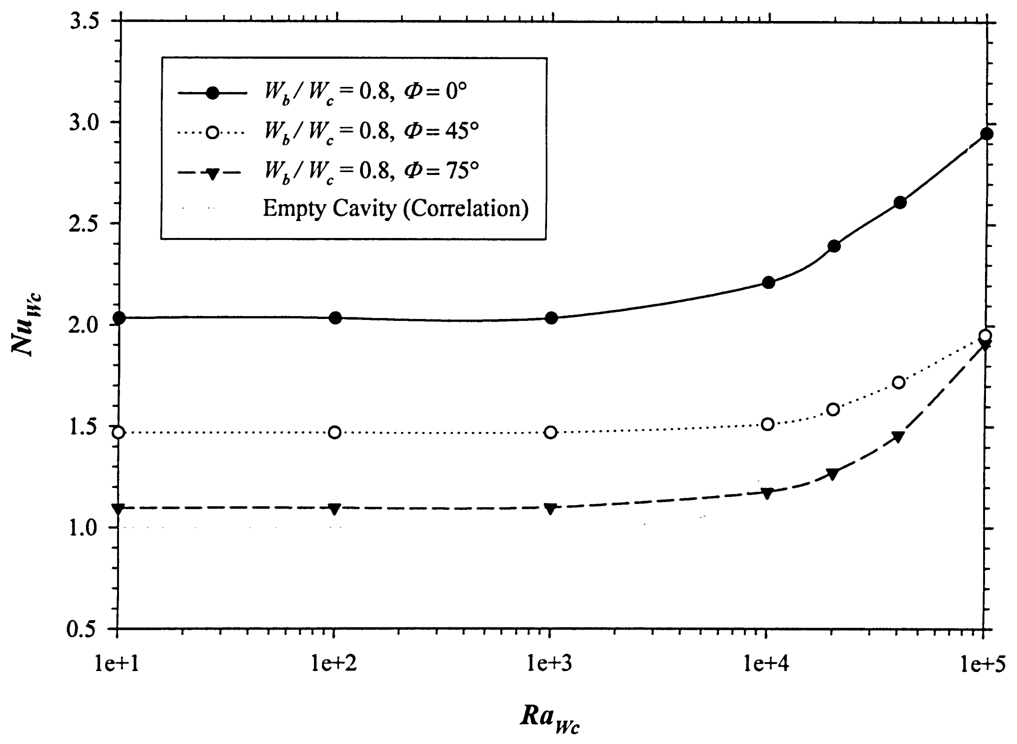

Figure 4.17: Effect of slat angle on average Nusselt number for a dimensionless blind width of 0.8 (Ra_{Wc} = 10 to 10^5, $A = 60$, $W_b / W_c = 0.8$, $k_b / k_f = 4600$, $\Phi = 0°$, 45°, and 75°)

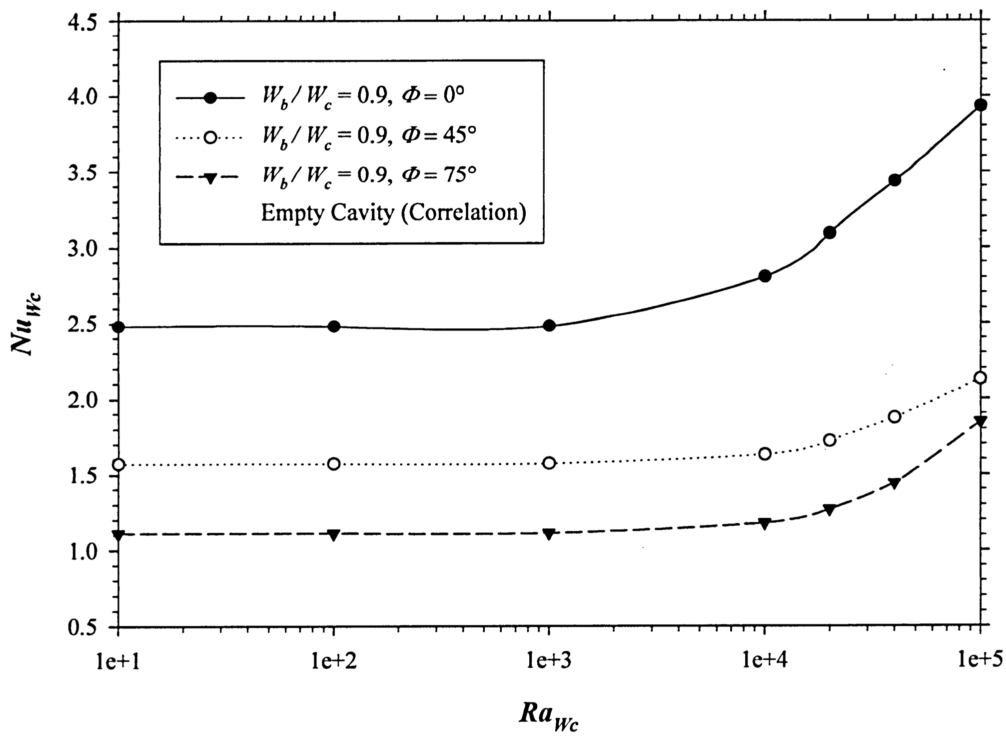

Figure 4.18: Effect of slat angle on average Nusselt number for a dimensionless blind width of 0.9 (Ra_{Wc} = 10 to 10^5, A = 60, W_b / W_c = 0.9, k_b / k_f = 4600, Φ = 0°, 45°, and 75°)

4.2.4 Effective Blind Width Summary

The blind's impeding effect on the buoyancy-driven flow depends mainly on the dimensionless effective blind width. When this parameter is near unity, the strength of the buoyancy-driven flow is reduced (see Table 4.1). Having stated this, the Nusselt number correlations for an empty cavity (Equations 1.10 and 1.11) naturally suggests that the convective heat transfer rate increases as the strength of the flow increases. This is not the situation with a blind in a cavity, where the case with the weakest buoyancy-driven flow has the highest heat transfer rate. This is caused by two effects; the first is the thermal bridging effect of the (high conductivity) slats, which is discussed in detail in the following section, and the second is the blind redirecting the two counter-flowing boundary layers by enhancing the cross-cavity flow. As stated, these two effects more than compensate for the reduction of the heat transfer rate due to the decrease in the strength of the buoyancy-driven flow, especially the latter. The primary recirculating flow moving parallel to the glazings is deflected, causing secondary recirculating flow, as shown in the stream function contours in Figure 4.10. The array of adjacent slats and the two glazings, which contain the secondary flow, form a stacked cavity formation with an aspect ratio of about one. As mentioned in the Chapter 1, the studies of ElSherbiny et al. [11] suggest that Nusselt number increases as aspect ratio is decreased to unity. Evidently, the *stacking effect* increases the heat transfer, where the cross-over occurs between every slat and not just at the top and bottom of the cavity. Therefore, depending on the blind's configuration, the heat transfer is increased if the flow travel is predominantly across the cavity and reduced if the flow is predominantly parallel to the glazing. In other words, the amount of flow in the x direction is more influential on the heat transfer rate than the amount of flow in the y direction. The Nusselt number increases by about 47% and 100% between the smallest ($W_b / W_c = 0.5$, $\Phi = 75°$) and largest ($W_b / W_c = 0.9$, $\Phi = 0°$) effective blind widths, for a cavity aspect ratio of 20 and 60, respectively, at a Rayleigh number of 10^5.

4.2.5 Blind to Fluid Thermal Conductivity Ratio Effect

Figures 4.19 to 4.21 illustrate the effect of the blind to fluid thermal conductivity ratios of 15 and 4600 on the Nusselt number for W_b / W_c ratio of 0.5 and 0.9. Figure 4.19 ($\Phi = 0°$) shows that the Nusselt number is weakly affected by the W_b / W_c ratio when the $k_b / k_f = 15$, for Rayleigh numbers in the conduction regime. For higher Rayleigh numbers, the W_b / W_c ratio does have a significant effect. For example, the Nusselt number for $W_b / W_c = 0.9$ and $k_b / k_f =$ 15 considerably increases, despite having a flow strength one order of magnitude less than that of an empty cavity (see Table 4.2). This clearly exemplifies the stacking effect. Although the

s_h and s_c spacings are small, the thermal bridging effect is low because the k_b / k_f ratio is relatively low. As the Rayleigh number increases, the effect of the k_b / k_f ratio becomes less significant. Figures 4.20 (Φ = 45°) and 4.21 (Φ = 75°) show a similar effect, where the thermal conductivity ratio has a smaller effect on Nusselt number, particularly at a slat angle of 75°. As the Rayleigh number increases, the boundary layers become increasingly thin as they develop along the two glazing surfaces, and recede away from the slat tips. As a result, the thermal bridging effect is less influential on the Nusselt number. This is evident, again in Figures 4.19 to 4.21, where the curves for both high and low k_b / k_f ratios with a similar W_b / W_c ratio start to converge as the Rayleigh number increases. Overall, the greatest increase in the Nusselt number is about 125% in the conduction regime (Ra_{Wc} = 10 – 1000) and about 30% at a Rayleigh number of 10^5, for the W_b / W_c = 0.9 and Φ = 0° configuration.

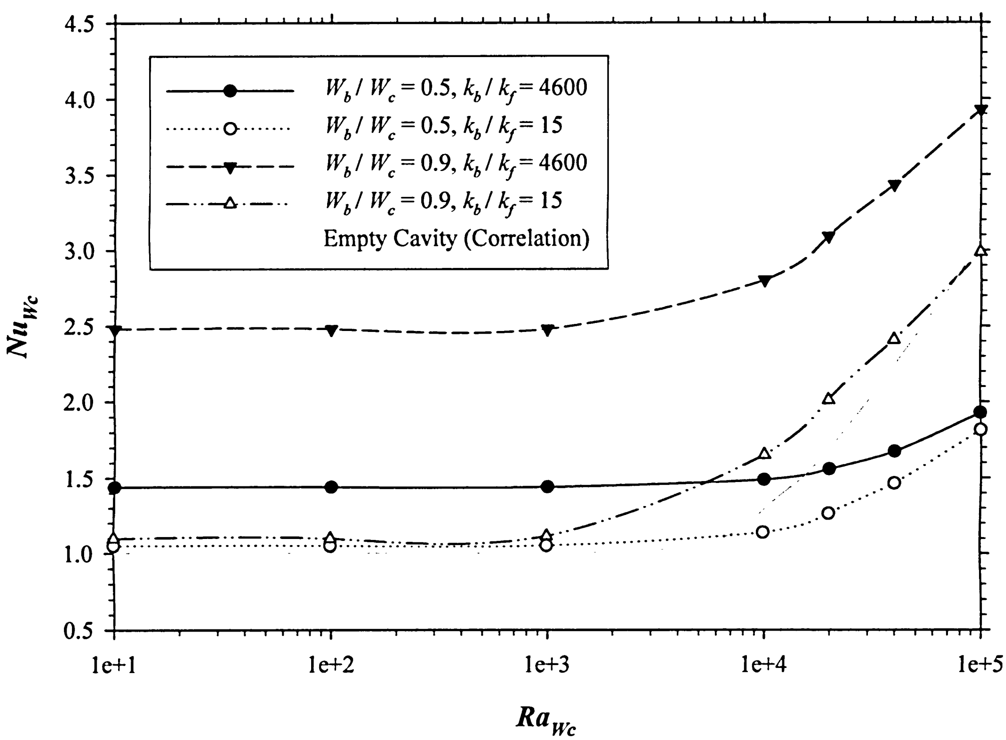

Figure 4.19: Effect of blind thermal conductivity on average Nusselt number for a slat angle of 0° (Ra_{Wc} = 10 to 10^5, A = 60, W_b / W_c = 0.5 and 0.9, k_b / k_f = 15 and 4600, Φ = 0°)

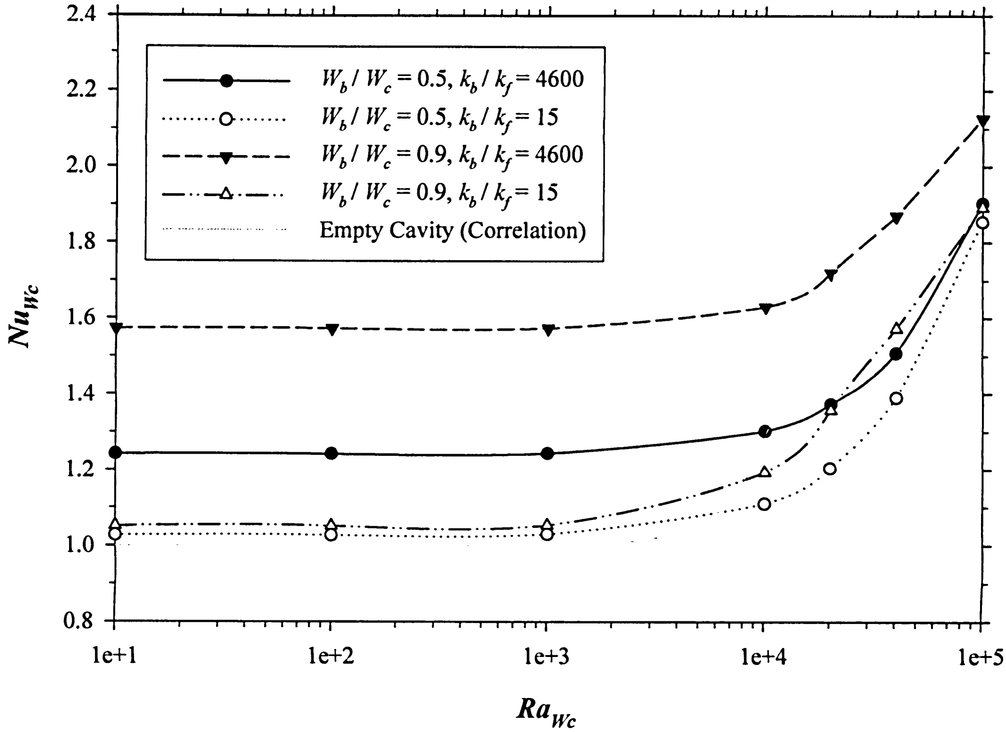

Figure 4.20: Effect of blind thermal conductivity on average Nusselt number for a slat angle of 45° (Ra_{Wc} = 10 to 10^5, $A = 60$, $W_b / W_c = 0.5$ and 0.9, $k_b / k_f = 15$ and 4600, $\Phi = 45°$)

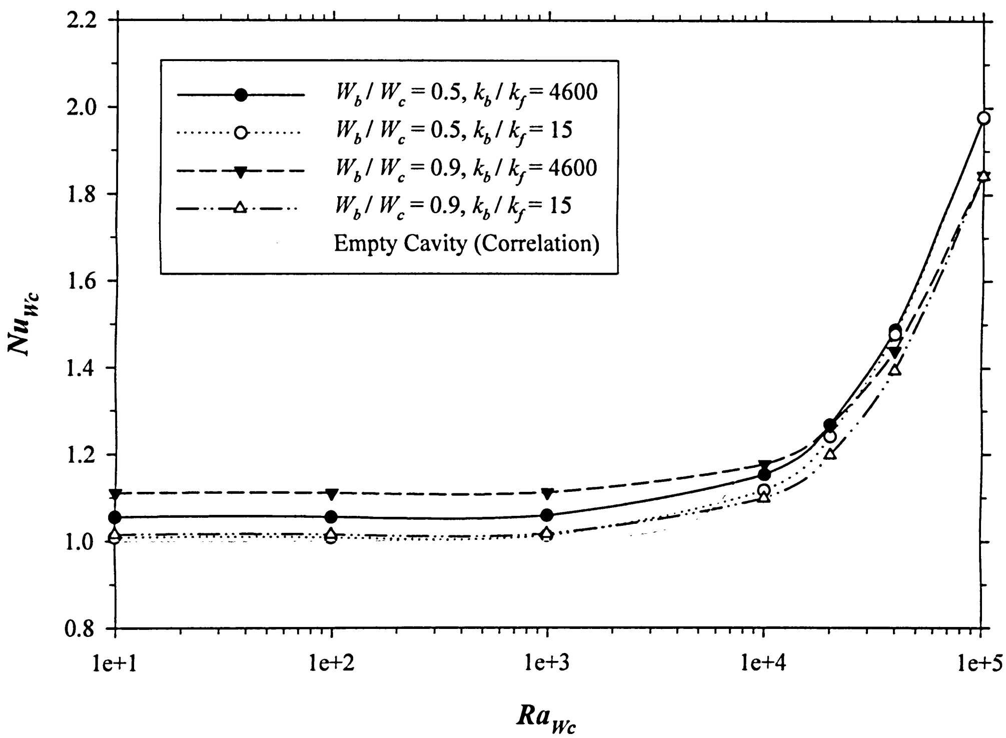

Figure 4.21: Effect of blind thermal conductivity on average Nusselt number for a slat angle of 75° (Ra_{Wc} = 10 to 10^5, $A = 60$, $W_b / W_c = 0.5$ and 0.9, $k_b / k_f = 15$ and 4600, $\Phi = 75°$)

Figures 4.22 to 4.27 illustrate the corresponding temperature and stream function contours for a Rayleigh number of 10^5 and W_b / W_c ratio of 0.9 for k_b / k_f ratios of 15 and 4600 at the three slat angles studied. Again, a full cavity is shown along with an enlarged view of the top and bottom sections. Table 4.2 shows the maximum dimensionless stream function for both k_b / k_f ratios and slat angles of 0°, 45°, and 75°. The contours in Figures 4.22, 4.24, and 4.26 have been presented in Section 4.2.2 as Figures 4.10, 4.12, and 4.14, respectively. They are presented again for comparison to Figures 4.23, 4.25, and 4.27, in order to see the qualitative effect of the two k_b / k_f ratios.

Table 4.2: Maximum dimensionless stream function, ψ^* ($Ra_{Wc} = 10^5$, $A = 20$, $W_b / W_c = 0.9$, $k_b / k_f = 15$ and 4600, $\Phi = 0°$, 45°, and 75°)

	$\Phi = 0°$	$\Phi = 45°$	$\Phi = 75°$	Empty Cavity (Numerical)
$k_b/k_f = 15$	0.0500	0.125	0.310	0.427
$k_b/k_f = 4600$	0.0465	0.114	0.310	

In Figure 4.23 ($k_b / k_f = 15$, $\Phi = 0°$), it is apparent that the isotherms are more uniformly distributed across the cavity width when compared to the contours in Figure 4.22 ($k_b / k_f =$ 4600, $\Phi = 0°$). This normally results in a lower heat transfer rate (weak thermal bridging effect), as shown in Figure 4.19. Figures 4.24 ($k_b / k_f = 4600$, $\Phi = 45°$) and 4.25 ($k_b / k_f = 15$, $\Phi = 45°$) illustrate the same effect as the $\Phi = 0°$ case. In Figures 4.26 ($k_b / k_f = 4600$, $\Phi = 75°$) and 4.27 ($k_b / k_f = 15$, $\Phi = 75°$), it is apparent that the k_b / k_f ratio has almost no effect on the temperature field. Overall, for the same slat angle, the stream function contours for both k_b / k_f ratio cases are very similar.

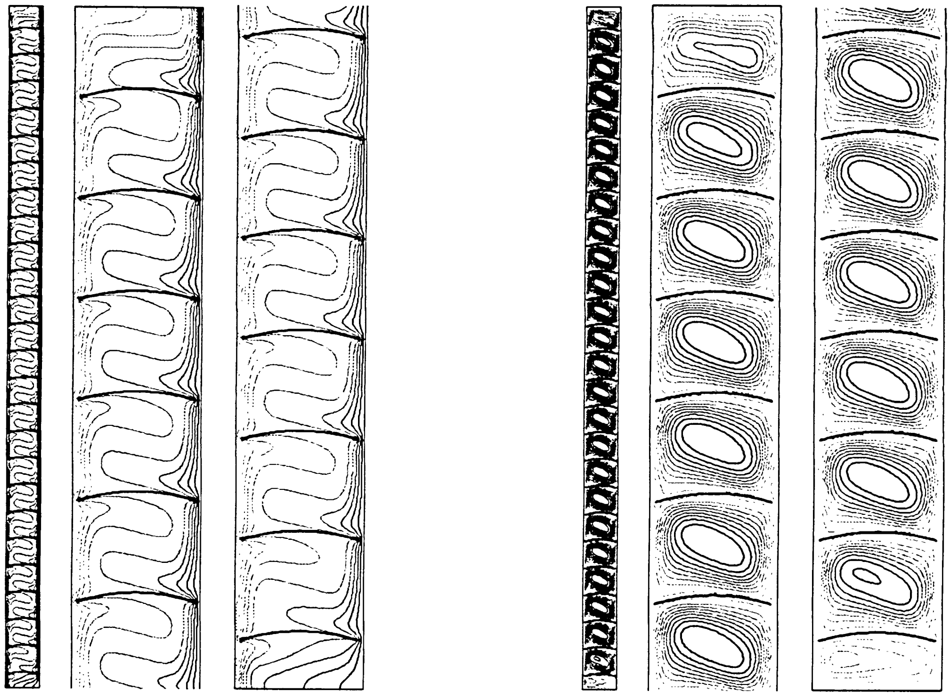

(a) T (b) ψ

Figure 4.22: (a) Temperature contours, (b) stream function contours ($\psi^*_{max} = 0.0465$) ($Ra_{W_c} = 10^5, A = 20, W_b / W_c = 0.9, k_b / k_f = 4600, \Phi = 0°$)

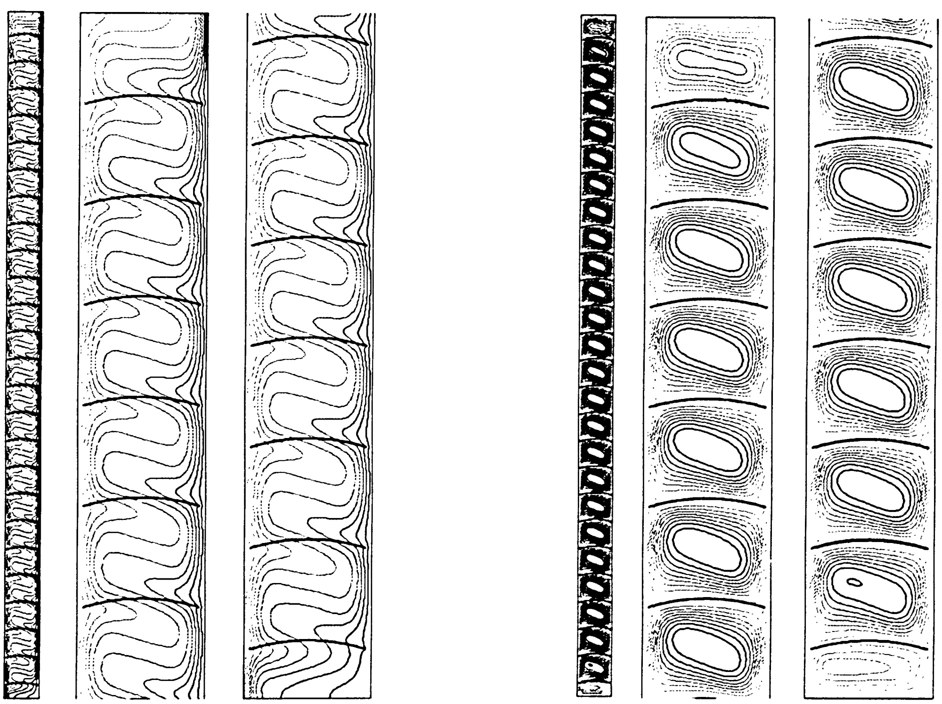

(a) T (b) ψ

Figure 4.23: (a) Temperature contours, (b) stream function contours ($\psi^*_{max} = 0.0496$) ($Ra_{W_c} = 10^5, A = 20, W_b / W_c = 0.9, k_b / k_f = 15, \Phi = 0°$)

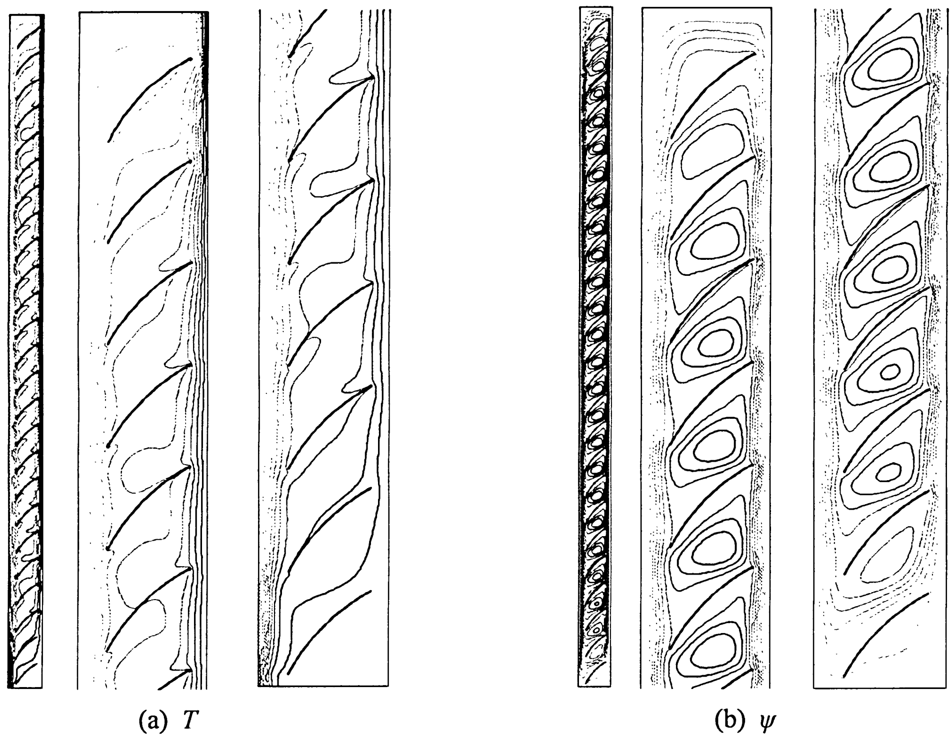

Figure 4.24: (a) Temperature contours, (b) stream function contours (ψ^{*}_{max} = 0.114) (Ra_{Wc} = 10^5, A = 20, W_b / W_c = 0.9, k_b / k_f = 4600, Φ = 45°)

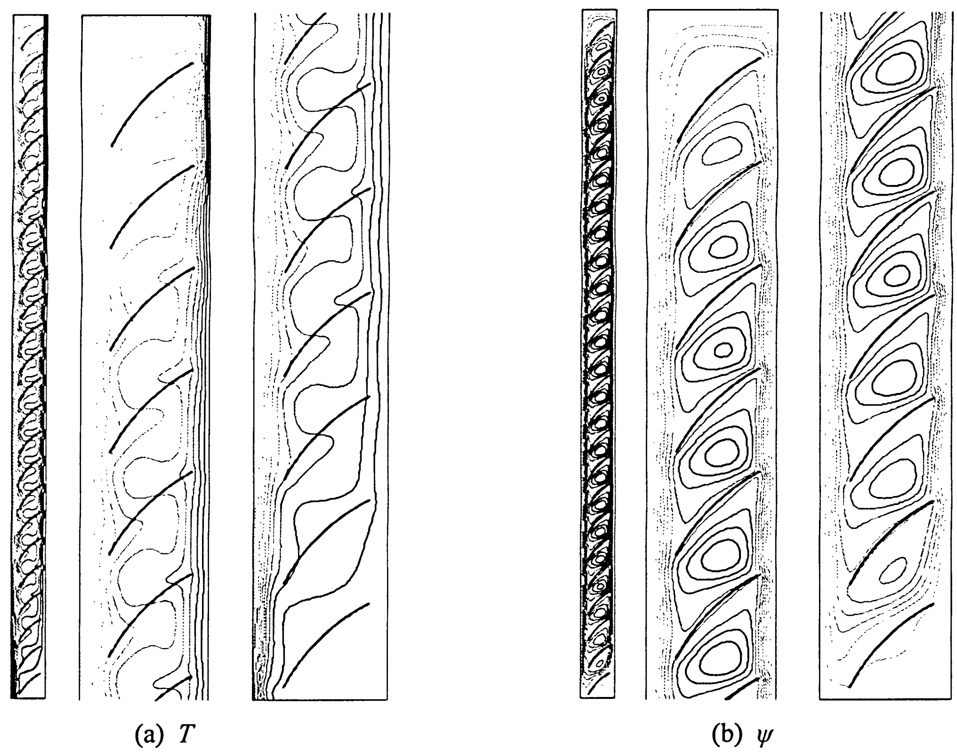

Figure 4.25: (a) Temperature contours, (b) stream function contours (ψ^{*}_{max} = 0.125) (Ra_{Wc} = 10^5, A = 20, W_b / W_c = 0.9, k_b / k_f = 15, Φ = 45°)

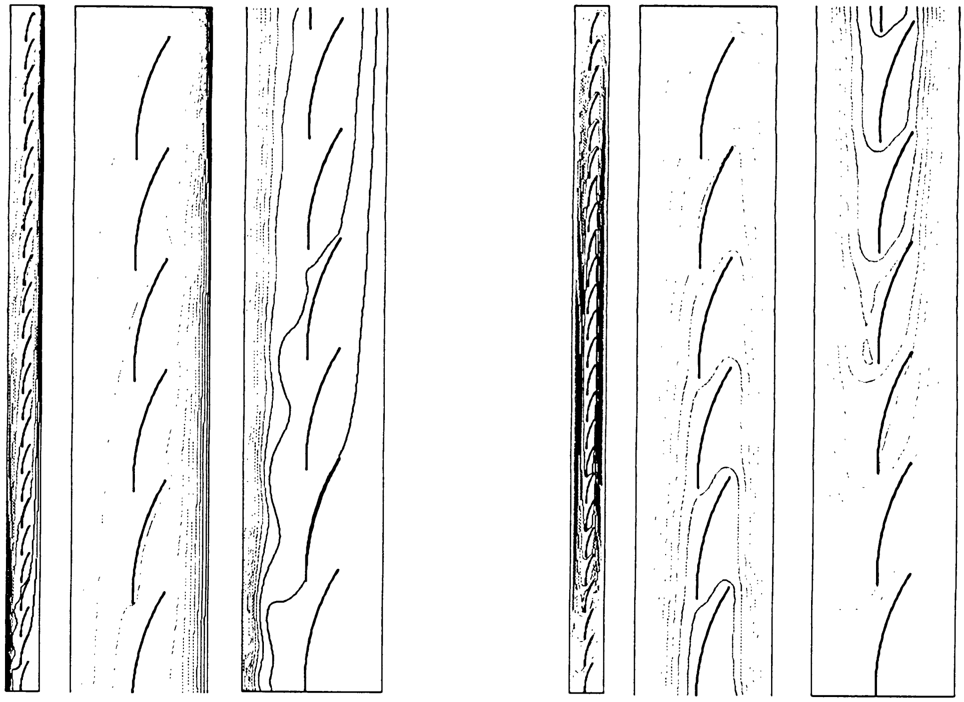

(a) T (b) ψ

Figure 4.26: (a) Temperature contours, (b) stream function contours (ψ^*_{max} = 0.310) (Ra_{W_c} = 10^5, A = 20, W_b / W_c = 0.9, k_b / k_f = 4600, Φ = 75°)

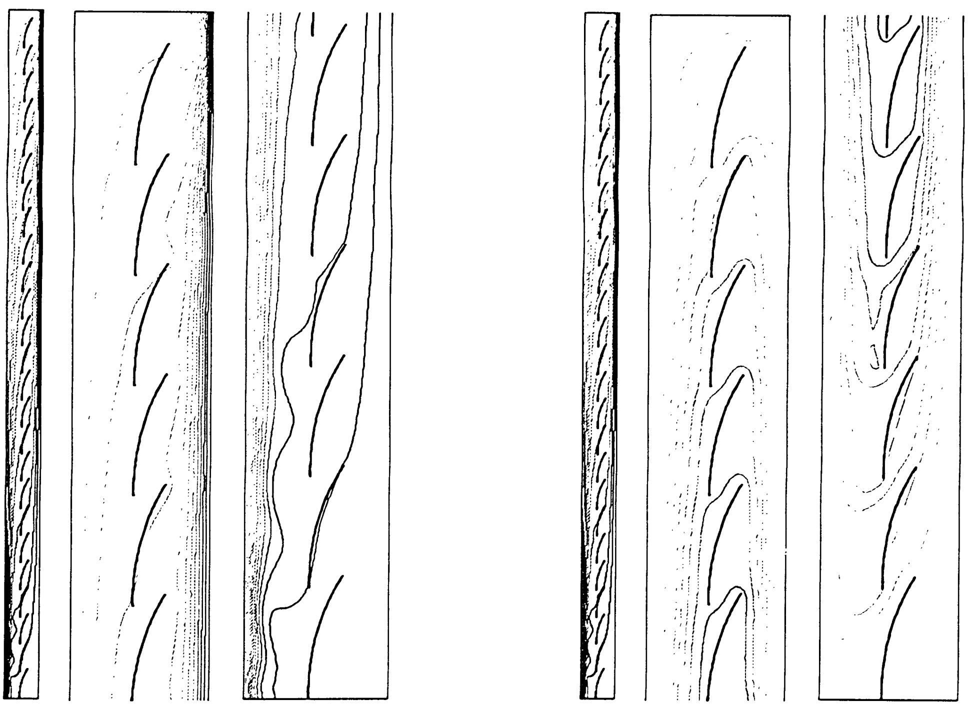

(a) T (b) ψ

Figure 4.27: (a) Temperature contours, (b) stream function contours (ψ^*_{max} = 0.310) (Ra_{W_c} = 10^5, A = 20, W_b / W_c = 0.9, k_b / k_f = 15, Φ = 75°)

Figures 4.28 ($\Phi = 0°$) and 4.31 ($\Phi = 45°$ and $75°$) show the corresponding local Nusselt number distributions for the same parameters. In Figure 4.28 ($\Phi = 0°$), both curves are generally periodic with maxima at the same spatial frequency as the slat pitch. It is apparent that the higher k_b / k_f ratio curve has sharp and substantial maxima at the same vertical locations as the slat tips, and a higher average Nusselt number. This is again caused by the thermal bridging effect of the slats. Figure 4.29 illustrates this by combining the plot in Figure 4.28 with the corresponding temperature field contours in Figure 4.22. The lower k_b / k_f ratio curve has maxima that occur between the slats. This is due to the dominant secondary recirculating flow (from the stacking effect), as seen in the corresponding stream function contours in Figure 4.23. Figure 4.30 illustrates this by combining the plot in Figure 4.28 with the corresponding temperature field contours in Figure 4.23.

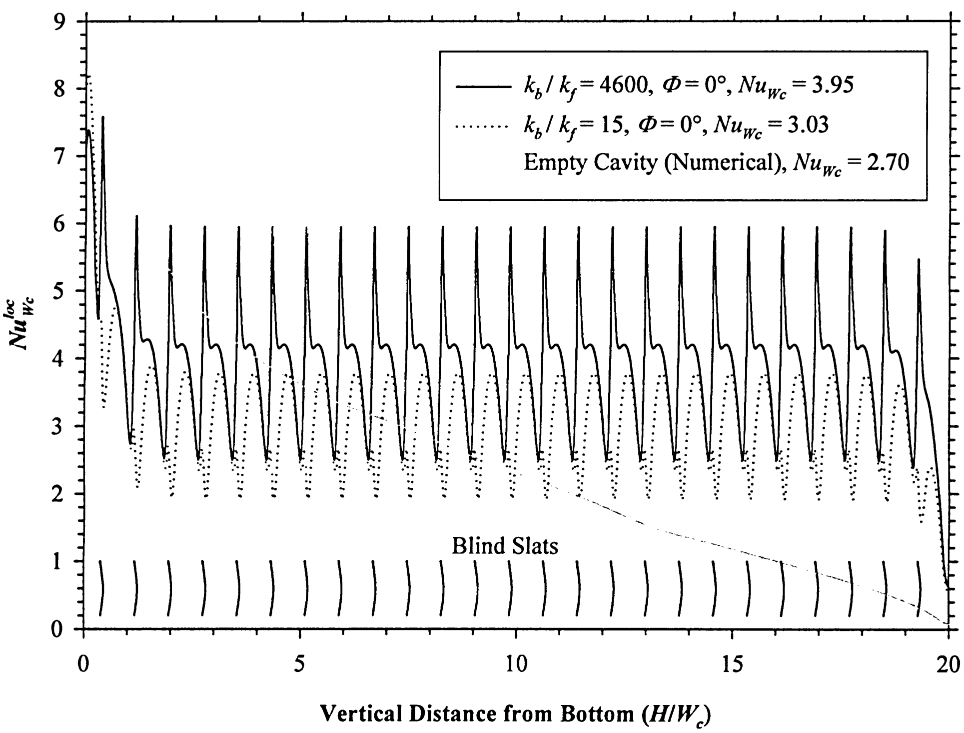

Figure 4.28: Effect of blind thermal conductivity on hot-wall local Nusselt number distribution for a slat angle of 0° ($Ra_{Wc} = 10^5$, $A = 20$, $W_b / W_c = 0.9$, $k_b / k_f = 15$ and 4600, $\Phi = 0°$)

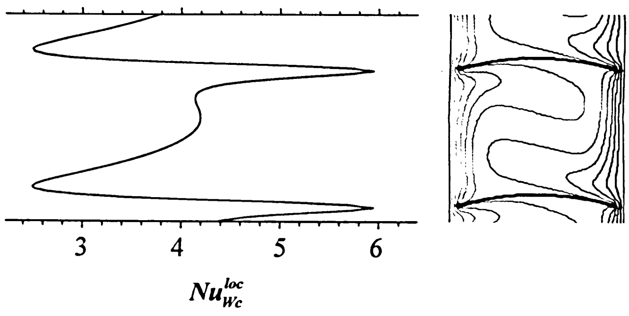

Figure 4.29: Hot-wall local Nusselt number plot and temperature field contours for k_b / k_f = 4600

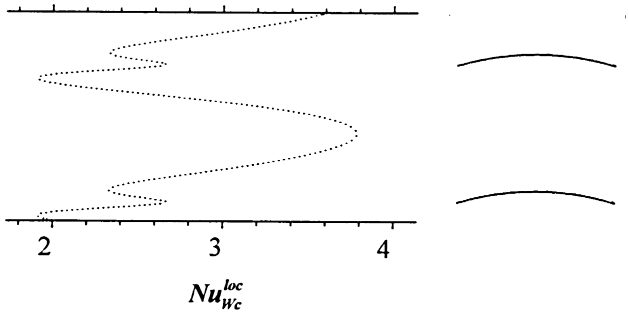

Figure 4.30: Hot-wall local Nusselt number plot and temperature field contours for k_b / k_f = 15

In Figure 4.30, the slight *recovery* in the Nusselt number at the same vertical location as the slat tip could be a combination of thermal bridging and flow acceleration, since the k_b / k_f ratio is quite low (approximately 307 times less than the k_b / k_f = 4600 case).

In Figure 4.31, both curves for slat angle of 45° have comparable average Nusselt numbers and again are generally periodic with maxima at the same spatial frequency as the slat pitch. The maxima in both curves occur between the slats, indicating that the thermal bridging effect is weak, but not the stacking effect. As seen in the corresponding stream function contours in Figures 4.24 (k_b / k_f = 4600, Φ = 45°) and 4.25 (k_b / k_f = 15, Φ = 45°), the secondary recirculating flows are well developed.

Again in Figure 4.31, both curves for a slat angle of 75° have identical local and average Nusselt numbers and no local periodic maxima. Therefore, the k_b / k_f ratio does not affect the local and average Nusselt numbers at $\Phi = 75°$. Therefore, the blind slat's thermal conductivity becomes less significant as the effective blind width is decreased or if the k_b / k_f ratio is small. This is evident in Figures 4.19 to 4.21, where the smaller W_b / W_c ratio curves yield a lower Nusselt number. Also, the lower k_b / k_f ratio curves yield a Nusselt number near one, regardless of the effective blind width, for Rayleigh numbers in the conduction regime.

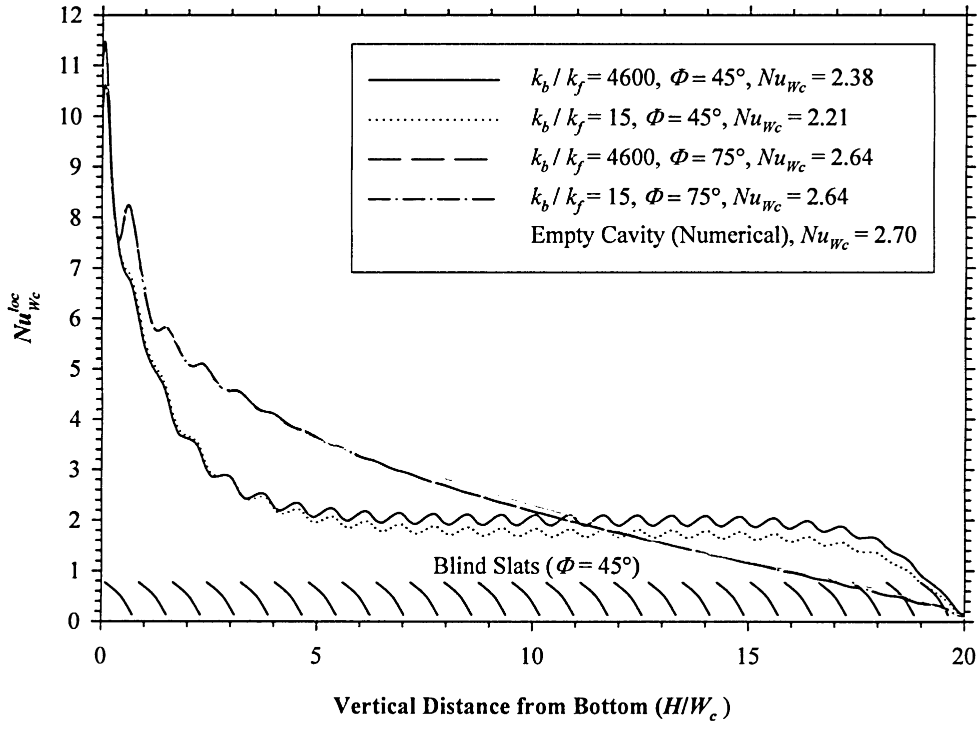

Figure 4.31: Effect of blind thermal conductivity on hot-wall local Nusselt number distribution for slat angles of 45° and 75° ($Ra_{Wc} = 10^5$, $A = 20$, $W_b / W_c = 0.9$, $k_b / k_f = 15$ and 4600, $\Phi = 45°$ and 75°)

In Figure 4.28 and 4.31, the local Nusselt number for an empty cavity has been plotted using data from a CFD solution, at a Rayleigh number of 10^5. The average Nusselt number from the CFD solution is 2.70 and the average from ElSherbiny et al. [11] and Wright's [12] correlation is 3.07. The Nusselt number from the CFD solution is clearly under-predicted. This is likely due to unsteady flow, because the critical Grashof number for the empty cavity is well exceeded, as suggested by Equation 1.7. It is assumed that the trend of the local Nusselt number curve is not heavily affected. In Tables 4.1 and 4.2, the dimensionless empty cavity stream function for a Rayleigh number of 10^5 could also be under-predicted. Even though some error is involved in these values, they are used to get an approximate idea of the effect a blind has on the thermal and hydrodynamic aspects of an empty cavity.

4.2.6 Aspect Ratio Effect

Figures 4.32 to 4.34 illustrate the effect of the cavity aspect ratio on the Nusselt number for W_b / W_c ratios from 0.5 to 0.9 and slat angles of 0°, 45°, and 75°. Rayleigh numbers in the conduction regime ($Ra_{Wc} = 10 - 1000$) and convection dominated regime ($Ra_{Wc} = 1 \times 10^5$) have been considered.

In Figure 4.32 ($\Phi = 0°$), for a Rayleigh number in the convection dominated regime, Nusselt number increases and becomes less dependent on aspect ratio as the W_b / W_c ratio approaches unity. The increase in the W_b / W_c ratio conduces to the stacking effect; thus, a strong periodic characteristic develops, as exemplified in the isotherms of Figure 4.22. Stacking similar array of cavities, with an aspect ratio of about one, would not change the heat flux or the Nusselt number. Generally, periodicity tends to keep the average of the measured quantity constant (in this case the Nusselt number), regardless of the domain (in this case the aspect ratio). For Rayleigh numbers in the conduction regime, the Nusselt number also increases as the W_b / W_c ratio increases, but is independent (IND) of aspect ratio.

In Figure 4.32 ($\Phi = 0°$), the horizontal line ($Nu_{Wc} = 3.07$) indicates the empty cavity Nusselt number for a Rayleigh number of 10^5. This Nusselt number is valid for any aspect ratio greater than 10. It is apparent that for a W_b / W_c ratio just above 0.8, the heat transfer rate exceeds that of an empty cavity.

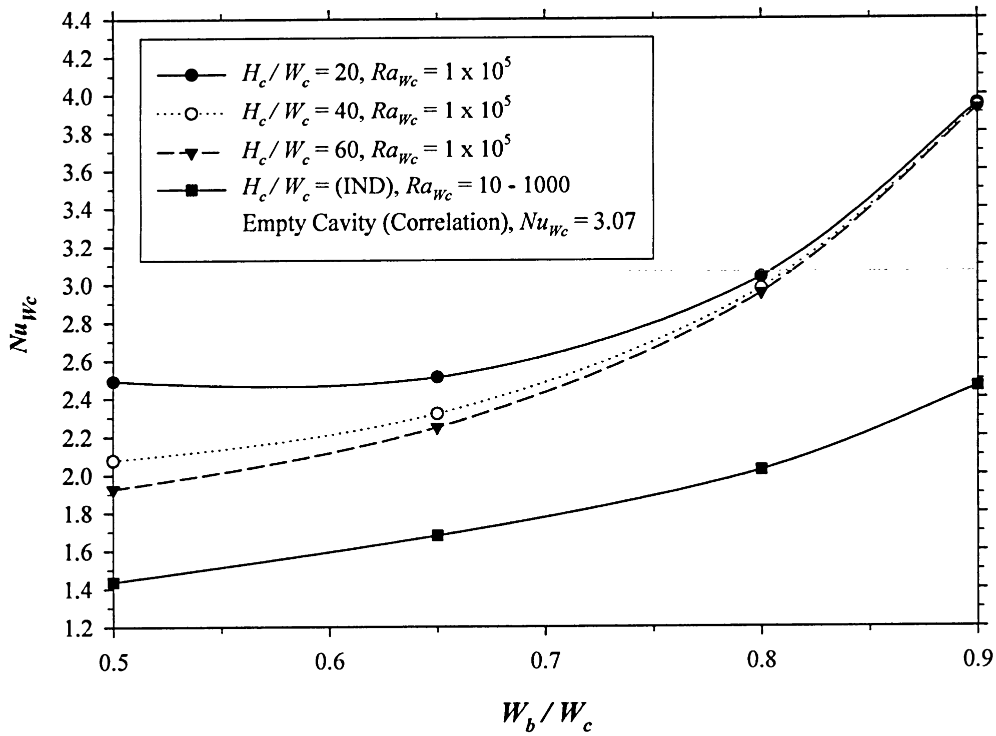

Figure 4.32: Effect of aspect ratio on average Nusselt number for a slat angle of 0° (Ra_{Wc} = 10 to1000 and 10^5, A = 20, 40, and 60, W_b / W_c = 0.5 to 0.9, k_b / k_f = 4600, $\Phi = 0°$)

In Figure 4.33 ($\Phi = 45°$), the Nusselt number is a function of the aspect ratio for all W_b / W_c ratios, at a Rayleigh number of 10^5. At a Rayleigh number in the conduction regime, the Nusselt number increases as the W_b / W_c ratio approaches unity, but is again independent of the aspect ratio.

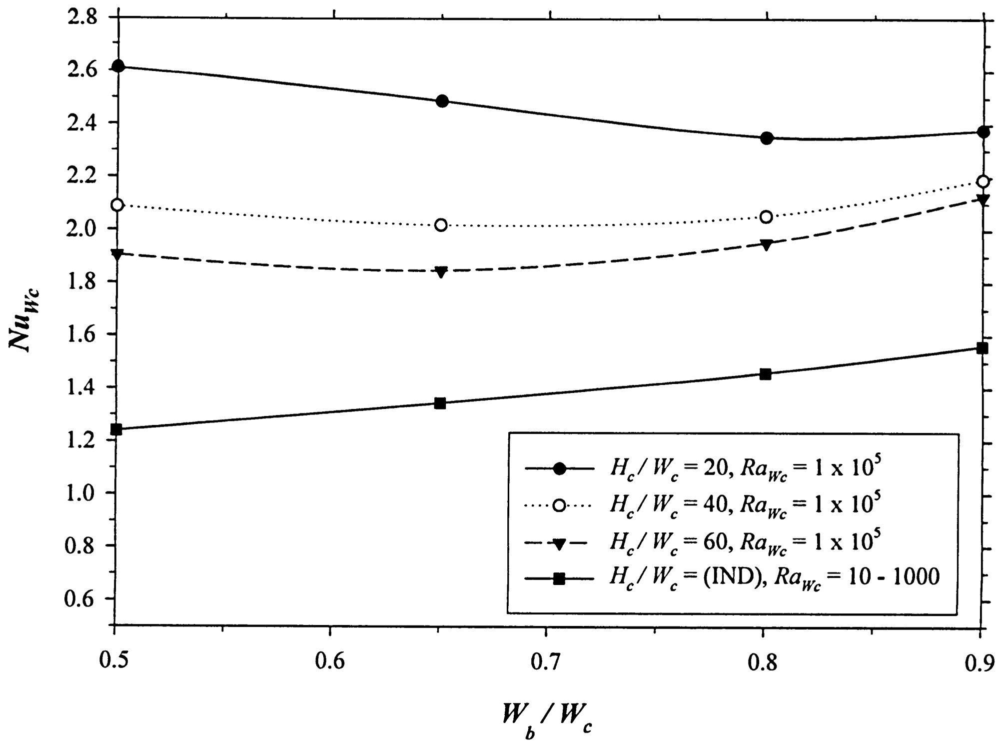

Figure 4.33: Effect of aspect ratio on average Nusselt number for a slat angle of 45° (Ra_{Wc} = 10 to1000 and 10^5, A = 20, 40, and 60, W_b / W_c = 0.5 to 0.9, k_b / k_f = 4600, Φ = 45°)

In Figure 4.34 (Φ = 75°), the Nusselt number is a function of the aspect ratio for all W_b / W_c ratios, at a Rayleigh number of 10^5. For a Rayleigh number in the conduction regime, the Nusselt number increases slightly as the W_b / W_c ratio approaches unity, but is again independent of the aspect ratio. Overall, the Nusselt number has a weak dependence on the W_b / W_c ratio, at a slat angle of 75°.

In Figures 4.32 to 4.34, it is evident that Nusselt number always increases as the aspect ratio is decreased. Over the range studied, the aspect ratio has the greatest effect (35.4%) when the W_b / W_c ratio is equal to 0.9 and the slat angle is equal to 75°, and the least effect (0.54%) when the W_b / W_c ratio is equal to 0.9 and slat angle is equal to 0°, both at a Rayleigh number of 10^5. This is illustrated in Figure 4.35. As the Rayleigh number increases, the effect of the aspect ratio becomes more influential on the average Nusselt number, especially for high slat angles.

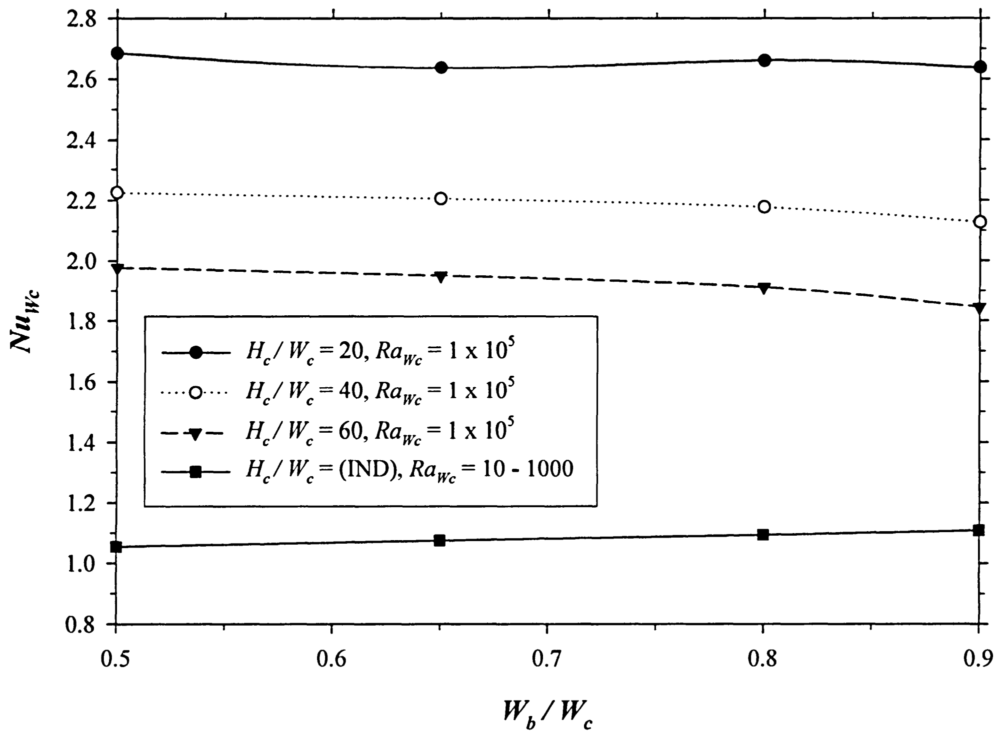

Figure 4.34: Effect of aspect ratio on average Nusselt number for a slat angle of 75° (Ra_{Wc} = 10 to1000 and 10^5, A = 20, 40, and 60, W_b / W_c = 0.5 to 0.9, k_b / k_f = 4600, Φ = 75°)

As mentioned in Chapter 1, the study of ElSherbiny et al. [11] suggests that, for an empty cavity, Nusselt number increases and becomes increasingly dependent on the aspect ratio, as the aspect ratio is decreased. Also, when a buoyancy-driven flow in an empty cavity is observed, it is apparent that the two adjacent boundary layers interact as they develop along the vertical walls (see Figures 1.3 to 1.5). This interaction forms a periodic characteristic apparent in the thermal contours, making the Nusselt number quite independent of the cavity aspect ratio (approximately for A > 25). When the slat angle is near Φ = 75°, the Nusselt number is a function of the aspect ratio, because no periodic characteristics are apparent in the temperature field and the flow is dominantly parallel to the glazing or in the y direction (limited flow cross-over, see Figures 4.26 or 4.27). As previously mentioned, the amount of flow in the x direction is more influential on the heat transfer rate than the amount of flow in the y direction. This is the main reason why the Nusselt number decreases as the aspect ratio increases (see Figure 4.34).

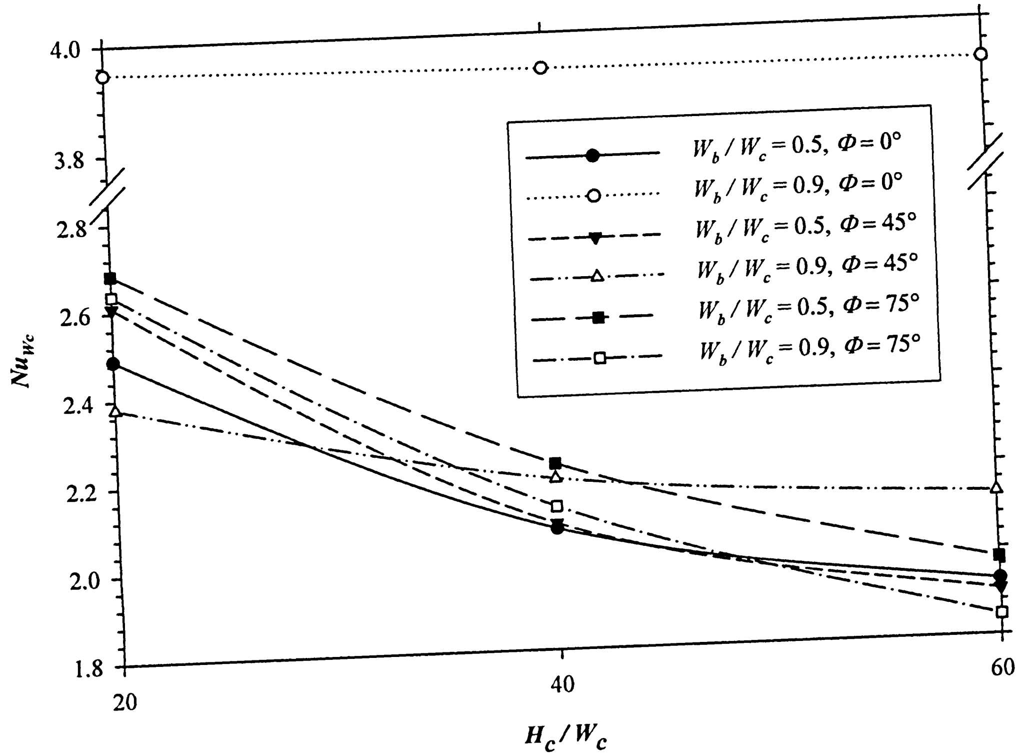

Figure 4.35: Effect of average Nusselt number dependence on aspect ratio ($Ra_{Wc} = 10^5$, $A = 20$, 40, and 60, $W_b / W_c = 0.5$ and 0.9, $k_b / k_f = 4600$, $\Phi = 0°$, 45°, and 75°)

4.2.7 Positive and Negative Slat Angle Effect

Figure 4.36 illustrates the effect of positive and negative slat angles on the Nusselt number. Only slat angles of ± 45° were considered, because it is assumed that these angles would yield the greatest Nusselt number difference. Except for a W_b / W_c ratio equal to 0.5, only at a Rayleigh number of 10^5, it seems that there is an insignificant difference (< 1%) in the Nusselt number between positive and negative slat angles of 45°. This conclusion does not agree with experimental studies. Huang's [35] and Garnet's [32] GHP apparatus experimental results showed a higher percent difference, up to 7%, in the U-value for the positive slate angle (cold-side-up), at Rayleigh numbers in the low convection dominated regime.

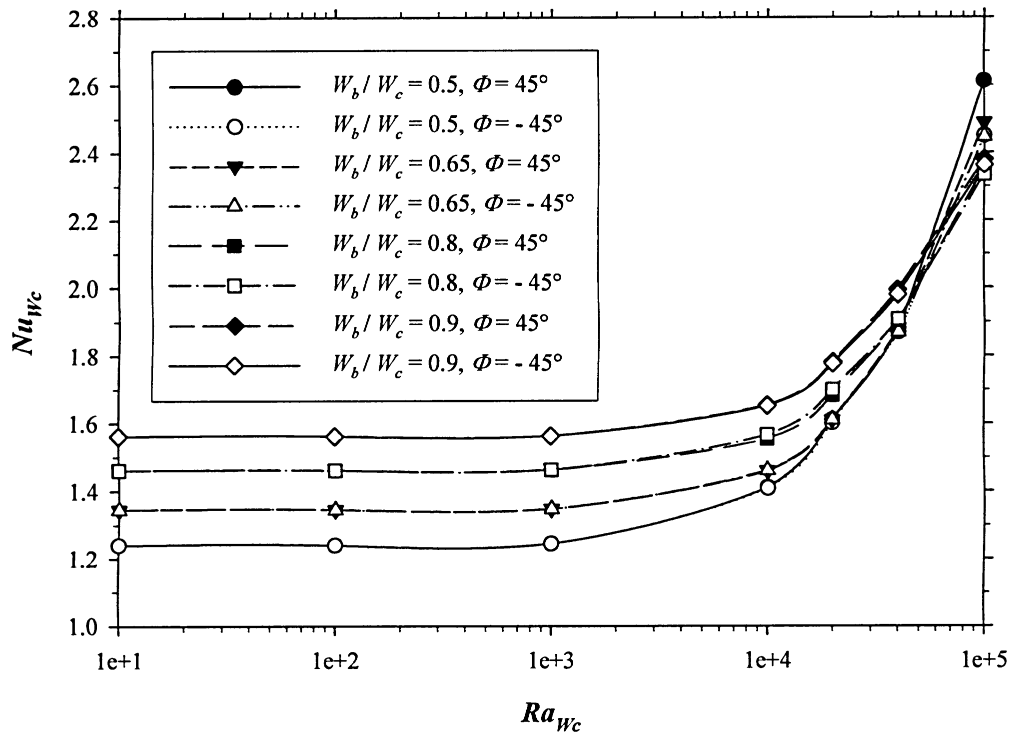

Figure 4.36: Effect of positive and negative slat angles on local Nusselt number ($Ra_{Wc} = 10^5$, $A = 20$, $W_b / W_c =$ 0.5 to 0.9, $k_b / k_f = 4600$, $\Phi = \pm 45°$)

Recalling Figure 3.9, Lai's [10] MZI experimental local Nusselt number data were plotted against results from a numerical solution for a slat angle of 45°. The two sets of results do not show a close agreement. The experimental curve has variations in the local convective heat transfer that were not predicted numerically, even though the average Nusselt numbers are within 10%. The interferogram in Figure 3.10 shows a stronger cross-over effect, indicating a stronger recirculating flow between the blind slats, when compared to the numerically obtained temperature contours. The preliminary numerical study by Lai [10] and Lai et al. [43]

predicted the same. This could indicate that the flow is slightly unsteady and that a CFD model (under the steady assumption) does not simulate the cross-over effect and/or the strong primary and secondary flow interaction very well. Intuitively, the positive slat angle (cold-side-up) is more conducive to the cross-over effect, yielding a higher heat transfer rate. Furthermore, at a positive slat angle of 45° and Rayleigh number of 10^5, the CFD simulations in the present study usually yielded a *wave-like* (oscillatory) solution and had difficulty converging. This is likely due to the complex flow physics (e.g. vortex shedding) in the cross-over effect, where high density gradients are probable in the secondary recirculating flow. These specific details are beyond the scope of the present study and are unclear at this time. However, only the average Nusselt number is of importance, and the error involved in regards to this issue is minor (see Section 3.9).

4.3 Empty Cavity Comparison

As mentioned, in most of the graphs in this chapter, an average Nusselt number curve for an empty cavity has been plotted using the average of the correlation by ElSherbiny et al. [11] and Wright [12] (Equations 1.10 and 1.11). It is apparent that, in all cases, for low Rayleigh numbers, the blind increases the convective heat transfer rate due the thermal bridging effect. Therefore, the empty cavity gives a better thermal performance at low Rayleigh numbers. For high Rayleigh numbers, only for the cases that have the stacking effect, the blind increases the convective heat transfer beyond that of an empty cavity. For all other cases, the blind helps reduce the convective heat transfer.

4.4 Summary

The parametric study shows that the effective blind width to cavity width ratio has a strong influence on the three main factors (outlined in Section 4.2) that affect the convective heat transfer. Also, the study shows that the convective heat transfer rate can be significantly reduced if the boundary layer interaction is inhibited. This is achieved when the blind is in the closed position ($\Phi = 75°$). Inherently, at this slat angle, the conductive effect of the blind is also diminished. When the cavity aspect ratio is increased, the Nusselt number is further reduced. The purpose of this study is not to find an optimum window/blind configuration, where the convective heat transfer is at a minimum. However, it is worth mentioning that, for a fixed cavity width (W_c), the average Nusselt number increases monotonically as the W_b / W_c ratio is increased. In the window designer's point of view, there is no intermediate optimum for the W_b / W_c ratio for the range of parameters studied. A more detailed list of conclusions is given in Chapter 6.

5

SIMPLIFIED MODEL

5.1 Introduction

The convective and radiative heat transfer of a window/blind system is coupled such that a conjugate solution, including both modes, is necessary in order to predict the U-value. The magnitude of the radiative heat transfer rate is about 80% greater than the convective heat transfer rate for non-treated glazing surfaces. This conjugate problem contains several radiative parameters which make a general solution for the average Nusselt number very difficult. The Simplified Model is used to overcome this issue, where the convective and radiative heat transfer rates are solved separately by using a numerical convection-only model and a theoretical radiation model, respectively. Both models are later recoupled using a post-processing algorithm to obtain a conjugate heat transfer rate comparable to a full CFD solution. Therefore, the convection-only solution does not depend on and can apply to any arbitrary surface emissivities and absolute surface temperatures. The convection-only CFD solutions require far less computational overhead, as no view factor calculations and radiative iterations are necessary. The S2S radiation model in FLUENT is computationally very expensive when there are a large number of radiating surfaces. In this chapter, the details of the Simplified Model are outlined. Further details regarding the Simplified Model can be found in [34].

5.2 Radiation Model

As illustrated in Figure 5.1, an imaginary four-surface enclosure was developed using two adjacent slats. The slats are approximated as having no curvature and long in the z direction, such that the geometry can be treated as two-dimensional. The error introduced by the flat slat simplification has been studied by Yahoda and Wright [33]. They determined that an error of approximately 0.01 can be expected in the effective absorptance value for the slat surface at a slat radius of curvature, r_s, to pitch ratio of about 2. This is approximately the same ratio for the model considered in this study ($r_s \approx 1.95$). It can easily be shown that the slat tip-to-glazing spacings, s_h and s_c, have a negligible effect on the view factors; therefore, a four surface model is sufficient. Naylor et al. [29] and Yahoda and Wright [33] have done studies with more than four surfaces and found that the heat transfer rate difference is small.

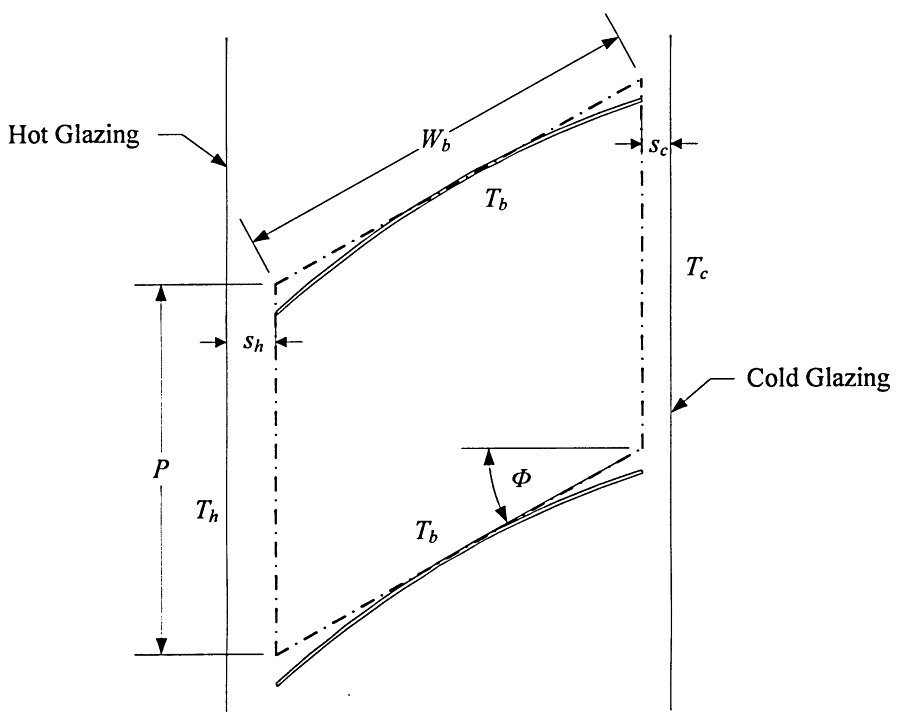

Figure 5.1: Four-surface enclosure approximation

The radiation formulation is based on a grey enclosure analysis (independent of λ), where the surfaces are assumed to be isothermal, emit and reflect diffusely (independent of direction), uniformly irradiated, and have a constant emissivity. The isothermal assumption for the blind slats is reasonable because the thermal internal resistance over the surface film resistance is very small (i.e. $Bi_b << 1$). The grey assumption allows for Kirchoff's law to be applied for all surfaces (i.e. $\rho + \varepsilon = 1$ or $\alpha = \varepsilon$), where all walls of the enclosure are opaque (i.e. $\tau = 0$). Glass is transparent in the visible electromagnetic spectrum, but it is opaque to long-wave (infrared, $\lambda > 3$ μm) radiation. Only nighttime conditions are considered; therefore, no solar radiation is involved. As a result, the radiation exchange in this study falls entirely in the long-wave portion of the electromagnetic spectrum. Long-wave radiation is emitted typically from surfaces that are near room temperature. Participating medium effects are not considered in this radiative analysis. The fill-gas is assumed transparent to radiative heat exchange, particularly for the small distances of a typical window cavity. The above assumptions for the radiation model correspond to the S2S radiation model in FLUENT.

Figure 5.2 shows the local hot-wall radiative heat flux results from the full CFD solution that has parameters that correspond to Lai's [10] MZI apparatus experiment (used for validation in Section 3.9). It is apparent that the radiative heat transfer rate is strongly periodic even though the cavity aspect ratio for this case is small (A = 13.3). Therefore, due to the predominant periodic nature of the radiative heat flux, the array of slats can be approximated as being infinitely long.

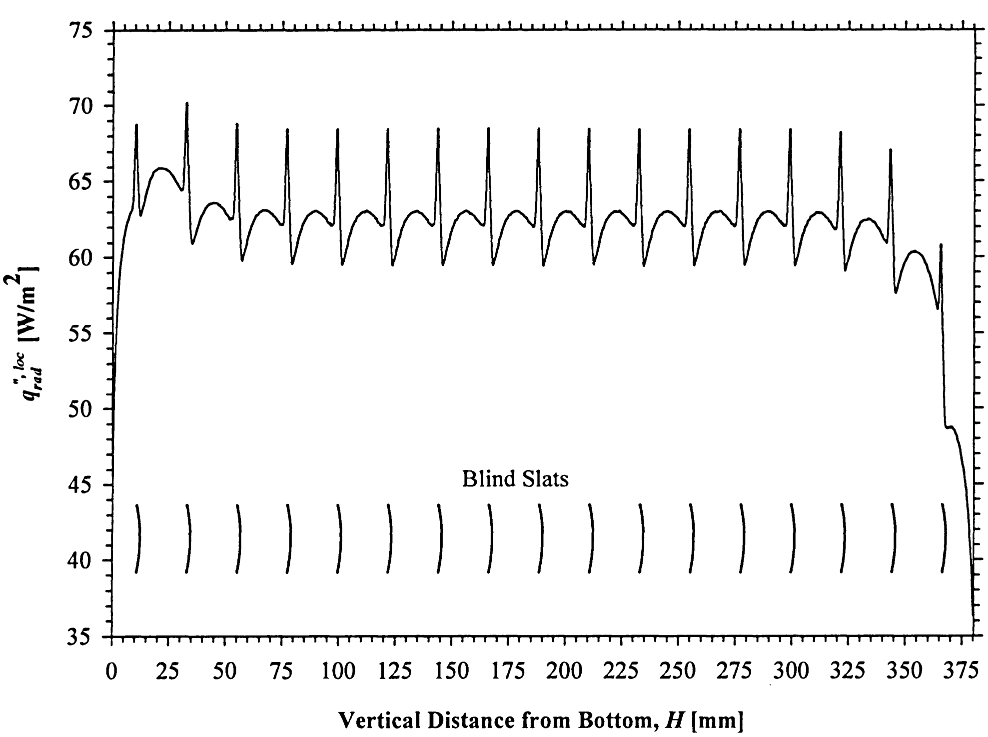

Figure 5.2: Local radiative heat flux on hot-wall from a full CFD solution ($Ra_{Wc} = 4.56 \times 10^4$, $A = 13.3$, $W_b / W_c = 0.86$, $k_b / k_f = 4617$, $\Phi = 0°$)

5.2.1 Radiation Formulation

Considering the assumptions from the previous section, the four-surface enclosure approximation in Figure 5.1 corresponds to the radiation model in Figure 5.3, where J_k is the radiosity, G_k is the irradiation, ε_k the hemispheric emissivity, and T_k the temperature of the k^{th} surface. The circled numbers show the surface designations for the radiation model.

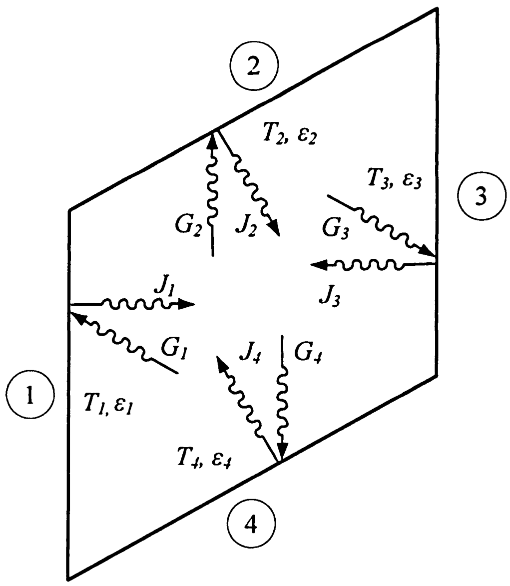

Figure 5.3: Four-surface radiation model

The boundary conditions for the radiation model in Figure 5.3 are as follows:

Surface 1

$$T_1 = T_h, \quad \varepsilon_1 = \varepsilon_g \tag{5.1 a}$$

Surface 2

$$T_2 = T_b, \quad \varepsilon_2 = \varepsilon_b \tag{5.1 b}$$

Surface 3

$$T_3 = T_c, \quad \varepsilon_3 = \varepsilon_g \tag{5.1 c}$$

Surface 4

$$T_4 = T_b, \quad \varepsilon_4 = \varepsilon_b \tag{5.1 d}$$

where T_b is the temperature of the blind (initially unknown), ε_b is the hemispheric emissivity of the blind, and ε_g is the hemispheric emissivity of the glazing. As mentioned, the slat tip-to-glazing spacing, s_h and s_c, has a negligible effect on the radiative heat transfer; therefore, surface 1 and 3 are assigned the temperature of the hot and cold glazings, respectively.

Equations 5.2 to 5.4 were used to solve the radiative heat transfer rates for the four surfaces in the radiation model in Figure 5.3. The net radiative heat transfer rate, q_k, from the k^{th} surface is determined by the difference between the radiosity, J_k, and the irradiation, G_k:

$$\frac{q_k}{A_k} = J_k - G_k \tag{5.2}$$

The radiosity is the portion of the radiation emitted and reflected from the k^{th} surface and the irradiation is the incoming radiation from all other surfaces on to the k^{th} surface. Where irradiation is defined by:

$$G_k = \sum_{j=1}^{N} J_j F_{k-j} \tag{5.3}$$

and radiosity is defined by:

$$J_k = \varepsilon_k E_k + \rho_k G_k = \varepsilon_k \sigma T_k^4 + \rho_k \sum_{j=1}^{N} J_j F_{k-j} \tag{5.4}$$

where E_k is the emissive power, and ρ_k is the reflectivity of the k^{th} surface, $F_{k\text{-}j}$ is the view factor of surface k to j, σ is the Stefan-Boltzmann constant, and N is the number of surfaces within the enclosure (e.g. $N = 4$).

Equation 5.4 represents a set of simultaneous equations for the surface radiosities. Therefore, four equations and four unknowns are required to be solved. The Bevans-Dunkle [45] iterative technique was used to simultaneously solve all four surface radiosities. This technique incorporates a Gauss-Seidel method, is easy to program, and converges efficiently. A program was developed to solve the radiative heat transfer rate using the Bevans-Dunkle technique (see Appendix E). The following convergence criterion was followed:

$$\frac{J_k^{i-1} - J_k^i}{J_k^i} < 10^{-6} \tag{5.5}$$

Finally, the radiative heat transfer rate was calculated using Equation 5.6.

$$\frac{q_k}{A_k} = \varepsilon_k \sigma T_k^4 - \alpha_k \sum_{j=1}^{N} J_j F_{k-j} \tag{5.6}$$

The criterion in Equation 5.5 should yield a net energy balance for the system as follows:

$$\sum_{k=1}^{N} q_k < 10^{-4} \tag{5.7}$$

5.2.2 View Factor Formulation

The view factors have a great influence on the radiation exchange between the diffuse surfaces in Figure 5.3. Since the enclosure is modeled as two-dimensional, for each radiating surface the view factors, F, were calculated using Hottel's Crossed String method [46]. This method considers the size, separation distance, and orientation of all surfaces. It is expressed as follows:

$$F_{k-j} = \frac{\sum XS_{k-j} - \sum US_{k-j}}{2L_k} \tag{5.8}$$

where $\Sigma XS_{k\text{-}j}$ is the sum of the crossed string lengths joining the k^{th} and j^{th} surfaces, $\Sigma US_{k\text{-}j}$ is the sum of the uncrossed string lengths joining the k^{th} and j^{th} surfaces, and L_k is the length of the k^{th} surface. For accurate radiosity values, the reciprocity relationship and the conservation of view factors, Equations 5.9 and 5.10, respectively, were satisfied.

Reciprocity relationship:

$$A_k F_{k-j} = A_j F_{j-k} \tag{5.9}$$

Conservation:

$$\sum F_{k-j} = 1 \tag{5.10}$$

Because all surfaces in the enclosure are flat, the self-viewing factors, $F_{k\text{-}k}$, are equal to zero. The Cross String method was chosen because it provides a closed-form solution, is very simple to calculate, and requires no computationally expensive integrations. Figure 5.4 illustrates the configuration of the *strings* from surface k to j, and Equation 5.11 expresses the resulting view factor.

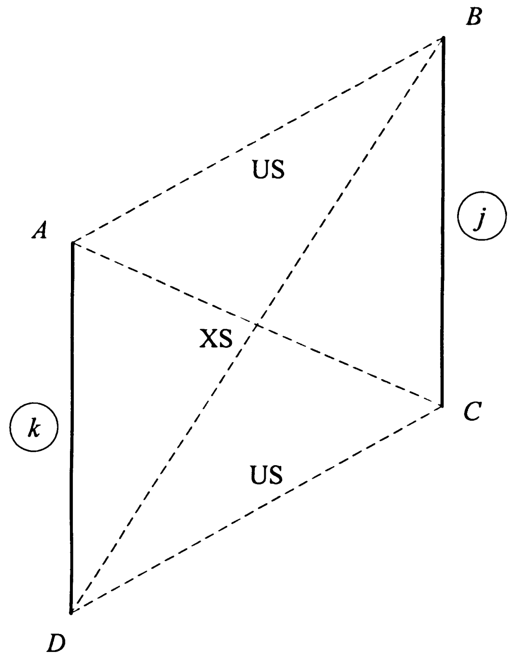

Figure 5.4: Configuration of Crossed String method for surface k to j

$$F_{k-j} = \frac{(\overline{AC} + \overline{BD}) - (\overline{AB} + \overline{CD})}{2(\overline{AD})} \tag{5.11}$$

Therefore, view factors depend entirely on the enclosure geometry: slat width (W_b), slat pitch (P), and slat angle (Φ). Because the pitch is proportional to the slat width ($P = 7/8\ W_b$), the slat angle has the only influence on the view factor for each of the four surfaces. A program was developed to solve the view factors (see Appendix D).

5.3 Energy Balance

The blind temperature, T_b, in Equation 5.1 is dependent on the coupled convective and radiative heat transfer, where the blind can be thought of as the *coupling medium.* Because a convection-only CFD solution was done, the (correct) temperature of the blind was initially unknown. This temperature is required in order to solve for the surface radiosities. Equation 5.12 was used to estimate (est) a *first guess* for the iteration.

$$T_b^{est} = \frac{T_h + T_c}{2} \tag{5.12}$$

The blind's temperature was determined by an energy balance analysis which involves both convective and radiative influences. Figure 5.5 shows the energy balance diagram of the blind that results in Equation 5.13.

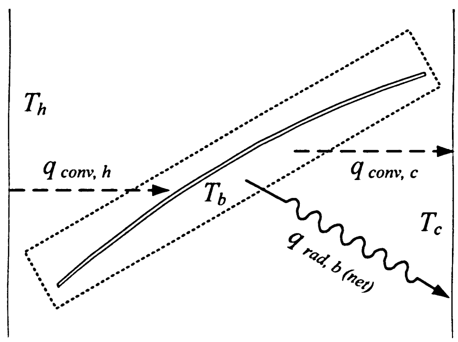

Figure 5.5: Energy balance of blind slat

$$q_{rad,b\,(net)} = h_{h-b}H_c\left(T_h - T_b\right) - h_{b-c}H_c\left(T_b - T_c\right) \tag{5.13}$$

Where $q_{rad,\, b\ (net)}$ of the slat is obtained from the sum of the heat transfer rates from surface 2 and 4 of the radiation model in Figure 5.3:

$$q_{rad,b\ (net)} = \left(q_2 + q_4\right)\frac{H_c}{P} \tag{5.14}$$

and $h_{h\text{-}b}$ and $h_{b\text{-}c}$ are the convective heat transfer coefficients for the hot glazing to the blind and for the blind to the cold glazing, respectively. These coefficients are calculated using Equations 5.15 and 5.16. The coefficients are based on a centre-glass one-dimensional thermal circuit model as illustrated in Figure 5.6, where q_{conv} is the overall convective heat transfer rate across the enclosure, obtained from a convection-only CFD solution. Using Equation 5.15, the average heat transfer coefficient of the window/blind system can be calculated.

The term H_c / P in Equation 5.14, and later in Equation 5.20, determines the number of stacked four-surface enclosures in the full window/blind system. This inherently makes the assumption that the radiative heat transfer rate is periodic for the entire glazing height.

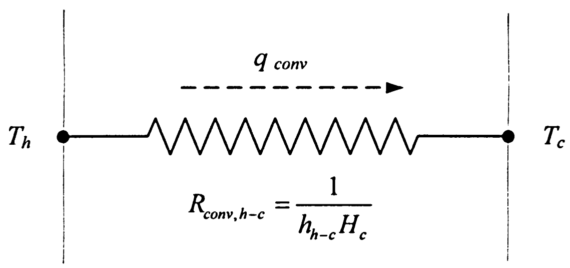

Figure 5.6: One-dimensional thermal circuit across glazings

$$h_{h-c} = \frac{q_{conv}}{H_c\left(T_h - T_c\right)} \tag{5.15}$$

The thermal circuit in Figure 5.6 can be broken down to an equivalent circuit, shown in Figure 5.7, which includes the temperature of the blind. This figure is the thermal circuit equivalent to the Figure 5.5.

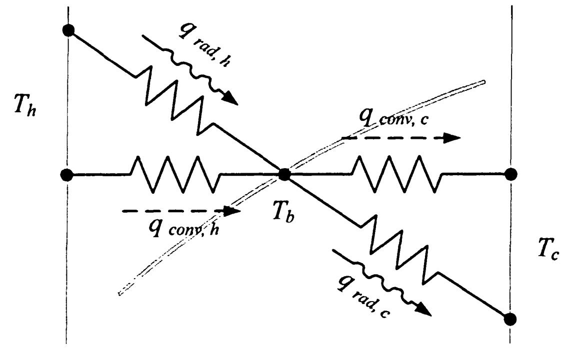

Figure 5.7: Modified one-dimensional thermal circuit across glazings

It is likely that the heat transfer coefficient from the hot-glazing to the blind and from the blind to the cold-glazing is roughly equivalent. This is a good approximation because the dynamics of the flow on either side of the blind should be very similar, especially when the blind is placed directly in the centre of the glazings. Figures 3.8 and 3.10 from Chapter 3 show this in the stream function contours obtained from a full CFD solution.

Due to the curvature of the slat, at angles larger than 0°, s_h and s_c are not equal. In Figure 5.1, it is evident that s_h is greater than s_c. This is assumed not to influence the convective heat transfer rate significantly. Therefore, for a centred blind, the total convective resistance across the glazings can be divided such that:

$$h_{h-c} = \frac{1}{2} h_{h-b} = \frac{1}{2} h_{b-c} \tag{5.16}$$

It is assumed that radiation will have a negligible affect on $h_{h\text{-}b}$ and $h_{b\text{-}c}$. Because s_h is shorter than s_c, the slat temperature could shift closer toward the cold glazing due to the thermal conductivity of the slat. This would affect the equality between $h_{h\text{-}b}$ and $h_{b\text{-}c}$, but only for slat angles near 45°. For slat angles of 0°, s_h is equal to s_c, and for slat angles near 75°, the effect of thermal conductivity will be very weak because s_h and s_c is large. Again, Figures 3.8 and 3.10 from Chapter 3 show the temperature contours from a full CFD solution. By inspection of the isotherms, it is apparent that the temperature of the blind falls about half way between the hot and cold wall temperatures. Generally, this is true for a slat found in the centre-glass region, half way up a cavity. Especially for a case with a small effective blind width, and a high Rayleigh number, the slats in the top portion of the cavity will have temperatures slightly closer to the hot glazing and the bottom portion of the cavity will have temperatures slightly closer to the cold glazing. In Figure 3.10, this is apparent near the top and bottom ends of the enclosure. It is assumed that the slat temperature half way up the cavity can represent the average temperature of the entire blind (linear approximation). The validity of Equation 5.16 is supported by the close agreement of the Simplified Model to the corresponding full conjugate solution, covered in Section 5.4. Finally, by substituting Equation 5.16 into Equation 5.13 (the energy balance equation) and solving for T_b yields an improved or corrected blind temperature:

$$T_b = \frac{1}{2}\left(\left(T_h + T_c\right) - \frac{q_{rad,b\,(net)}}{h_{h-b} H_c} \right) \tag{5.17}$$

The following convergence criterion was followed:

$$\frac{T^{*i-1} - T^{*i}}{T^{*i}} < 0.01 \tag{5.18}$$

where T^*, the dimensionless temperature, is defined in Equation 2.2 in Chapter 2. This improved blind temperature is substituted into the radiosity equation (Equation 5.4) to get an improved $q_{rad,\,b}$ and also substituted into Equation 5.19 to get a corrected convective heat transfer rate, $q_{conv,h}^{corr}$ and $q_{conv,c}^{corr}$. The term *corrected* refers to the effect of the recoupling, where by using the Simplified Model, these values are converged towards that of a full CFD solution.

$$q_{conv,h}^{corr} = 2h_{h-b}H_c\left(T_h - T_b\right) \tag{5.19 a}$$

$$q_{conv,c}^{corr} = 2h_{b-c}H_c\left(T_b - T_c\right) \tag{5.19 b}$$

Using the heat transfer rate from the radiation model, $q_{rad,h}$ (surface 1) and $q_{rad,c}$ (surface 3) can be calculated using Equation 5.20.

$$q_{rad,h} = q_1 \frac{H_c}{P} \tag{5.20 a}$$

$$q_{rad,c} = q_3 \frac{H_c}{P} \tag{5.20 b}$$

When the temperature of the blind is converged, Equations 5.19 and 5.20 can be substituted into Equation 5.21 to solve for the Simplified Model total heat transfer rate, q_{total}^{sm}, for the window/blind system. The convection and radiation are now re-coupled.

$$q_{total}^{sm} = q_{conv,h}^{corr} + q_{rad,h} = q_{conv,c}^{corr} + q_{rad,c} \tag{5.21}$$

Using Equation 2.8 from Chapter 2, the Simplified Model U-value (U^{SM}) for the window/blind system can be calculated as follows:

$$U^{SM} = \frac{q_{total}^{SM}}{H_c \left(T_h - T_c\right)} \tag{5.22}$$

Figure 5.8 shows a diagram of the iteration steps in solving the temperature of the blind.

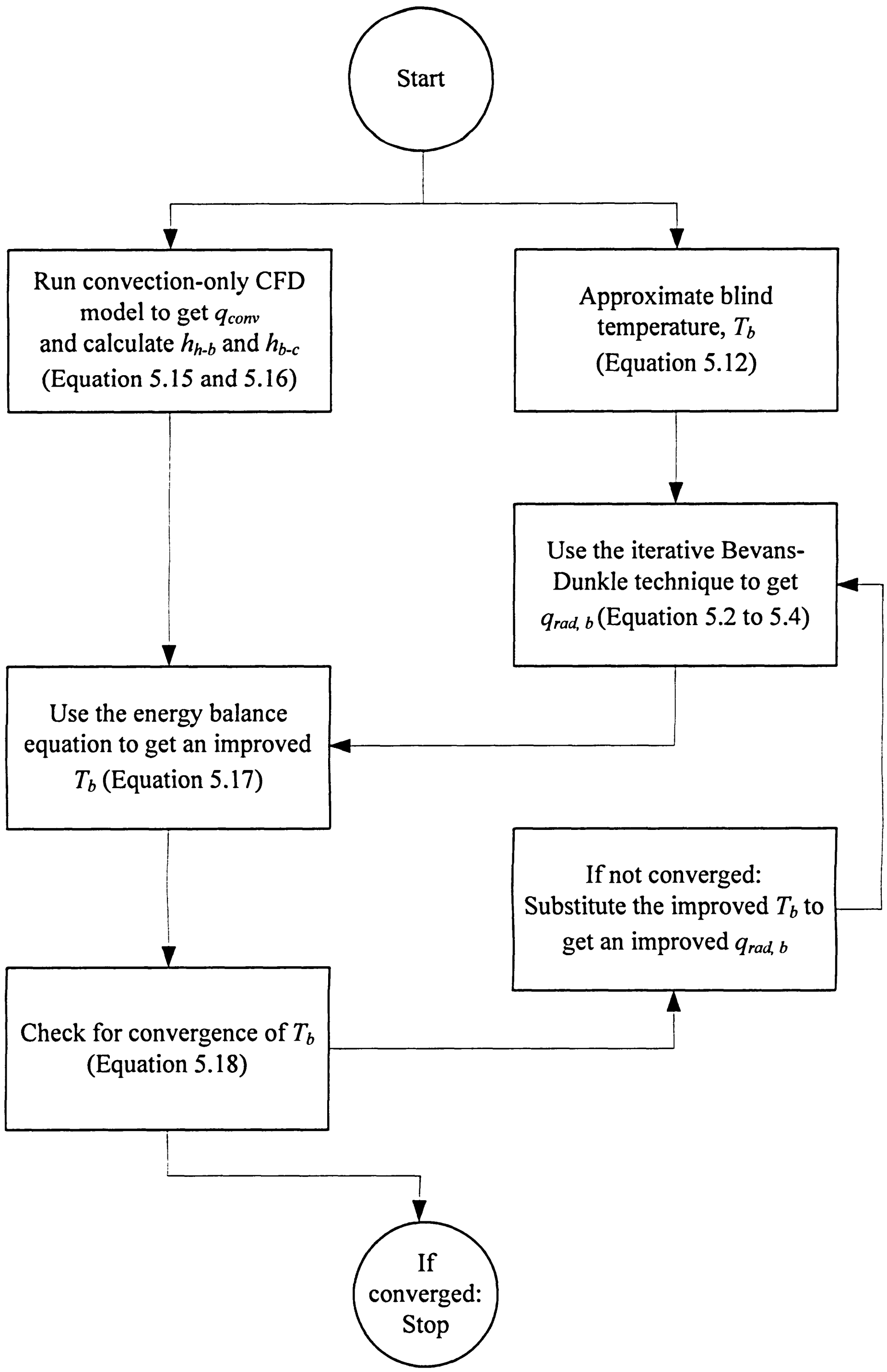

Figure 5.8: Iteration steps to solve for blind temperature

5.4 Validation

Table 5.1 contains the U-values from the full CFD solution (used for validation in Section 3.9) that have parameters corresponding to Huang's [35] GHP apparatus experiment. Figure 5.9 is a plot of the U-values from Table 5.1. Slat angles of 0° to 75° have been considered to validate the Simplified Model approximation, especially at high slat angles.

Table 5.1: U-value comparison between a Simplified Model and a full CFD solution (Ra_{Wc} = 1.39 x 10^4, A = 23.8, W_b / W_c = 0.58, k_b / k_f = 4615, Φ = 0°, 30°, 60°, and 75°, T_h = 302.59 K, T_c = 293.41 K, ε_g = 0.84, ε_b = 0.792, ε_{ew} = 0.84)

Angle, Φ [Degrees]	Simplified Model U-value [W/m²K]	Full Solution U-value [W/m²K]	% Error
0°	5.00	4.94	1.21%
30°	4.65	4.66	-0.21%
60°	4.00	4.04	-0.99%
75°	3.83	3.74	2.41%

Note: The full CFD solution U-values are the same as the numerical U-values from Table 3.5, but the two glazing resistances (R_g = 0.01045 m²K/W) are not considered.

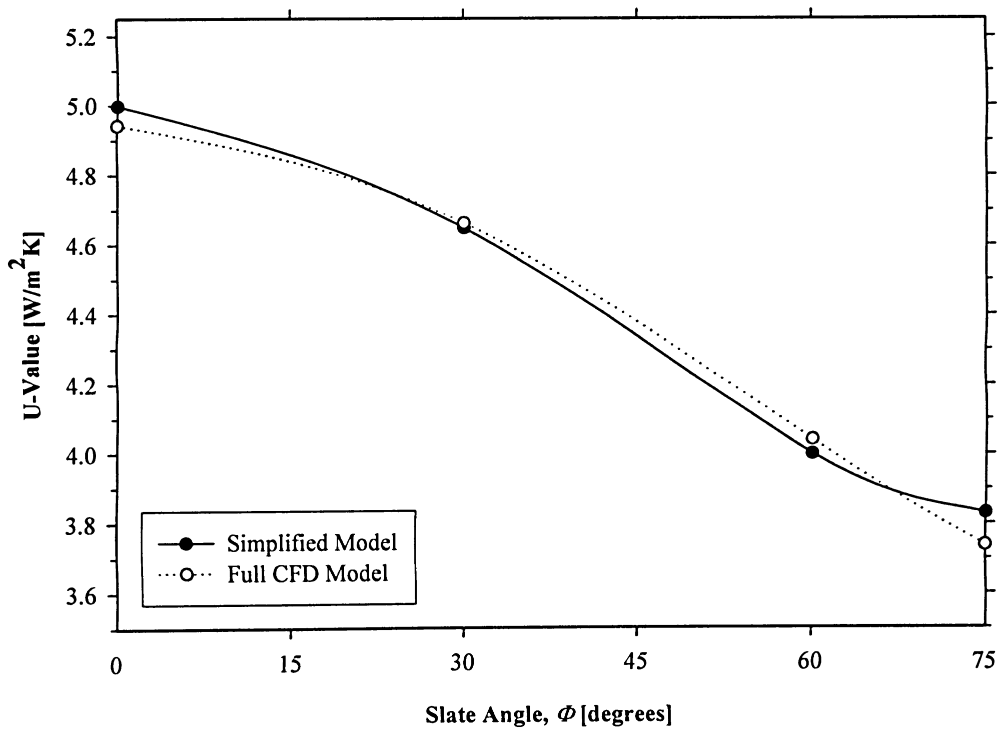

Figure 5.9: U-value comparison between a Simplified Model and a full CFD solution (Ra_{Wc} = 1.39 x 10^4, A = 23.8, W_b / W_c = 0.58, k_b / k_f = 4615, Φ = 0°, 30°, 60°, and 75°, T_h = 302.59 K, T_c = 293.41 K, ε_g = 0.84, ε_b = 0.792, ε_{ew} = 0.84)

It is apparent that the Simplified Model and the full CFD solution agree well, where the highest U-value error is only 2.4%. To further test the Simplified Model, a low-e window was considered, where the hot glazing emissivity was set to 0.171 and the slat angle at 75°. The U-value obtained from the Simplified Model was 2.59 W/m^{2}K and the full solution was 2.48 W/m^{2}K, with an error of 4.17%. Therefore, the Simplified Model is a good approximation, and the assumptions made to reduce the complexity of the radiation model only have a small effect.

Most window/blind systems found on the market have a standard high thermal conductivity aluminium blind ($k_b \approx 120$ W/mK [18]). For this reason, the isothermal assumption of the slats is a good approximation. When a lower conductivity plastic blind is considered ($k_b \approx 0.4$ W/mK), the radiation model in Figure 5.3 may result in an inaccurate radiative heat transfer rate. A single surface (i.e. 2 or 4) might not be sufficient in representing a significant temperature gradient in the slat. The assumption of the surface being uniformly irradiated will no longer hold true. This is of greatest concern in a conduction dominated regime, when the effective blind width to cavity width ratio is near unity.

5.5 Summary

It has been shown that a conjugate convection and radiation problem can be decoupled, such that a convection-only CFD simulation results can be subsequently combined with a simple radiation model to obtain an accurate total heat transfer rate. As mentioned, a general solution for the convective heat transfer is made possible by using the Simplified Model. A correlation can be developed using the current parametric study results and implemented, along with the radiation model, in window modeling software.

6

CONCLUSIONS AND RECOMMENDATIONS

6.1 Conclusions

The free convective heat transfer in a double-glazed window with a between-pane Venetian blind has been studied using a numerical method. A wide set of dimensionless parameters was considered, which allowed for a greater understanding of the thermal interactions between a window and a blind. To include radiation effects, a simplified model was considered and tested for accuracy. Depending on the window/blind geometry, the results from the present study indicate that the blind can either reduce or enhance the convective heat transfer of the system. The main conclusions are as follows:

— The results from the parametric study show that a between-pane blind has a significant influence on the convective heat transfer. It is affected by the following three main factors: The blind's thermal conduction, the impeding effect on the buoyancy-driven flow, and the enhancing or inhibiting effect on the cross-cavity flow. Depending on the window/blind configuration, the magnitude of each of these three factors will be influenced.

— The eff ective blind width to cavity width ratio has the greatest influence on the convective heat transfer. When the effective blind width to cavity width ratio is close to unity, the conduction in the (high conductivity) blind and the cross-cavity flow tends to be very dominant. This configuration yields the highest heat transfer rate, even though the flow is the weakest, because of the impeding effect of the blind.

— When the effe ctive blind width to cavity width ratio is small (e.g. closed blind), the conductive effect of the blind is negligible. The flow for this configuration is the strongest, but generally, the heat transfer rate is the lowest. This is due to the reduction of the cross-cavity flow.

— A high blind to fluid thermal conductivity ratio greatly increases the heat transfer rate at low Rayleigh numbers, when the effective blind width to cavity width ratio is near unity. When the Rayleigh number is increased, the slat's thermal conductivity is not as influential.

— When the effective blind width to cavity width ratio is near unity, the Nusselt number becomes independent of the cavity aspect ratio. However, when the effective blind width to cavity width ratio is small (closed blind), the Nusselt number becomes heavily dependent on the aspect ratio. As the aspect ratio increases, the convective heat transfer rate decreases.

— The numerical solutions indicate that there is an insignificant difference in the convective heat transfer between a positive and negative slat angle of 45°. This conclusion does not agree with experimental studies, although the experimental convective heat transfer difference is small.

- Generally, for low Rayleigh numbers, the blind increases the convective heat transfer rate. At a high Rayleigh number, for cases that have the stacking effect, the blind increases the convective heat transfer beyond that of an empty cavity. For all other cases, the blind helps reduce the convective heat transfer.

- The par ametric study clearly showed that the convective heat transfer rate can be significantly reduced if the boundary layer interaction is inhibited.

- Overall, t he average Nusselt number from the CFD solution showed a close agreement to experimental results.

- The simplified model proved to be accurate in recoupling the convection-only CFD solution with a simple radiation model. When compared to a full CFD solution, the U-values are within 2.4%.

6.2 Recommendations

- I n this study, only nighttime conditions are considered. Because there is no significant overlap between the solar wavelength band (0.2 μm $< \lambda <$ 3 μm) and the longer infrared wavelength band (3 μm $< \lambda <$ 60 μm) of the electromagnetic spectrum, daytime effects can be easily incorporated. Future studies should include solar irradiation, which could be added by generating the appropriate amount of heat within the blind slats.

— In this study, the thermal boundary conditions for the window cavity are idealized, where the glazings are assumed isothermal and the end-walls are assumed adiabatic. These assumptions will affect the heat transfer rate. In future studies, more realistic boundary conditions should be used, thereby considering frame effects, internal and external convective heat transfer coefficients, and conduction in the end-walls.

— To better understand the fluid mechanics within the current window/blind system, a flow visualization study should be conducted to obtain images of the velocity field.

— To resolve the issue of the flow possibly being unstable for slat angles of ±45°, a transient CFD simulation should be conducted. This might reduce the discrepancy between numerical and experimental local and average Nusselt numbers at high Rayleigh numbers.

APPENDIX A – AVERAGE NUSSELT NUMBER FOR $k_b / k_f = 4600$

A.1 Aspect Ratio = 20

Table A.1: Average Nusselt number for dimensionless blind width of 0.5 (Ra_{Wc} = 10 to 10^5, A = 20, W_b / W_c = 0.5, k_b / k_f = 4600, Φ = 0°, ±45°, and 75°)

Ra_{Wc}	Φ = 0°	Φ = 45°	Φ = -45°	Φ = 75°
10	1.437	1.240	1.240	1.054
100	1.437	1.240	1.240	1.054
1000	1.439	1.244	1.244	1.064
10^4	1.547	1.410	1.408	1.340
2 x 10^4	1.687	1.610	1.601	1.644
4 x 10^4	1.932	1.880	1.869	2.056
10^5	2.491	2.611	2.449	2.686

Table A.2: Average Nusselt number for dimensionless blind width of 0.65 (Ra_{Wc} = 10 to 10^5, A = 20, W_b / W_c = 0.65, k_b / k_f = 4600, Φ = 0°, ±45°, and 75°)

Ra_{Wc}	Φ = 0°	Φ = 45°	Φ = -45°	Φ = 75°
10	1.679	1.345	1.345	1.074
100	1.679	1.345	1.345	1.074
1000	1.680	1.347	1.347	1.078
10^4	1.768	1.459	1.461	1.304
2 x 10^4	1.906	1.610	1.610	1.594
4 x 10^4	2.123	1.881	1.869	2.003
10^5	2.511	2.488	2.446	2.637

Table A.3: Average Nusselt number for dimensionless blind width of 0.8 (Ra_{Wc} = 10 to 10^5, A = 20, W_b / W_c = 0.8, k_b / k_f = 4600, Φ = 0°, ±45°, and 75°)

Ra_{Wc}	Φ = 0°	Φ = 45°	Φ = -45°	Φ = 75°
10	2.022	1.461	1.461	1.093
100	2.022	1.461	1.461	1.093
1000	2.023	1.463	1.463	1.102
10^4	2.218	1.554	1.566	1.336
2 x 10^4	2.409	1.682	1.699	1.611
4 x 10^4	2.645	1.904	1.908	2.013
10^5	3.037	2.354	2.334	2.662

Table A.4: Average Nusselt number for dimensionless blind width of 0.9 (Ra_{Wc} = 10 to 10^5, A = 20, W_b / W_c = 0.9, k_b / k_f = 4600, Φ = 0°, ±45°, and 75°)

Ra_{Wc}	Φ = 0°	Φ = 45°	Φ = -45°	Φ = 75°
10	2.460	1.562	1.562	1.108
100	2.460	1.562	1.562	1.108
1000	2.468	1.563	1.563	1.114
10^4	2.795	1.654	1.651	1.328
2×10^4	3.080	1.781	1.777	1.582
4×10^4	3.426	1.993	1.980	1.982
10^5	3.947	2.380	2.362	2.638

A.2 Aspect Ratio = 40

Table A.5: Average Nusselt number for dimensionless blind width of 0.5 (Ra_{Wc} = 10 to 10^5, A = 40, W_b / W_c = 0.5, k_b / k_f = 4600, Φ = 0°, ±45°, and 75°)

Ra_{Wc}	Φ = 0°	Φ = 45°	Φ = -45°	Φ = 75°
10	1.441	1.243	1.243	1.056
100	1.441	1.243	1.243	1.056
1000	1.442	1.245	1.245	1.059
10^4	1.502	1.328	1.329	1.191
2×10^4	1.589	1.429	1.434	1.364
4×10^4	1.740	1.622	1.627	1.669
10^5	2.076	2.088	2.097	2.225

Table A.6: Average Nusselt number for dimensionless blind width of 0.65 (Ra_{Wc} = 10 to 10^5, A = 40, W_b / W_c = 0.65, k_b / k_f = 4600, Φ = 0°, ±45°, and 75°)

Ra_{Wc}	Φ = 0°	Φ = 45°	Φ = -45°	Φ = 75°
10	1.678	1.347	1.347	1.076
100	1.678	1.347	1.347	1.076
1000	1.679	1.348	1.348	1.078
10^4	1.749	1.410	1.421	1.199
2×10^4	1.862	1.497	1.513	1.358
4×10^4	2.037	1.655	1.667	1.647
10^5	2.319	2.020	2.020	2.205

Table A.7: Average Nusselt number for dimensionless blind width of 0.8 (Ra_{Wc} = 10 to 10^5, A = 40, W_b / W_c = 0.8, k_b / k_f = 4600, Φ = 0°, ±45°, and 75°)

Ra_{Wc}	Φ = 0°	Φ = 45°	Φ = -45°	Φ = 75°
10	2.022	1.462	1.463	1.095
100	2.022	1.462	1.463	1.095
1000	2.028	1.465	1.465	1.099
10^4	2.222	1.526	1.541	1.219
2 x 10^4	2.404	1.612	1.639	1.361
4 x 10^4	2.623	1.768	1.789	1.627
10^5	2.976	2.055	2.067	2.177

Table A.8: Average Nusselt number for dimensionless blind width of 0.9 (Ra_{Wc} = 10 to 10^5, A = 40, W_b / W_c = 0.9, k_b / k_f = 4600, Φ = 0°, ±45°, and 75°)

Ra_{Wc}	Φ = 0°	Φ = 45°	Φ = -45°	Φ = 75°
10	2.460	1.564	1.564	1.109
100	2.460	1.564	1.564	1.109
1000	2.469	1.565	1.566	1.113
10^4	2.802	1.639	1.638	1.224
2 x 10^4	3.089	1.738	1.737	1.356
4 x 10^4	3.429	1.904	1.899	1.607
10^5	3.934	2.191	2.191	2.127

A.3 Aspect Ratio = 60

Table A.9: Average Nusselt number for dimensionless blind width of 0.5 (Ra_{Wc} = 10 to 10^5, A = 60, W_b / W_c = 0.5, k_b / k_f = 4600, Φ = 0°, 45°, and 75°)

Ra_{Wc}	Φ = 0°	Φ = 45°	Φ = -45°	Φ = 75°
10	1.439	1.243	-	1.056
100	1.439	1.243	-	1.056
1000	1.440	1.244	-	1.060
10^4	1.489	1.303	-	1.154
2 x 10^4	1.557	1.373	-	1.269
4 x 10^4	1.673	1.508	-	1.489
10^5	1.927	1.904	-	1.977

Table A.10: Average Nusselt number for dimensionless blind width of 0.65 (Ra_{Wc} = 10 to 10^5, A = 60, W_b / W_c = 0.65, k_b / k_f = 4600, Φ = 0°, 45°, and 75°)

Ra_{Wc}	Φ = 0°	Φ = 45°	Φ = -45°	Φ = 75°
10	1.678	1.348	-	1.076
100	1.678	1.348	-	1.076
1000	1.679	1.348	-	1.076
10^4	1.743	1.393	-	1.163
2 x 10^4	1.847	1.459	-	1.269
4 x 10^4	2.008	1.578	-	1.474
10^5	2.247	1.847	-	1.950

Table A.11: Average Nusselt number for dimensionless blind width of 0.8 (Ra_{Wc} = 10 to 10^5, A = 60, W_b / W_c = 0.8, k_b / k_f = 4600, Φ = 0°, 45°, and 75°)

Ra_{Wc}	Φ = 0°	Φ = 45°	Φ = -45°	Φ = 75°
10	2.034	1.468	-	1.096
100	2.034	1.468	-	1.096
1000	2.034	1.469	-	1.099
10^4	2.215	1.513	-	1.179
2 x 10^4	2.396	1.586	-	1.274
4 x 10^4	2.612	1.721	-	1.460
10^5	2.952	1.953	-	1.912

Table A.12: Average Nusselt number for dimensionless blind width of 0.9 (Ra_{Wc} = 10 to 10^5, A = 60, W_b / W_c = 0.9, k_b / k_f = 4600, Φ = 0°, 45°, and 75°)

Ra_{Wc}	Φ = 0°	Φ = 45°	Φ = -45°	Φ = 75°
10	2.479	1.572	-	1.111
100	2.479	1.572	-	1.111
1000	2.480	1.573	-	1.112
10^4	2.804	1.630	-	1.177
2 x 10^4	3.089	1.719	-	1.267
4 x 10^4	3.430	1.870	-	1.440
10^5	3.926	2.127	-	1.845

APPENDIX B – AVERAGE NUSSELT NUMBER FOR $k_b / k_f = 15$

B.1 Aspect Ratio = 20

Table B.1: Average Nusselt number for dimensionless blind width of 0.5 (Ra_{Wc} = 10 to 10^5, A = 20, W_b / W_c = 0.5, k_b / k_f = 15, Φ = 0°, 45°, and 75°)

Ra_{Wc}	Φ = 0°	Φ = 45°	Φ = -45°	Φ = 75°
10	1.049	1.028	-	1.008
100	1.049	1.028	-	1.008
1000	1.053	1.035	-	1.019
10^4	1.238	1.263	-	1.321
2 x 10^4	1.457	1.515	-	1.321
4 x 10^4	1.803	1.925	-	2.070
10^5	2.464	2.620	-	2.685

Table B.2: Average Nusselt number for dimensionless blind width of 0.65 (Ra_{Wc} = 10 to 10^5, A = 20, W_b / W_c = 0.65, k_b / k_f = 15, Φ = 0°, 45°, and 75°)

Ra_{Wc}	Φ = 0°	Φ = 45°	Φ = -45°	Φ = 75°
10	1.066	1.037	-	1.011
100	1.066	1.037	-	1.011
1000	1.069	1.041	-	1.016
10^4	1.272	1.221	-	1.277
2 x 10^4	1.513	1.436	-	1.586
4 x 10^4	1.831	1.793	-	2.003
10^5	2.340	2.477	-	2.637

Table B.3: Average Nusselt number for dimensionless blind width of 0.8 (Ra_{Wc} = 10 to 10^5, A = 20, W_b / W_c = 0.8, k_b / k_f = 15, Φ =0°, 45°, and 75°)

Ra_{Wc}	Φ = 0°	Φ = 45°	Φ = -45°	Φ = 75°
10	1.082	1.045	-	1.013
100	1.082	1.045	-	1.013
1000	1.089	1.049	-	1.024
10^4	1.442	1.219	-	1.297
2 x 10^4	1.721	1.421	-	1.592
4 x 10^4	2.053	1.722	-	2.012
10^5	2.581	2.270	-	2.662

Table B.4: Average Nusselt number for dimensionless blind width of 0.9 (Ra_{Wc} = 10 to 10^5, A = 20, W_b / W_c = 0.9, k_b / k_f = 15, Φ = 0°, ±45°, and 75°)

Ra_{Wc}	Φ = 0°	Φ = 45°	Φ = -45°	Φ = 75°
10	1.095	1.051	1.051	1.015
100	1.095	1.051	1.051	1.015
1000	1.113	1.054	1.054	1.024
10^4	1.653	1.245	1.229	1.279
2 x 10^4	1.654	1.455	1.416	1.562
4 x 10^4	2.425	1.738	1.677	1.979
10^5	3.031	2.208	2.142	2.637

B.2 Aspect Ratio = 40

Table B.5: Average Nusselt number for dimensionless blind width of 0.5 (Ra_{Wc} = 10 to 10^5, A = 40, W_b / W_c = 0.5, k_b / k_f = 15, Φ =0°, 45°, and 75°)

Ra_{Wc}	Φ = 0°	Φ = 45°	Φ = -45°	Φ = 75°
10	1.050	1.028	-	1.008
100	1.050	1.028	-	1.008
1000	1.052	1.031	-	1.012
10^4	1.162	1.147	-	1.159
2 x 10^4	1.311	1.281	-	1.345
4 x 10^4	1.548	1.534	-	1.664
10^5	1.994	2.086	-	2.225

Table B.6: Average Nusselt number for dimensionless blind width of 0.65 (Ra_{Wc} = 10 to 10^5, A = 40, W_b / W_c = 0.65, k_b / k_f = 15, Φ = 0°, 45°, and 75°)

Ra_{Wc}	Φ = 0°	Φ = 45°	Φ = -45°	Φ = 75°
10	1.066	1.037	-	1.011
100	1.066	1.037	-	1.011
1000	1.069	1.039	-	1.014
10^4	1.234	1.140	-	1.154
2 x 10^4	1.439	1.272	-	1.329
4 x 10^4	1.709	1.501	-	1.638
10^5	2.103	1.968	-	2.204

Table B.7: Average Nusselt number for dimensionless blind width of 0.8 (Ra_{Wc} = 10 to 10^5, A = 40, W_b / W_c = 0.8, k_b / k_f = 15, Φ = 0°, 45°, and 75°)

Ra_{Wc}	Φ = 0°	Φ = 45°	Φ = -45°	Φ = 75°
10	1.082	1.045	-	1.013
100	1.082	1.045	-	1.013
1000	1.093	1.049	-	1.020
10^4	1.438	1.166	-	1.158
2 x 10^4	1.704	1.316	-	1.317
4 x 10^4	2.013	1.542	-	1.609
10^5	2.495	1.913	-	2.182

Table B.8: Average Nusselt number for dimensionless blind width of 0.9 (Ra_{Wc} = 10 to 10^5, A = 40, W_b / W_c = 0.9, k_b / k_f = 15, Φ = 0°, 45°, and 75°)

Ra_{Wc}	Φ = 0°	Φ = 45°	Φ = -45°	Φ = 75°
10	1.095	1.051	-	1.015
100	1.095	1.051	-	1.015
1000	1.113	1.054	-	1.021
10^4	1.662	1.211	-	1.155
2 x 10^4	2.024	1.384	-	1.303
4 x 10^4	2.415	1.615	-	1.581
10^5	3.006	1.978	-	2.143

B.3 Aspect Ratio = 60

Table B.9: Average Nusselt number for dimensionless blind width of 0.5 (Ra_{Wc} = 10 to 10^5, A = 60, W_b / W_c = 0.5, k_b / k_f = 15, Φ = 0°, 45°, and 75°)

Ra_{Wc}	Φ = 0°	Φ = 45°	Φ = -45°	Φ = 75°
10	1.049	1.028	-	1.008
100	1.049	1.028	-	1.008
1000	1.051	1.030	-	1.013
10^4	1.138	1.110	-	1.117
2 x 10^4	1.264	1.204	-	1.241
4 x 10^4	1.465	1.390	-	1.478
10^5	1.815	1.855	-	1.978

Table B.10: Average Nusselt number for dimensionless blind width of 0.65 (Ra_{Wc} = 10 to 10^5, A = 60, W_b / W_c = 0.65, k_b / k_f = 15, Φ = 0°, 45°, and 75°)

Ra_{Wc}	Φ = 0°	Φ = 45°	Φ = -45°	Φ = 75°
10	1.066	1.036	-	1.011
100	1.066	1.036	-	1.011
1000	1.068	1.039	-	1.014
10^4	1.220	1.113	-	1.111
2 x 10^4	1.416	1.217	-	1.228
4 x 10^4	1.667	1.402	-	1.451
10^5	2.023	1.752	-	1.944

Table B.11: Average Nusselt number for dimensionless blind width of 0.8 (Ra_{Wc} = 10 to 10^5, A = 60, W_b / W_c = 0.8, k_b / k_f = 15, Φ = 0°, 45°, and 75°)

Ra_{Wc}	Φ = 0°	Φ = 45°	Φ = -45°	Φ = 75°
10	1.083	1.045	-	1.013
100	1.083	1.045	-	1.013
1000	1.090	1.047	-	1.017
10^4	1.425	1.143	-	1.112
2 x 10^4	1.687	1.277	-	1.217
4 x 10^4	1.992	1.479	-	1.425
10^5	2.459	1.750	-	1.905

Table B.12: Average Nusselt number for dimensionless blind width of 0.9 (Ra_{Wc} = 10 to 10^5, A = 60, W_b / W_c = 0.9, k_b / k_f = 15, Φ = 0°, 45°, and 75°)

Ra_{Wc}	Φ = 0°	Φ = 45°	Φ = -45°	Φ = 75°
10	1.096	1.052	-	1.015
100	1.096	1.052	-	1.015
1000	1.114	1.054	-	1.017
10^4	1.652	1.194	-	1.099
2 x 10^4	2.010	1.357	-	1.198
4 x 10^4	2.408	1.571	-	1.394
10^5	2.986	1.893	-	1.843

APPENDIX C – WINDOW GEOMETRY GENERATION CODE

When executed, the *Window Geometry Generation Code* generates the entire two-dimensional window/blind geometry. The code also defines all boundary and continuum types, and exports them as a *journal* file, ready for meshing in GAMBIT. The code is written in Microsoft Visual Basic 6.3 which is embedded in Microsoft Office Excel 2003. The following is an example of the non-dimensional input values for a short cavity (A = 5), followed by the output and the code.

C.1 Input

Input

Cavity Dimensions

Cavity Height (m)	5.000000
Cavity Width (m)	1.000000

Calculate

Blade Dimensions

Width (m)	0.900000
Tip-to-Ctr Curve Hgt (m)	0.067500
Thickness (m)	0.006750
Pitch (m)	0.787500
Bottom y-Offset (m)	0.455547
Centre x-Offset (m)	0.000000
Angle (deg)	00.0°

Export File

Clear Output

C.2 Output

```
/ Program name & version: Copy ofWindow Code_rev 28.xls
/Cavity height = 5   Cavity width = 1
/Blade tip to ctr = 0.0675   Balde width = 0.9
/Blade thickness = 0.00675   Blade pitch = 0.7875
/Blade bottom y-offset = 0.455547215582534   Blade centre x-offset = 0   Blade angle = 0°
/Number of blades / cells = 6 / 7
/Date (M/D/Y) and time of output = 1/6/2006 2:47:30 PM
/
solver select "FLUENT 5/6"
/
/
/
vertex create "LBC"    coordinates 0    0
vertex create "RBC"    coordinates 1    0
vertex create "LBB1"   coordinates 0.05    0.3846722
vertex create "MBB1"   coordinates 0.5    0.4521722
vertex create "RBB1"   coordinates 0.95    0.3846722
vertex create "LTB1"   coordinates 0.05    0.3914222
vertex create "MTB1"   coordinates 0.5    0.4589222
vertex create "RTB1"   coordinates 0.95    0.3914222
vertex create "LTC1"   coordinates 0    0.3914222
vertex create "RTC1"   coordinates 1    0.3846722
vertex create "LBB2"   coordinates 0.05    1.1721722
vertex create "MBB2"   coordinates 0.5    1.2396722
vertex create "RBB2"   coordinates 0.95    1.1721722
vertex create "LTB2"   coordinates 0.05    1.1789222
vertex create "MTB2"   coordinates 0.5    1.2464222
vertex create "RTB2"   coordinates 0.95    1.1789222
vertex create "LTC2"   coordinates 0    1.1789222
vertex create "RTC2"   coordinates 1    1.1721722
vertex create "LBB3"   coordinates 0.05    1.9596722
vertex create "MBB3"   coordinates 0.5    2.0271722
vertex create "RBB3"   coordinates 0.95    1.9596722
vertex create "LTB3"   coordinates 0.05    1.9664222
vertex create "MTB3"   coordinates 0.5    2.0339222
vertex create "RTB3"   coordinates 0.95    1.9664222
vertex create "LTC3"   coordinates 0    1.9664222
vertex create "RTC3"   coordinates 1    1.9596722
vertex create "LBB4"   coordinates 0.05    2.7471722
vertex create "MBB4"   coordinates 0.5    2.8146722
vertex create "RBB4"   coordinates 0.95    2.7471722
vertex create "LTB4"   coordinates 0.05    2.7539222
vertex create "MTB4"   coordinates 0.5    2.8214222
vertex create "RTB4"   coordinates 0.95    2.7539222
vertex create "LTC4"   coordinates 0    2.7539222
vertex create "RTC4"   coordinates 1    2.7471722
vertex create "LBB5"   coordinates 0.05    3.5346722
vertex create "MBB5"   coordinates 0.5    3.6021722
vertex create "RBB5"   coordinates 0.95    3.5346722
vertex create "LTB5"   coordinates 0.05    3.5414222
vertex create "MTB5"   coordinates 0.5    3.6089222
vertex create "RTB5"   coordinates 0.95    3.5414222
vertex create "LTC5"   coordinates 0    3.5414222
vertex create "RTC5"   coordinates 1    3.5346722
vertex create "LBB6"   coordinates 0.05    4.3221722
vertex create "MBB6"   coordinates 0.5    4.3896722
vertex create "RBB6"   coordinates 0.95    4.3221722
vertex create "LTB6"   coordinates 0.05    4.3289222
vertex create "MTB6"   coordinates 0.5    4.3964222
vertex create "RTB6"   coordinates 0.95    4.3289222
vertex create "LTC6"   coordinates 0    4.3289222
vertex create "RTC6"   coordinates 1    4.3221722
vertex create "LTC"    coordinates 0    5
vertex create "RTC"    coordinates 1    5
/
edge create  "BC"    straight    "LBC"    "RBC"
```

```
edge create  "LC1"    straight   "LBC"     "LTC1"
edge create  "RC1"    straight   "RBC"     "RTC1"
edge create  "LTC1"   straight   "LTC1"    "LTB1"
edge create  "RTC1"   straight   "RTC1"    "RBB1"
edge create  "LB1"    straight   "LBB1"    "LTB1"
edge create  "RB1"    straight   "RBB1"    "RTB1"
edge create  "BB1"    threepoints "LBB1"   "MBB1"   "RBB1"   arc
edge create  "TB1"    threepoints "LTB1"   "MTB1"   "RTB1"   arc
edge create  "LC2"    straight   "LTC1"    "LTC2"
edge create  "RC2"    straight   "RTC1"    "RTC2"
edge create  "LTC2"   straight   "LTC2"    "LTB2"
edge create  "RTC2"   straight   "RTC2"    "RBB2"
edge create  "LB2"    straight   "LBB2"    "LTB2"
edge create  "RB2"    straight   "RBB2"    "RTB2"
edge create  "BB2"    threepoints "LBB2"   "MBB2"   "RBB2"   arc
edge create  "TB2"    threepoints "LTB2"   "MTB2"   "RTB2"   arc
edge create  "LC3"    straight   "LTC2"    "LTC3"
edge create  "RC3"    straight   "RTC2"    "RTC3"
edge create  "LTC3"   straight   "LTC3"    "LTB3"
edge create  "RTC3"   straight   "RTC3"    "RBB3"
edge create  "LB3"    straight   "LBB3"    "LTB3"
edge create  "RB3"    straight   "RBB3"    "RTB3"
edge create  "BB3"    threepoints "LBB3"   "MBB3"   "RBB3"   arc
edge create  "TB3"    threepoints "LTB3"   "MTB3"   "RTB3"   arc
edge create  "LC4"    straight   "LTC3"    "LTC4"
edge create  "RC4"    straight   "RTC3"    "RTC4"
edge create  "LTC4"   straight   "LTC4"    "LTB4"
edge create  "RTC4"   straight   "RTC4"    "RBB4"
edge create  "LB4"    straight   "LBB4"    "LTB4"
edge create  "RB4"    straight   "RBB4"    "RTB4"
edge create  "BB4"    threepoints "LBB4"   "MBB4"   "RBB4"   arc
edge create  "TB4"    threepoints "LTB4"   "MTB4"   "RTB4"   arc
edge create  "LC5"    straight   "LTC4"    "LTC5"
edge create  "RC5"    straight   "RTC4"    "RTC5"
edge create  "LTC5"   straight   "LTC5"    "LTB5"
edge create  "RTC5"   straight   "RTC5"    "RBB5"
edge create  "LB5"    straight   "LBB5"    "LTB5"
edge create  "RB5"    straight   "RBB5"    "RTB5"
edge create  "BB5"    threepoints "LBB5"   "MBB5"   "RBB5"   arc
edge create  "TB5"    threepoints "LTB5"   "MTB5"   "RTB5"   arc
edge create  "LC6"    straight   "LTC5"    "LTC6"
edge create  "RC6"    straight   "RTC5"    "RTC6"
edge create  "LTC6"   straight   "LTC6"    "LTB6"
edge create  "RTC6"   straight   "RTC6"    "RBB6"
edge create  "LB6"    straight   "LBB6"    "LTB6"
edge create  "RB6"    straight   "RBB6"    "RTB6"
edge create  "BB6"    threepoints "LBB6"   "MBB6"   "RBB6"   arc
edge create  "TB6"    threepoints "LTB6"   "MTB6"   "RTB6"   arc
edge create  "LC7"    straight   "LTC6"    "LTC"
edge create  "RC7"    straight   "RTC6"    "RTC"
edge create  "TC"     straight   "LTC"     "RTC"
/
/Cell face
face create  "C1"   wireframe  "LC1"  "BC"    "RC1"  "RTC1"  "BB1"   "LB1"  "LTC1"  real
face create  "C2"   wireframe  "LC2"  "LTC1"  "TB1"  "RB1"   "RTC1"  "RC2"  "RTC2"  "BB2"
"LB2"   "LTC2"   real
face create  "C3"   wireframe  "LC3"  "LTC2"  "TB2"  "RB2"   "RTC2"  "RC3"  "RTC3"  "BB3"
"LB3"   "LTC3"   real
face create  "C4"   wireframe  "LC4"  "LTC3"  "TB3"  "RB3"   "RTC3"  "RC4"  "RTC4"  "BB4"
"LB4"   "LTC4"   real
face create  "C5"   wireframe  "LC5"  "LTC4"  "TB4"  "RB4"   "RTC4"  "RC5"  "RTC5"  "BB5"
"LB5"   "LTC5"   real
face create  "C6"   wireframe  "LC6"  "LTC5"  "TB5"  "RB5"   "RTC5"  "RC6"  "RTC6"  "BB6"
"LB6"   "LTC6"   real
face create  "C7"   wireframe  "LC7"  "LTC6"  "TB6"  "RB6"   "RTC6"  "RC7"  "TC"    real
/
/Blade face
face create  "B1"   wireframe  "LB1"  "BB1"  "RB1"  "TB1"  real
face create  "B2"   wireframe  "LB2"  "BB2"  "RB2"  "TB2"  real
face create  "B3"   wireframe  "LB3"  "BB3"  "RB3"  "TB3"  real
```

```
face create "B4" wireframe "LB4" "BB4" "RB4" "TB4" real
face create "B5" wireframe "LB5" "BB5" "RB5" "TB5" real
face create "B6" wireframe "LB6" "BB6" "RB6" "TB6" real
/
/Physics create
physics create "Blades" btype "Wall" edge "LB1" "BB1" "RB1" "TB1" "LB2" "BB2"
"RB2" "TB2" "LB3" "BB3" "RB3" "TB3" "LB4" "BB4" "RB4" "TB4" "LB5" "BB5"
"RB5" "TB5" "LB6" "BB6" "RB6" "TB6"
/
physics create "Leftwall" btype "Wall" edge "LC1" "LC2" "LC3" "LC4" "LC5" "LC6"
"LC7"
/
physics create "Rightwall" btype "Wall" edge "RC1" "RC2" "RC3" "RC4" "RC5" "RC6"
"RC7"
/
physics create "Top&BotWall" btype "Wall" edge "TC" "BC"
/
physics create "MyFluid" ctype "FLUID" face "C1" "C2" "C3" "C4" "C5" "C6"
"C7"
/
physics create "MySolid" ctype "SOLID" face "B1" "B2" "B3" "B4" "B5" "B6"
/
/Group create
group create "LC" edge "LC1" "LC2" "LC3" "LC4" "LC5" "LC6" "LC7"
/
group create "RC" edge "RC1" "RC2" "RC3" "RC4" "RC5" "RC6" "RC7"
/
group create "LTC" edge "LTC1" "LTC2" "LTC3" "LTC4" "LTC5" "LTC6"
/
group create "TB" edge "TB1" "TB2" "TB3" "TB4" "TB5" "TB6"
/
group create "RB" edge "RB1" "RB2" "RB3" "RB4" "RB5" "RB6"
/
group create "RTC" edge "RTC1" "RTC2" "RTC3" "RTC4" "RTC5" "RTC6"
/
group create "BB" edge "BB1" "BB2" "BB3" "BB4" "BB5" "BB6"
/
group create "LB" edge "LB1" "LB2" "LB3" "LB4" "LB5" "LB6"
/
group create "TC&BC" edge "TC" "BC"
/
/ End of File
```

C.3 Code

```
'Window Code Generator - Updated on January 6 2006 by Tony Avedissian

Private Sub CommandButton1_Click()

Range("a20:iv65536").ClearContents


Application.ScreenUpdating = False

Application.DisplayStatusBar = True

Application.StatusBar = "Please wait while performing task..."


Sheets("Main Sheet").Select

'Dimensioning variables
Dim h As Double
Dim w As Double
Dim d As Double
```

```
Dim l As Double
Dim t As Double
Dim p As Double
Dim s As Double
Dim f As Double
Dim a As Double
Dim n As Integer
Dim i As Integer

'input
h = Range("c5").Value
w = Range("c6").Value
l = Range("c10").Value
d = Range("c11").Value
t = Range("c12").Value
p = Range("c13").Value
s = Range("c14").Value
f = Range("c15").Value
a = (Range("c16").Value * 3.14159265358979 / 180)

'File information
Range("b20").Value = "/ Program name & version: " & ActiveWorkbook.Name
Range("b21").Value = "/Cavity height = " & h & "   Cavity width = " & w
Range("b22").Value = "/Blade tip to ctr = " & d & "   Balde width = " & l
Range("b23").Value = "/Blade thickness = " & t & "   Blade pitch = " & p
Range("b24").Value = "/Blade bottom y-offset = " & s & "   Blade centre x-offset = " & Range("c15").Value & "   Blade angle = " & Range("c16").Value & "°"

'Number of blades
n = Int((h - (2 * s)) / p + 1)

Range("b25").Value = "/Number of blades / cells = " & n & " / " & n + 1
Range("b26").Value = "/Date (M/D/Y) and time of output = " & Now
Range("b27").Value = "/"
Range("b28").Value = "solver select ""FLUENT 5/6"" "
Range("b29").Value = "/"
Range("b30").Value = "/"
Range("b31").Value = "/"

Range("a32").Select

'vertex create

'cavity very bottom left
ActiveCell.Offset(0, 1).Select
ActiveCell.Value = "vertex create"
ActiveCell.Offset(0, 1).Select
ActiveCell.Value = """LBC"""
ActiveCell.Offset(0, 1).Select
ActiveCell.Value = "coordinates"
ActiveCell.Offset(0, 1).Select
ActiveCell.Value = 0
ActiveCell.Offset(0, 1).Select
ActiveCell.Value = 0
ActiveCell.Offset(1, -5).Select

'cavity very bottom right
ActiveCell.Offset(0, 1).Select
ActiveCell.Value = "vertex create"
ActiveCell.Offset(0, 1).Select
ActiveCell.Value = """RBC"""
ActiveCell.Offset(0, 1).Select
ActiveCell.Value = "coordinates"
ActiveCell.Offset(0, 1).Select
ActiveCell.Value = w
ActiveCell.Offset(0, 1).Select
ActiveCell.Value = 0
```

```
ActiveCell.Offset(1, -5).Select

For i = 1 To n

'cell number
ActiveCell.Value = i
ActiveCell.Offset(0, 1).Select

'left bottom
ActiveCell.Value = "vertex create"
ActiveCell.Offset(0, 1).Select
ActiveCell.Value = """LBB" & i & """"
ActiveCell.Offset(0, 1).Select
ActiveCell.Value = "coordinates"
ActiveCell.Offset(0, 1).Select
ActiveCell.Value = ((w / 2) - ((l / 2) * Cos(a))) + (((d + (t / 2)) * Sin(a))) + f
ActiveCell.Offset(0, 1).Select
ActiveCell.Value = (s - ((d + (t / 2)) * Cos(a)) - ((l / 2) * Sin(a)))
ActiveCell.Offset(1, -4).Select

'middle bottom
ActiveCell.Value = "vertex create"
ActiveCell.Offset(0, 1).Select
ActiveCell.Value = """MBB" & i & """"
ActiveCell.Offset(0, 1).Select
ActiveCell.Value = "coordinates"
ActiveCell.Offset(0, 1).Select
ActiveCell.Value = ((w / 2) + (t / 2) * Sin(a)) + f
ActiveCell.Offset(0, 1).Select
ActiveCell.Value = (s - ((t / 2) * Cos(a)))
ActiveCell.Offset(1, -4).Select

'right bottom
ActiveCell.Value = "vertex create"
ActiveCell.Offset(0, 1).Select
ActiveCell.Value = """RBB" & i & """"
ActiveCell.Offset(0, 1).Select
ActiveCell.Value = "coordinates"
ActiveCell.Offset(0, 1).Select
ActiveCell.Value = ((w / 2) + ((l / 2) * Cos(a)) + (((d + (t / 2)) * Sin(a)))) + f
ActiveCell.Offset(0, 1).Select
ActiveCell.Value = (s - ((d + (t / 2)) * Cos(a)) + ((l / 2) * Sin(a)))
ActiveCell.Offset(1, -4).Select

t = -t

'left top
ActiveCell.Value = "vertex create"
ActiveCell.Offset(0, 1).Select
ActiveCell.Value = """LTB" & i & """"
ActiveCell.Offset(0, 1).Select
ActiveCell.Value = "coordinates"
ActiveCell.Offset(0, 1).Select
ActiveCell.Value = ((w / 2) - ((l / 2) * Cos(a))) + (((d + (t / 2)) * Sin(a))) + f
ActiveCell.Offset(0, 1).Select
ActiveCell.Value = (s - ((d + (t / 2)) * Cos(a)) - ((l / 2) * Sin(a)))
ActiveCell.Offset(1, -4).Select

'middle top
ActiveCell.Value = "vertex create"
ActiveCell.Offset(0, 1).Select
ActiveCell.Value = """MTB" & i & """"
ActiveCell.Offset(0, 1).Select
ActiveCell.Value = "coordinates"
ActiveCell.Offset(0, 1).Select
ActiveCell.Value = ((w / 2) + (t / 2) * Sin(a)) + f
ActiveCell.Offset(0, 1).Select
ActiveCell.Value = (s - ((t / 2) * Cos(a)))
ActiveCell.Offset(1, -4).Select
```

```
'right top
ActiveCell.Value = "vertex create"
ActiveCell.Offset(0, 1).Select
ActiveCell.Value = """RTB" & i & """"
ActiveCell.Offset(0, 1).Select
ActiveCell.Value = "coordinates"
ActiveCell.Offset(0, 1).Select
ActiveCell.Value = ((w / 2) + ((l / 2) * Cos(a)) + ((d + (t / 2)) * Sin(a))) + f
ActiveCell.Offset(0, 1).Select
ActiveCell.Value = (s - ((d + (t / 2)) * Cos(a)) + ((l / 2) * Sin(a)))
ActiveCell.Offset(1, -4).Select

t = -t

'cavity left
ActiveCell.Value = "vertex create"
ActiveCell.Offset(0, 1).Select
ActiveCell.Value = """LTC" & i & """"
ActiveCell.Offset(0, 1).Select
ActiveCell.Value = "coordinates"
ActiveCell.Offset(0, 1).Select
ActiveCell.Value = 0
ActiveCell.Offset(0, 1).Select
ActiveCell.Value = ActiveCell.Offset(-3, 0).Value
ActiveCell.Offset(1, -4).Select

'cavity right
ActiveCell.Value = "vertex create"
ActiveCell.Offset(0, 1).Select
ActiveCell.Value = """RTC" & i & """"
ActiveCell.Offset(0, 1).Select
ActiveCell.Value = "coordinates"
ActiveCell.Offset(0, 1).Select
ActiveCell.Value = w
ActiveCell.Offset(0, 1).Select
ActiveCell.Value = ActiveCell.Offset(-5, 0).Value
ActiveCell.Offset(1, -5).Select

'pitch add
s = s + p

Next i

'cavity very top left
ActiveCell.Offset(0, 1).Select
ActiveCell.Value = "vertex create"
ActiveCell.Offset(0, 1).Select
ActiveCell.Value = """LTC"""
ActiveCell.Offset(0, 1).Select
ActiveCell.Value = "coordinates"
ActiveCell.Offset(0, 1).Select
ActiveCell.Value = 0
ActiveCell.Offset(0, 1).Select
ActiveCell.Value = h
ActiveCell.Offset(1, -5).Select

'cavity very top right
ActiveCell.Offset(0, 1).Select
ActiveCell.Value = "vertex create"
ActiveCell.Offset(0, 1).Select
ActiveCell.Value = """RTC"""
ActiveCell.Offset(0, 1).Select
ActiveCell.Value = "coordinates"
ActiveCell.Offset(0, 1).Select
ActiveCell.Value = w
ActiveCell.Offset(0, 1).Select
ActiveCell.Value = h
ActiveCell.Offset(1, -4).Select
```

```
'edge create

ActiveCell.Value = "/"
ActiveCell.Offset(1, 0).Select

'Bottom cell
ActiveCell.Value = "edge create"
ActiveCell.Offset(0, 1).Select
ActiveCell.Value = """BC"""
ActiveCell.Offset(0, 1).Select
ActiveCell.Value = "straight"
ActiveCell.Offset(0, 1).Select
ActiveCell.Value = """LBC"""
ActiveCell.Offset(0, 1).Select
ActiveCell.Value = """RBC"""
ActiveCell.Offset(1, -4).Select

ActiveCell.Value = "edge create"
ActiveCell.Offset(0, 1).Select
ActiveCell.Value = """LC1"""
ActiveCell.Offset(0, 1).Select
ActiveCell.Value = "straight"
ActiveCell.Offset(0, 1).Select
ActiveCell.Value = """LBC"""
ActiveCell.Offset(0, 1).Select
ActiveCell.Value = """LTC1"""
ActiveCell.Offset(1, -4).Select

ActiveCell.Value = "edge create"
ActiveCell.Offset(0, 1).Select
ActiveCell.Value = """RC1"""
ActiveCell.Offset(0, 1).Select
ActiveCell.Value = "straight"
ActiveCell.Offset(0, 1).Select
ActiveCell.Value = """RBC"""
ActiveCell.Offset(0, 1).Select
ActiveCell.Value = """RTC1"""
ActiveCell.Offset(1, -5).Select

For i = 1 To n

ActiveCell.Value = i
ActiveCell.Offset(0, 1).Select

If i <> 1 Then

'left cell
ActiveCell.Value = "edge create"
ActiveCell.Offset(0, 1).Select
ActiveCell.Value = """LC" & i & """"
ActiveCell.Offset(0, 1).Select
ActiveCell.Value = "straight"
ActiveCell.Offset(0, 1).Select
ActiveCell.Value = """LTC" & (i - 1) & """"
ActiveCell.Offset(0, 1).Select
ActiveCell.Value = """LTC" & i & """"
ActiveCell.Offset(1, -4).Select

'right cell
ActiveCell.Value = "edge create"
ActiveCell.Offset(0, 1).Select
ActiveCell.Value = """RC" & i & """"
ActiveCell.Offset(0, 1).Select
ActiveCell.Value = "straight"
ActiveCell.Offset(0, 1).Select
ActiveCell.Value = """RTC" & (i - 1) & """"
ActiveCell.Offset(0, 1).Select
ActiveCell.Value = """RTC" & i & """"
ActiveCell.Offset(1, -4).Select
```

```
End If

'Top cell left
ActiveCell.Value = "edge create"
ActiveCell.Offset(0, 1).Select
ActiveCell.Value = """LTC" & i & """"
ActiveCell.Offset(0, 1).Select
ActiveCell.Value = "straight"
ActiveCell.Offset(0, 1).Select
ActiveCell.Value = """LTC" & i & """"
ActiveCell.Offset(0, 1).Select
ActiveCell.Value = """LTB" & i & """"
ActiveCell.Offset(1, -4).Select

'Top cell right
ActiveCell.Value = "edge create"
ActiveCell.Offset(0, 1).Select
ActiveCell.Value = """RTC" & i & """"
ActiveCell.Offset(0, 1).Select
ActiveCell.Value = "straight"
ActiveCell.Offset(0, 1).Select
ActiveCell.Value = """RTC" & i & """"
ActiveCell.Offset(0, 1).Select
ActiveCell.Value = """RBB" & i & """"
ActiveCell.Offset(1, -4).Select

'left blade thickness
ActiveCell.Value = "edge create"
ActiveCell.Offset(0, 1).Select
ActiveCell.Value = """LB" & i & """"
ActiveCell.Offset(0, 1).Select
ActiveCell.Value = "straight"
ActiveCell.Offset(0, 1).Select
ActiveCell.Value = """LBB" & i & """"
ActiveCell.Offset(0, 1).Select
ActiveCell.Value = """LTB" & i & """"
ActiveCell.Offset(1, -4).Select

'right blade thickness
ActiveCell.Value = "edge create"
ActiveCell.Offset(0, 1).Select
ActiveCell.Value = """RB" & i & """"
ActiveCell.Offset(0, 1).Select
ActiveCell.Value = "straight"
ActiveCell.Offset(0, 1).Select
ActiveCell.Value = """RBB" & i & """"
ActiveCell.Offset(0, 1).Select
ActiveCell.Value = """RTB" & i & """"
ActiveCell.Offset(1, -4).Select

'blade bottom
ActiveCell.Value = "edge create"
ActiveCell.Offset(0, 1).Select
ActiveCell.Value = """BB" & i & """"
ActiveCell.Offset(0, 1).Select
ActiveCell.Value = "threepoints"
ActiveCell.Offset(0, 1).Select
ActiveCell.Value = """LBB" & i & """"
ActiveCell.Offset(0, 1).Select
ActiveCell.Value = """MBB" & i & """"
ActiveCell.Offset(0, 1).Select
ActiveCell.Value = """RBB" & i & """"
ActiveCell.Offset(0, 1).Select
ActiveCell.Value = "arc"
ActiveCell.Offset(1, -6).Select

'blade top
ActiveCell.Value = "edge create"
ActiveCell.Offset(0, 1).Select
ActiveCell.Value = """TB" & i & """"
```

```
ActiveCell.Offset(0, 1).Select
ActiveCell.Value = "threepoints"
ActiveCell.Offset(0, 1).Select
ActiveCell.Value = """LTB" & i & """"
ActiveCell.Offset(0, 1).Select
ActiveCell.Value = """MTB" & i & """"
ActiveCell.Offset(0, 1).Select
ActiveCell.Value = """RTB" & i & """"
ActiveCell.Offset(0, 1).Select
ActiveCell.Value = "arc"
ActiveCell.Offset(1, -7).Select

Next i

ActiveCell.Offset(0, 1).Select

'Top cell
ActiveCell.Value = "edge create"
ActiveCell.Offset(0, 1).Select
ActiveCell.Value = """LC" & i & """"
ActiveCell.Offset(0, 1).Select
ActiveCell.Value = "straight"
ActiveCell.Offset(0, 1).Select
ActiveCell.Value = """LTC" & (i - 1) & """"
ActiveCell.Offset(0, 1).Select
ActiveCell.Value = """LTC"""
ActiveCell.Offset(1, -4).Select

ActiveCell.Value = "edge create"
ActiveCell.Offset(0, 1).Select
ActiveCell.Value = """RC" & i & """"
ActiveCell.Offset(0, 1).Select
ActiveCell.Value = "straight"
ActiveCell.Offset(0, 1).Select
ActiveCell.Value = """RTC" & (i - 1) & """"
ActiveCell.Offset(0, 1).Select
ActiveCell.Value = """RTC"""
ActiveCell.Offset(1, -4).Select

ActiveCell.Value = "edge create"
ActiveCell.Offset(0, 1).Select
ActiveCell.Value = """TC"""
ActiveCell.Offset(0, 1).Select
ActiveCell.Value = "straight"
ActiveCell.Offset(0, 1).Select
ActiveCell.Value = """LTC"""
ActiveCell.Offset(0, 1).Select
ActiveCell.Value = """RTC"""
ActiveCell.Offset(1, -4).Select

'Cell face create
ActiveCell.Value = "/"
ActiveCell.Offset(1, 0).Select
ActiveCell.Value = "/Cell face "
ActiveCell.Offset(1, -1).Select
ActiveCell.Value = 1
ActiveCell.Offset(0, 1).Select

'Bottom face
ActiveCell.Value = "face create"
ActiveCell.Offset(0, 1).Select
ActiveCell.Value = """C1"""
ActiveCell.Offset(0, 1).Select
ActiveCell.Value = "wireframe"
ActiveCell.Offset(0, 1).Select
ActiveCell.Value = """LC1"""
ActiveCell.Offset(0, 1).Select
ActiveCell.Value = """BC"""
ActiveCell.Offset(0, 1).Select
ActiveCell.Value = """RC1"""
```

```
ActiveCell.Offset(0, 1).Select
ActiveCell.Value = """RTC1"""
ActiveCell.Offset(0, 1).Select
ActiveCell.Value = """BB1"""
ActiveCell.Offset(0, 1).Select
ActiveCell.Value = """LB1"""
ActiveCell.Offset(0, 1).Select
ActiveCell.Value = """LTC1"""
ActiveCell.Offset(0, 1).Select
ActiveCell.Value = "real"
ActiveCell.Offset(1, -11).Select

For i = 2 To n

ActiveCell.Value = i
ActiveCell.Offset(0, 1).Select
ActiveCell.Value = "face create"
ActiveCell.Offset(0, 1).Select
ActiveCell.Value = """C" & i & """"
ActiveCell.Offset(0, 1).Select
ActiveCell.Value = "wireframe"
ActiveCell.Offset(0, 1).Select
ActiveCell.Value = """LC" & i & """"
ActiveCell.Offset(0, 1).Select
ActiveCell.Value = """LTC" & (i - 1) & """"
ActiveCell.Offset(0, 1).Select
ActiveCell.Value = """TB" & (i - 1) & """"
ActiveCell.Offset(0, 1).Select
ActiveCell.Value = """RB" & (i - 1) & """"
ActiveCell.Offset(0, 1).Select
ActiveCell.Value = """RTC" & (i - 1) & """"
ActiveCell.Offset(0, 1).Select
ActiveCell.Value = """RC" & i & """"
ActiveCell.Offset(0, 1).Select
ActiveCell.Value = """RTC" & i & """"
ActiveCell.Offset(0, 1).Select
ActiveCell.Value = """BB" & i & """"
ActiveCell.Offset(0, 1).Select
ActiveCell.Value = """LB" & i & """"
ActiveCell.Offset(0, 1).Select
ActiveCell.Value = """LTC" & i & """"
ActiveCell.Offset(0, 1).Select
ActiveCell.Value = "real"
ActiveCell.Offset(1, -14).Select

Next i



ActiveCell.Value = i
ActiveCell.Offset(0, 1).Select

'Top Face
ActiveCell.Value = "face create"
ActiveCell.Offset(0, 1).Select
ActiveCell.Value = """C" & i & """"
ActiveCell.Offset(0, 1).Select
ActiveCell.Value = "wireframe"
ActiveCell.Offset(0, 1).Select
ActiveCell.Value = """LC" & i & """"
ActiveCell.Offset(0, 1).Select
ActiveCell.Value = """LTC" & (i - 1) & """"
ActiveCell.Offset(0, 1).Select
ActiveCell.Value = """TB" & (i - 1) & """"
ActiveCell.Offset(0, 1).Select
ActiveCell.Value = """RB" & (i - 1) & """"
ActiveCell.Offset(0, 1).Select
ActiveCell.Value = """RTC" & (i - 1) & """"
ActiveCell.Offset(0, 1).Select
ActiveCell.Value = """RC" & i & """"
```

```
ActiveCell.Offset(0, 1).Select
ActiveCell.Value = """TC"""
ActiveCell.Offset(0, 1).Select
ActiveCell.Value = "real"
ActiveCell.Offset(1, -10).Select

'Blade face create
ActiveCell.Value = "/ "
ActiveCell.Offset(1, 0).Select
ActiveCell.Value = "/Blade face "
ActiveCell.Offset(1, -1).Select

For i = 1 To n

ActiveCell.Value = i
ActiveCell.Offset(0, 1).Select

ActiveCell.Value = "face create"
ActiveCell.Offset(0, 1).Select
ActiveCell.Value = """B" & i & """"
ActiveCell.Offset(0, 1).Select
ActiveCell.Value = "wireframe"
ActiveCell.Offset(0, 1).Select
ActiveCell.Value = """LB" & i & """"
ActiveCell.Offset(0, 1).Select
ActiveCell.Value = """BB" & i & """"
ActiveCell.Offset(0, 1).Select
ActiveCell.Value = """RB" & i & """"
ActiveCell.Offset(0, 1).Select
ActiveCell.Value = """TB" & i & """"
ActiveCell.Offset(0, 1).Select
ActiveCell.Value = "real"
ActiveCell.Offset(1, -8).Select

Next i


'Physics create (Boundary)

'Blades
ActiveCell.Offset(0, 1).Select
ActiveCell.Value = "/ "
ActiveCell.Offset(1, 0).Select
ActiveCell.Value = "/Physics create "
ActiveCell.Offset(1, 0).Select
ActiveCell.Value = "physics create"
ActiveCell.Offset(0, 1).Select
ActiveCell.Value = """Blades"""
ActiveCell.Offset(0, 1).Select
ActiveCell.Value = "btype"
ActiveCell.Offset(0, 1).Select
ActiveCell.Value = """Wall"""
ActiveCell.Offset(0, 1).Select
ActiveCell.Value = "edge"
ActiveCell.Offset(0, 1).Select

For i = 1 To n

ActiveCell.Value = """LB" & i & """"
ActiveCell.Offset(0, 1).Select
ActiveCell.Value = """BB" & i & """"
ActiveCell.Offset(0, 1).Select
ActiveCell.Value = """RB" & i & """"
ActiveCell.Offset(0, 1).Select
ActiveCell.Value = """TB" & i & """"
ActiveCell.Offset(0, 1).Select

If ActiveCell.Column > 200 Then
If i <> n Then
ActiveCell.Value = "\"
```

```
End If

If i < 50 Then
ActiveCell.Offset(1, -201).Select

Else: ActiveCell.Offset(1, -200).Select
End If
End If

Next i

'Left wall
i = ActiveCell.Column
ActiveCell.Offset(1, -i + 2).Select
ActiveCell.Value = "/ "
ActiveCell.Offset(1, 0).Select
ActiveCell.Value = "physics create"
ActiveCell.Offset(0, 1).Select
ActiveCell.Value = """Leftwall"""
ActiveCell.Offset(0, 1).Select
ActiveCell.Value = "btype"
ActiveCell.Offset(0, 1).Select
ActiveCell.Value = """Wall"""
ActiveCell.Offset(0, 1).Select
ActiveCell.Value = "edge"
ActiveCell.Offset(0, 1).Select

For i = 1 To n + 1
ActiveCell.Value = """LC" & i & """"
ActiveCell.Offset(0, 1).Select

Next i

'Right wall
ActiveCell.Offset(1, -(i + 4)).Select
ActiveCell.Value = "/ "
ActiveCell.Offset(1, 0).Select
ActiveCell.Value = "physics create"
ActiveCell.Offset(0, 1).Select
ActiveCell.Value = """Rightwall"""
ActiveCell.Offset(0, 1).Select
ActiveCell.Value = "btype"
ActiveCell.Offset(0, 1).Select
ActiveCell.Value = """Wall"""
ActiveCell.Offset(0, 1).Select
ActiveCell.Value = "edge"
ActiveCell.Offset(0, 1).Select

For i = 1 To n + 1
ActiveCell.Value = """RC" & i & """"
ActiveCell.Offset(0, 1).Select

Next i

'Top and bottom wall
ActiveCell.Offset(1, -(i + 4)).Select
ActiveCell.Value = "/ "
ActiveCell.Offset(1, 0).Select
ActiveCell.Value = "physics create"
ActiveCell.Offset(0, 1).Select
ActiveCell.Value = """Top&BotWall"""
ActiveCell.Offset(0, 1).Select
ActiveCell.Value = "btype"
ActiveCell.Offset(0, 1).Select
ActiveCell.Value = """Wall"""
ActiveCell.Offset(0, 1).Select
ActiveCell.Value = "edge"
ActiveCell.Offset(0, 1).Select
ActiveCell.Value = """TC"""
ActiveCell.Offset(0, 1).Select
```

```
ActiveCell.Value = """BC"""

'Physics create (Continuum)

'Cells "MyFluid"
i = ActiveCell.Column
ActiveCell.Offset(1, -i + 2).Select
ActiveCell.Value = "/ "
ActiveCell.Offset(1, 0).Select
ActiveCell.Value = "physics create"
ActiveCell.Offset(0, 1).Select
ActiveCell.Value = """MyFluid"""
ActiveCell.Offset(0, 1).Select
ActiveCell.Value = "ctype"
ActiveCell.Offset(0, 1).Select
ActiveCell.Value = """FLUID"""
ActiveCell.Offset(0, 1).Select
ActiveCell.Value = "face"
ActiveCell.Offset(0, 1).Select

For i = 1 To n + 1
ActiveCell.Value = """C" & i & """"
ActiveCell.Offset(0, 1).Select

Next i

'Blades "MySolid"
i = ActiveCell.Column
ActiveCell.Offset(1, -i + 2).Select
ActiveCell.Value = "/ "
ActiveCell.Offset(1, 0).Select
ActiveCell.Value = "physics create"
ActiveCell.Offset(0, 1).Select
ActiveCell.Value = """MySolid"""
ActiveCell.Offset(0, 1).Select
ActiveCell.Value = "ctype"
ActiveCell.Offset(0, 1).Select
ActiveCell.Value = """SOLID"""
ActiveCell.Offset(0, 1).Select
ActiveCell.Value = "face"
ActiveCell.Offset(0, 1).Select

For i = 1 To n
ActiveCell.Value = """B" & i & """"
ActiveCell.Offset(0, 1).Select

Next i

'Group Create
i = ActiveCell.Column
ActiveCell.Offset(1, -i + 2).Select
ActiveCell.Value = "/ "
ActiveCell.Offset(1, 0).Select
ActiveCell.Value = "/Group create "
ActiveCell.Offset(1, 0).Select
ActiveCell.Value = "group create"
ActiveCell.Offset(0, 1).Select
ActiveCell.Value = """LC"""
ActiveCell.Offset(0, 1).Select
ActiveCell.Value = "edge"
ActiveCell.Offset(0, 1).Select

For i = 1 To n + 1
ActiveCell.Value = """LC" & i & """"
ActiveCell.Offset(0, 1).Select

Next i

ActiveCell.Offset(1, -(i + 2)).Select
ActiveCell.Value = "/ "
```

```
ActiveCell.Offset(1, 0).Select
ActiveCell.Value = "group create"
ActiveCell.Offset(0, 1).Select
ActiveCell.Value = """RC"""
ActiveCell.Offset(0, 1).Select
ActiveCell.Value = "edge"
ActiveCell.Offset(0, 1).Select

For i = 1 To n + 1
ActiveCell.Value = """RC" & i & """"
ActiveCell.Offset(0, 1).Select

Next i

ActiveCell.Offset(1, -(i + 2)).Select
ActiveCell.Value = "/ "
ActiveCell.Offset(1, 0).Select
ActiveCell.Value = "group create"
ActiveCell.Offset(0, 1).Select
ActiveCell.Value = """LTC"""
ActiveCell.Offset(0, 1).Select
ActiveCell.Value = "edge"
ActiveCell.Offset(0, 1).Select

For i = 1 To n
ActiveCell.Value = """LTC" & i & """"
ActiveCell.Offset(0, 1).Select

Next i

ActiveCell.Offset(1, -(i + 2)).Select
ActiveCell.Value = "/ "
ActiveCell.Offset(1, 0).Select
ActiveCell.Value = "group create"
ActiveCell.Offset(0, 1).Select
ActiveCell.Value = """TB"""
ActiveCell.Offset(0, 1).Select
ActiveCell.Value = "edge"
ActiveCell.Offset(0, 1).Select

For i = 1 To n
ActiveCell.Value = """TB" & i & """"
ActiveCell.Offset(0, 1).Select

Next i

ActiveCell.Offset(1, -(i + 2)).Select
ActiveCell.Value = "/ "
ActiveCell.Offset(1, 0).Select
ActiveCell.Value = "group create"
ActiveCell.Offset(0, 1).Select
ActiveCell.Value = """RB"""
ActiveCell.Offset(0, 1).Select
ActiveCell.Value = "edge"
ActiveCell.Offset(0, 1).Select

For i = 1 To n
ActiveCell.Value = """RB" & i & """"
ActiveCell.Offset(0, 1).Select

Next i

ActiveCell.Offset(1, -(i + 2)).Select
ActiveCell.Value = "/ "
ActiveCell.Offset(1, 0).Select
ActiveCell.Value = "group create"
ActiveCell.Offset(0, 1).Select
ActiveCell.Value = """RTC"""
ActiveCell.Offset(0, 1).Select
ActiveCell.Value = "edge"
```

```
ActiveCell.Offset(0, 1).Select

For i = 1 To n
ActiveCell.Value = """RTC" & i & """"
ActiveCell.Offset(0, 1).Select

Next i

ActiveCell.Offset(1, -(i + 2)).Select
ActiveCell.Value = "/ "
ActiveCell.Offset(1, 0).Select
ActiveCell.Value = "group create"
ActiveCell.Offset(0, 1).Select
ActiveCell.Value = """BB"""
ActiveCell.Offset(0, 1).Select
ActiveCell.Value = "edge"
ActiveCell.Offset(0, 1).Select

For i = 1 To n
ActiveCell.Value = """BB" & i & """"
ActiveCell.Offset(0, 1).Select

Next i

ActiveCell.Offset(1, -(i + 2)).Select
ActiveCell.Value = "/ "
ActiveCell.Offset(1, 0).Select
ActiveCell.Value = "group create"
ActiveCell.Offset(0, 1).Select
ActiveCell.Value = """LB"""
ActiveCell.Offset(0, 1).Select
ActiveCell.Value = "edge"
ActiveCell.Offset(0, 1).Select

For i = 1 To n
ActiveCell.Value = """LB" & i & """"
ActiveCell.Offset(0, 1).Select

Next i

ActiveCell.Offset(1, -(i + 2)).Select
ActiveCell.Value = "/ "
ActiveCell.Offset(1, 0).Select
ActiveCell.Value = "group create"
ActiveCell.Offset(0, 1).Select
ActiveCell.Value = """TC&BC"""
ActiveCell.Offset(0, 1).Select
ActiveCell.Value = "edge"
ActiveCell.Offset(0, 1).Select
ActiveCell.Value = """TC"""
ActiveCell.Offset(0, 1).Select
ActiveCell.Value = """BC"""
ActiveCell.Offset(1, -4).Select
ActiveCell.Value = "/ "
ActiveCell.Offset(1, 0).Select
ActiveCell.Value = "/ End of File"


'Message
Application.StatusBar = "Calculations Done"


If MsgBox(8 * n + 4 & " Vertext (x,y) calculations completed." & vbCrLf & 8 * n + 4 & " Edges created." _
& vbCrLf & (2 * n + 1) & " Faces created." & vbCrLf & "Export code?", vbQuestion + vbYesNo, "Calculations Done") = vbYes
Then

CommandButton3_Click

Else
```

```
Range("c4").Select
End If

Application.StatusBar = False

End Sub

Private Sub CommandButton2_Click()

'Clear sheet
Range("a20:iv65536").ClearContents

End Sub

'File Export
Private Sub CommandButton3_Click()

'Dimensioning variables
Dim FileDest As String
Dim FileNum As Integer
Dim j As Integer
Dim k As Integer

'Prompt user for destination file name
FileDest = InputBox("Enter file destination" & vbCrLf & "(complete path, file name and extention):", "File Export", "C:\Documents
and Settings\All Users\Desktop\" & _Range("c5").Value & "Hc " & Range("c6").Value & "Wc "& Range("c10").Value & "Wb " &
Range("c16").Value & "deg.jou")

'Obtain next free file handle number
FileNum = FreeFile()
'Turn error checking off
On Error Resume Next
'Attempt to open destination file for output
Open FileDest For Output As #FileNum
'If an error occurs report it and end
If Err <> 0 Then

MsgBox "File " & FileDest & "was not exported", vbCritical, "Export Error"
End
End If

'Turn error checking on
On Error GoTo 0
'Export range
Range("b20").Select

j = 0
k = 0

Do While Not IsEmpty(ActiveCell.Offset(j, k))
Do While Not IsEmpty(ActiveCell.Offset(j, k))
'ActiveCell.Offset(j, K).Value = "output"
Print #FileNum, ActiveCell.Offset(j, k).Text,
k = k + 1

Loop

Print #FileNum,

k = 0
j = j + 1
Loop

'Close destination file
Close #FileNum
Range("c4").Select
End Sub
```

APPENDIX D – VIEW FACTOR CALCULATOR CODE

When executed, the *View Factor Calculator Code* generates the view factors for up to 10 surfaces. The code is based on Hottel's Crossed String method [46]. The code is written in Microsoft Visual Basic 6.3 which is embedded in Microsoft Office Excel 2003. The following is an example of a four sided geometry coordinate input (typical for this study), followed by the output and the code.

D.1 Input

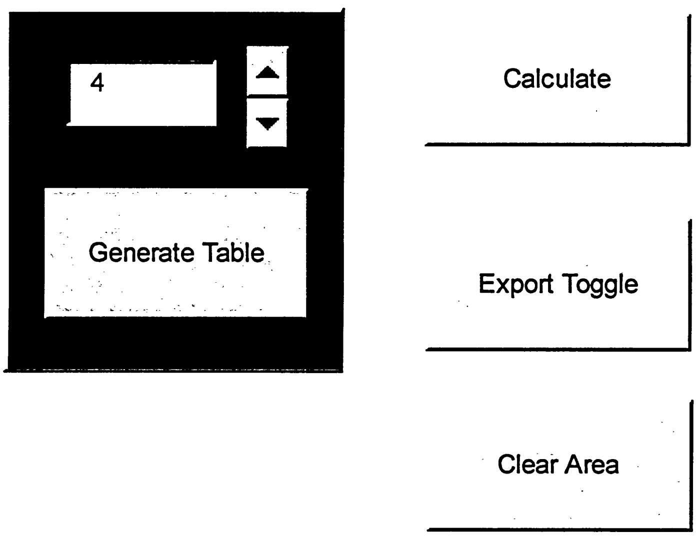

Surface1	Point 1 x =	0
	Point 1 y =	0
	Point 2 x =	0
	Point 2 y =	11.844
	Area =	11.844
Surface2	Point 1 x =	0
	Point 1 y =	11.844
	Point 2 x =	14.79
	Point 2 y =	37.461
	Area =	29.58
Surface3	Point 1 x =	14.79
	Point 1 y =	37.461
	Point 2 x =	14.79
	Point 2 y =	25.61703
	Area =	11.844
Surface4	Point 1 x =	14.79
	Point 1 y =	25.61703
	Point 2 x =	0
	Point 2 y =	0
	Area =	29.58

D.2 Output

F1->2	0.048507045
F1->3	0.055930257
F1->4	0.895562698
F Sum	1
F2->1	0.019422496
F2->3	0.358587399
F2->4	0.621989184
F Sum	0.999999079
F3->1	0.055930257
F3->2	0.895560221
F3->4	0.048506868
F Sum	0.999997345
F4->1	0.358588391
F4->2	0.621989184
F4->3	0.019422425
F Sum	1

D.3 Code

```
Private Sub CommandButton1_Click()

Range("a20:iv65536").Clear

Dim i As Integer
Dim j As Integer
Dim n As Integer

Range("b22").Select

'input loop

n = TextBox1.Value

For i = 1 To n

ActiveCell.Value = "Surface" & i
ActiveCell.Offset(0, 1).Select
ActiveCell.Value = "Point 1 x ="
ActiveCell.Offset(1, 0).Select
ActiveCell.Value = "Point 1 y ="
ActiveCell.Offset(1, 0).Select
ActiveCell.Value = "Point 2 x ="
ActiveCell.Offset(1, 0).Select
ActiveCell.Value = "Point 2 y ="
ActiveCell.Offset(1, 0).Select
ActiveCell.Value = "Area ="
ActiveCell.Offset(2, -1).Select

Next i

ActiveCell.Offset(-6 * n, 2).Select

End Sub

Private Sub CommandButton2_Click()

Dim i As Integer
Dim j As Integer
Dim n As Integer
Dim xa(10) As Double
Dim ya(10) As Double
Dim xb(10) As Double
Dim yb(10) As Double
Dim A(10) As Double
Dim scxa(10) As Double
Dim scya(10) As Double
Dim scxb(10) As Double
Dim scyb(10) As Double
Dim suxa(10) As Double
Dim suya(10) As Double
Dim suxb(10) As Double
Dim suyb(10) As Double
Dim sc(10) As Double
Dim su(10) As Double
Dim F(10, 10) As Double
Dim Fsum As Double

Range("d22").Select

n = TextBox1.Value

For i = 1 To n

xa(i) = ActiveCell.Value
ya(i) = ActiveCell.Offset(1, 0).Value
```

```
xb(i) = ActiveCell.Offset(2, 0).Value
yb(i) = ActiveCell.Offset(3, 0).Value
A(i) = ActiveCell.Offset(4, 0).Value
ActiveCell.Offset(6, 0).Select

Next i

'grab co

Range("f22").Select

For i = 1 To n
For j = 1 To n
If i = j Then GoTo skip3

ActiveCell.Value = "F" & i & "->" & j
ActiveCell.Offset(0, 1).Select

'error check

If A(i) <= 0 Then
MsgBox "Error.  Input a positive non-zero Area", vbCritical, "Calculation Error"

End
End If

'Crossed
scxa(i) = xa(i) - xa(j)
scya(i) = ya(i) - ya(j)

scxb(i) = xb(i) - xb(j)
scyb(i) = yb(i) - yb(j)

sc(i) = (((scxa(i)) ^ 2 + (scya(i)) ^ 2) ^ 0.5) + (((scxb(i)) ^ 2 + (scyb(i)) ^ 2) ^ 0.5)

'UNcrossed
suxa(i) = xa(i) - xb(j)
suya(i) = ya(i) - yb(j)

suxb(i) = xb(i) - xa(j)
suyb(i) = yb(i) - ya(j)

su(i) = ((suxa(i)) ^ 2 + (suya(i)) ^ 2) ^ 0.5 + ((suxb(i)) ^ 2 + (suyb(i)) ^ 2) ^ 0.5

F(i, j) = (sc(i) - su(i)) / (2 * A(i))
ActiveCell.Value = F(i, j)
ActiveCell.Offset(1, -1).Select
Fsum = Fsum + F(i, j)

skip3:

Next j

ActiveCell.Value = "F Sum"
ActiveCell.Offset(0, 1).Select
ActiveCell.Value = Fsum
ActiveCell.Offset(2, -1).Select
Fsum = 0

Next i

'Export

If ToggleButton1.Value = True Then

Sheets("rad").Select
ActiveSheet.Range("h23").Select

For i = 1 To n
For j = 1 To n
```

```
If i = j Then GoTo skip2
ActiveCell.Value = F(i, j)
ActiveCell.Offset(1, 0).Select
skip2:
Next j
ActiveCell.Offset(1, 0).Select
Next i
ActiveSheet.Range("d23").Select
End If
End Sub
Private Sub Export_Click()
End Sub
Private Sub CommandButton3_Click()
Range("a20:iv65536").Clear
End Sub
Private Sub Label1_Click()
End Sub
Private Sub SpinButton1_Spinup()
TextBox1.Value = TextBox1.Value + 1
If TextBox1.Value < 2 Then
TextBox1.Value = 2
End If
If TextBox1.Value > 10 Then
TextBox1.Value = 10
End If
End Sub
Private Sub SpinButton1_Spindown()
TextBox1.Value = TextBox1.Value - 1
If TextBox1.Value < 2 Then
TextBox1.Value = 2
End If
If TextBox1.Value > 10 Then
TextBox1.Value = 10
End If
End Sub
Private Sub ToggleButton1_Click()
End Sub
Private Sub CheckBox1_Click()
End Sub
```

APPENDIX E – BEVANS-DUNKLE ITERATION CODE

When executed, the *Bevans-Dunkle Iteration Code* simultaneously solves for up to 10 surface radiosities [45]. The code is written in Microsoft Visual Basic 6.3 which is embedded in Microsoft Office Excel 2003. The following is an example of a four sided geometry input (typical for this study), where the view factors are imported from the *View Factor Calculator Code*, followed by the output of only 3 iterations and the code.

E.1 Input

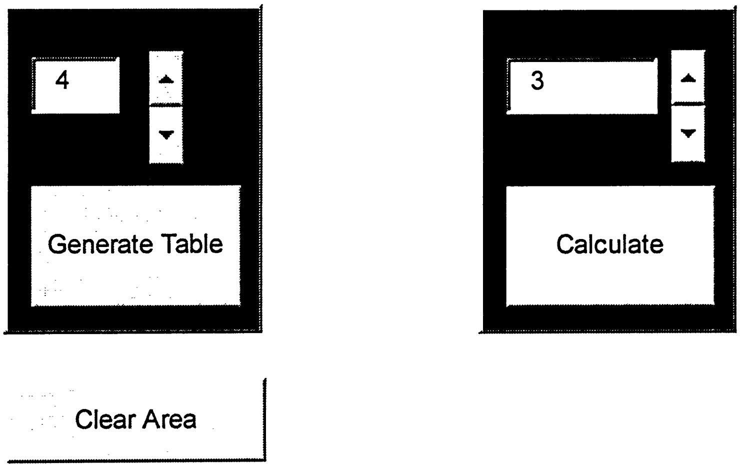

i		
1	T1 (K) =	302.59
	A1 (m^2) =	0.011844
	e1 =	0.84
2	T2 (K) =	298.1
	A2 (m^2) =	0.02958
	e2 =	0.792
3	T3 (K) =	293.41
	A3 (m^2) =	0.011844
	e3 =	0.84
4	T4 (K) =	298.1
	A4 (m^2) =	0.02958
	e4 =	0.792

i	Fi -> k	
1	F1 -> 2	0.048507045
	F1 -> 3	0.055930257
	F1 -> 4	0.895562698
2	F2 -> 1	0.019422496
	F2 -> 3	0.358587399
	F2 -> 4	0.621989184
3	F3 -> 1	0.055930257
	F3 -> 2	0.895560221
	F3 -> 4	0.048506868
4	F4 -> 1	0.358588391
	F4 -> 2	0.621989184
	F4 -> 3	0.019422425

E.2 Output

Ei	
E1 (W) =	475.3366973
E2 (W) =	447.745225
E3 (W) =	420.2257921
E4 (W) =	447.745225

	Iteration1
Side1 (i=1)	
J(k)*F(i->k)	21.718798
	23.503336
	400.98392
J(k)*F(i->k)sum	446.20606
(1-e)*J(k)*F(i->k)sum	71.392969
e*E1	399.28283
j1	470.67579
Side2 (i=2)	
J(k)*F(i->k)	9.141699
	150.68767
	278.49269
J(k)*F(i->k)sum	438.32206
(1-e)*J(k)*F(i->k)sum	91.170988
e*E2	354.61422
j2	445.78521
Side3 (i=3)	
J(k)*F(i->k)	26.325018
	399.2275
	21.718718
J(k)*F(i->k)sum	447.27123
(1-e)*J(k)*F(i->k)sum	71.563398
e*E3	352.98967
j3	424.55306
Side4 (i=4)	
J(k)*F(i->k)	168.77888
	277.27358
	8.2458501
J(k)*F(i->k)sum	454.2983
(1-e)*J(k)*F(i->k)sum	94.494047
e*E4	354.61422
j4	449.10827

	Iteration2		Iteration3
Side1 (i=1)		Side1 (i=1)	
J(k)*F(i->k)	21.6237233	J(k)*F(i->k)	21.647976
	23.7453619		23.75007
	402.20461		402.27746
J(k)*F(i->k)sum	447.573695	J(k)*F(i->k)sum	447.67551
(1-e)*J(k)*F(i->k)sum	71.6117911	(1-e)*J(k)*F(i->k)sum	71.628081
e*E1	399.282826	e*E1	399.28283
j1	470.894617	j1	470.91091
Side2 (i=2)		Side2 (i=2)	
J(k)*F(i->k)	9.14594904	J(k)*F(i->k)	9.1462654
	152.239378		152.26956
	279.340483		279.39108
J(k)*F(i->k)sum	440.725811	J(k)*F(i->k)sum	440.80691
(1-e)*J(k)*F(i->k)sum	91.6709687	(1-e)*J(k)*F(i->k)sum	91.687837
e*E2	354.614218	e*E2	354.61422
j2	446.285187	j2	446.30206
Side3 (i=3)		Side3 (i=3)	
J(k)*F(i->k)	26.3372569	J(k)*F(i->k)	26.338168
	399.675261		399.69037
	21.7848352		21.788781
J(k)*F(i->k)sum	447.797353	J(k)*F(i->k)sum	447.81732
(1-e)*J(k)*F(i->k)sum	71.6475764	(1-e)*J(k)*F(i->k)sum	71.650771
e*E3	352.989665	e*E3	352.98967
j3	424.637242	j3	424.64044
Side4 (i=4)		Side4 (i=4)	
J(k)*F(i->k)	168.857343	J(k)*F(i->k)	168.86318
	277.584559		277.59505
	8.2474851		8.2475471
J(k)*F(i->k)sum	454.689387	J(k)*F(i->k)sum	454.70578
(1-e)*J(k)*F(i->k)sum	94.5753925	(1-e)*J(k)*F(i->k)sum	94.578803
e*E4	354.614218	e*E4	354.61422
j4	449.189611	j4	449.19302

i	Ji (W)	Gi (W)	Qi (W)
1	5.577469	5.302269	0.275200091
2	13.20161	13.03907	0.16254643
3	5.029441	5.303948	-0.27450697
4	13.28713	13.4502	-0.163067484
		Q Sum (W) =	0.000172068

E.3 Code

```
Private Sub CommandButton4_Click()

Range("j20:iv65536").Clear

'E calculation
Dim i As Integer
Dim j As Integer
'Dim m As Integer
Dim t(10) As Double
Dim A(10) As Double
Dim em(10) As Double
Dim E(10) As Double
Dim F(10, 10) As Double
Dim EFsum(10) As Double
Dim EF(10, 10) As Double
Dim jj(10) As Double
Dim Eg(10) As Double
Dim jjsum(10) As Double
Dim q As Double
Dim qsum As Double

sigma = 0.0000000567

n = TextBox1.Value
Range("j23").Select

'Grab F values
ActiveCell.Offset(0, -2).Select

For i = 1 To n
For j = 1 To n
If i = j Then GoTo skip4:
F(i, j) = ActiveCell.Value
ActiveCell.Offset(1, 0).Select

skip4:
Next j
ActiveCell.Offset(1, 0).Select

Next i

'Calculate E
Range("j22").Select

ActiveCell.Value = "Ei"
ActiveCell.Offset(1, 0).Select

For i = 1 To n
t(i) = ActiveCell.Offset((2 * (i - 1)), -6).Value
A(i) = ActiveCell.Offset(1 + (2 * (i - 1)), -6).Value
em(i) = ActiveCell.Offset(2 + (2 * (i - 1)), -6).Value
ActiveCell.Value = "E" & i & " (W) ="
ActiveCell.Offset(0, 1).Select
E(i) = t(i) ^ 4 * sigma
ActiveCell.Value = E(i)
Eg(i) = E(i)
ActiveCell.Offset(2, -1).Select
Next i
ActiveCell.Offset(-2 * n, 3).Select

'Iteration
For m = 1 To TextBox2.Value
ActiveCell.Offset(-1, 1).Value = "Iteration" & m

For i = 1 To n
```

```
EFsum(i) = 0
jjsum(i) = 0

Next i

For i = 1 To n

'left side lable
ActiveCell.Value = "Side" & i & " (i=" & i & ")"
ActiveCell.Offset(1, 0).Select
ActiveCell.Value = "J(k)*F(i->k)"
ActiveCell.Offset(n - 1, 0).Select
ActiveCell.Value = "J(k)*F(i->k)sum"
ActiveCell.Offset(1, 0).Select
ActiveCell.Value = "(1-e)*J(k)*F(i->k)sum"
ActiveCell.Offset(1, 0).Select
ActiveCell.Value = "e*E" & i
ActiveCell.Offset(1, 0).Select
ActiveCell.Value = "j" & i
ActiveCell.Offset(-n - 2, 1).Select

For j = 1 To n
If i = j Then GoTo skip2:

EF(i, j) = Eg(j) * F(i, j)

ActiveCell.Value = EF(i, j)
ActiveCell.Offset(1, 0).Select

EFsum(i) = EFsum(i) + EF(i, j)
jj(i) = E(i) * em(i) + EFsum(i) * (1 - em(i))
Eg(i) = jj(i)
jjsum(i) = jjsum(i) + (jj(j) * F(i, j) * A(i))

skip2:

Next j

ActiveCell.Value = EFsum(i)
ActiveCell.Offset(1, 0).Select
ActiveCell.Value = EFsum(i) * (1 - em(i))
ActiveCell.Offset(1, 0).Select
ActiveCell.Value = E(i) * em(i)
ActiveCell.Offset(1, 0).Select
ActiveCell.Value = jj(i)

ActiveCell.Offset(2, -1).Select

Next i

ActiveCell.Offset(-n * (n + 5), 3).Select

Next m

ActiveCell.Offset(-1, 0).Value = "i"
ActiveCell.Offset(-1, 1).Value = "Ji (W)"
ActiveCell.Offset(-1, 2).Value = "Gi (W)"
ActiveCell.Offset(-1, 3).Value = "Qi (W)"

qsum = 0
For i = 1 To n
ActiveCell.Value = i
ActiveCell.Offset(0, 1).Select
ActiveCell.Value = jj(i) * A(i)
ActiveCell.Offset(0, 1).Select
ActiveCell.Value = jjsum(i)
ActiveCell.Offset(0, 1).Select
q = (jj(i) * A(i)) - jjsum(i)
ActiveCell.Value = q
```

```
qsum = qsum + q

ActiveCell.Offset(2, -3).Select
Next i
ActiveCell.Offset(0, 2).Select
ActiveCell.Value = "Q Sum (W) ="
ActiveCell.Offset(0, 1).Select
ActiveCell.Value = qsum

End Sub

Private Sub Label1_Click()
End Sub

Private Sub TextBox1_value()
End Sub

Private Sub Label2_Click()
End Sub

Private Sub SpinButton1_Spinup()

TextBox1.Value = TextBox1.Value + 1
If TextBox1.Value < 2 Then
TextBox1.Value = 2
End If
If TextBox1.Value > 10 Then
TextBox1.Value = 10
End If

End Sub

Private Sub SpinButton1_Spindown()

TextBox1.Value = TextBox1.Value - 1

If TextBox1.Value < 2 Then
TextBox1.Value = 2
End If
If TextBox1.Value > 10 Then
TextBox1.Value = 10
End If

End Sub

Private Sub CommandButton1_Click()
Range("a20:iv65536").Clear

Dim i As Integer
Dim n As Integer

Range("b22").Select
ActiveCell.Value = "i"
ActiveCell.Offset(1, 0).Select

'input loop
n = TextBox1.Value

For i = 1 To n

ActiveCell.Value = i
ActiveCell.Offset(0, 1).Select

ActiveCell.Value = "T" & i & " (K) ="
ActiveCell.Offset(1, 0).Select
ActiveCell.Value = "A" & i & " (m^2) ="
ActiveCell.Offset(1, 0).Select
ActiveCell.Value = "e" & i & " ="
ActiveCell.Offset(2, -1).Select
```

```
Next i

'View Factor
Dim k As Integer

n = TextBox1.Value
k = 1

Range("f22").Select
ActiveCell.Value = "i"
ActiveCell.Offset(0, 1).Select
ActiveCell.Value = "Fi -> k"
ActiveCell.Offset(1, -1).Select

'View Factor loop
For k = 1 To n

ActiveCell.Value = k
ActiveCell.Offset(0, 1).Select

For i = 1 To n
If i = k Then GoTo skip
ActiveCell.Value = "F" & k & " -> " & i
ActiveCell.Offset(1, 0).Select

skip:

Next i

ActiveCell.Offset(1, -1).Select
Next k

ActiveCell.Offset(-(n ^ 2), 1).Select
ActiveCell.Offset(1, 0).Select

'Borders
Range("b22:d" & 4 * n + 21).Select
Selection.Font.Bold = True
Selection.Borders(xlDiagonalDown).LineStyle = xlNone
Selection.Borders(xlDiagonalUp).LineStyle = xlNone
With Selection.Borders(xlEdgeLeft)
.LineStyle = xlContinuous
.Weight = xlThin
.ColorIndex = xlAutomatic
End With
With Selection.Borders(xlEdgeTop)
.LineStyle = xlContinuous
.Weight = xlThin
.ColorIndex = xlAutomatic
End With
With Selection.Borders(xlEdgeBottom)
.LineStyle = xlContinuous
.Weight = xlThin
.ColorIndex = xlAutomatic
End With
With Selection.Borders(xlEdgeRight)
.LineStyle = xlContinuous
.Weight = xlThin
.ColorIndex = xlAutomatic
End With
With Selection.Borders(xlInsideVertical)
.LineStyle = xlContinuous
.Weight = xlThin
.ColorIndex = xlAutomatic
End With
With Selection.Borders(xlInsideHorizontal)
.LineStyle = xlContinuous
.Weight = xlThin
.ColorIndex = xlAutomatic
End With
```

```
Range("f22:h" & (k * k) + 22 - 2 * k).Select
Selection.Font.Bold = True
Selection.Borders(xlDiagonalDown).LineStyle = xlNone
Selection.Borders(xlDiagonalUp).LineStyle = xlNone
With Selection.Borders(xlEdgeLeft)
.LineStyle = xlContinuous
.Weight = xlThin
.ColorIndex = xlAutomatic
End With
With Selection.Borders(xlEdgeTop)
.LineStyle = xlContinuous
.Weight = xlThin
.ColorIndex = xlAutomatic
End With
With Selection.Borders(xlEdgeBottom)
.LineStyle = xlContinuous
.Weight = xlThin
.ColorIndex = xlAutomatic
End With
With Selection.Borders(xlEdgeRight)
.LineStyle = xlContinuous
.Weight = xlThin
.ColorIndex = xlAutomatic
End With
With Selection.Borders(xlInsideVertical)
.LineStyle = xlContinuous
.Weight = xlThin
.ColorIndex = xlAutomatic
End With
With Selection.Borders(xlInsideHorizontal)
.LineStyle = xlContinuous
.Weight = xlThin
.ColorIndex = xlAutomatic
End With
Range("d23").Select

End Sub

Private Sub SpinButton2_Spinup()

TextBox2.Value = TextBox2.Value + 1

If TextBox2.Value < 1 Then
TextBox2.Value = 1
End If
If TextBox2.Value > 10 Then
TextBox2.Value = 10
End If

End Sub

Private Sub SpinButton2_Spindown()
TextBox2.Value = TextBox2.Value - 1
If TextBox2.Value < 1 Then
TextBox2.Value = 1
End If
If TextBox2.Value > 10 Then
TextBox2.Value = 10
End If

End Sub

Private Sub TextBox2_Change()
End Sub

Private Sub CommandButton2_Click()
Range("a20:iv65536").Clear
End Sub
```

REFERENCES

1. 2005 ASHRAE Fundamentals Handbook, 2005, Fenestration (F31), Atlanta, Georgia.

2. Wright, J.L., 1992, "Glazing System Thermal Analysis," CANMET, *Advanced Glazing System Laboratory*, VISION3, Minister of Supply and Services Canada, *University of Waterloo*, Waterloo.

3. Finlayson, E.U., Arasteh, D.K., Huizenga, C., Rubin, M.D., and Reilly, M.S., "WINDOW 4.0: Documentation of Calculation Procedures", *Energy and Environmental Division, Lawrence Berkeley Laboratory, Berkeley*, California.

4. Catton, I, 1978, "Natural Convection in Enclosures", *Proceedings of 6th International Heat Transfer Conference*, vol. 6, pp. 13-31.

5. Batchelor, G.K., 1954, "Heat Transfer by Free Convection Across a Closed Cavity between vertical boundaries at different temperatures", *Quart. Appl. Math. XII*, 209-233.

6. Wright, J.L. and Sullivan, H.F., 1989, "Natural Convection in Sealed Glazing Units: A Review", *ASHRAE Transactions: Technical and Symposium Papers*, vol. 95, part 1, pp. 592-603.

7. Wright, J.L., Jin, H., Hollands, K.G.T., Naylor, D., 2006, "Flow Visualization of Natural Convection in a Tall, Air-filled Vertical Cavity", *International Journal of Heat and Mass Transfer*, in press.

8. Korpela, S.A., Lee, Y., Drummond, J.E., 1982, "Heat Transfer Through a Double Pane Window", *Transactions of the ASME: Journal of Heat Transfer*, vol. 104, pp. 539-544.

9. Jin, H., 2000, "Flow visualization of Natural Convection in a Vertical Cavity", M.A.Sc. Thesis, *University of Waterloo*, Waterloo.

10. Lai, B., 2004, "An Interferometric Study of Free Convective Heat Transfer in a Double Glazed Window with a Between-Panes Venetian Blind", M.A.Sc. Thesis, *Ryerson University*, Toronto.

11. ElSherbiny, S.M., Raithby, G.D., Hollands, K.G.T., 1982, "Heat Transfer by Natural Convedtion across Vertical and Inclined Air Layers", *Transactions of the ASME Journal of Heat Transfer*, vol. 104, pp. 96-102.

12. Wright, J.L., 1996, "A Correlation to Quantify Convective Heat Transfer Between Vertical Window Glazings", *ASHRAE Transactions: Symposia*, pp. 940-946.

13. Aydin, O., 2000, "Determination of Optimum Air-Layer Thickness in Double-Pane Windows", *Energy & Buildings*, vol. 32, pp. 303-308.

14. Ostrach, S., 1972, "Natural Convection in Enclosures", *Advances in Heat Transfer*, vol. 8, pp. 161-227.

15. Ostrach, S., 1988, "Natural Convection in Enclosures", *Transactions of the ASME: Journal of Heat Transfer*, vol. 110, pp. 1175-1190.

16. Collins, M.R., and Harrison, S.J., 1999, "Calotimetric Measurements of the Inward-Flowing Fraction of Absorbed Solar Radiation in Venetian Blinds", *ASHRAE Transactions*, vol. 105, part 2, pp. 1022-1030.

17. Machin, A.D., Naylor, D., Harrison, S.J., Oosthuizen, P.H., 1997, "An Interferometric Study of the Effect of Louvers on Free Convection from an Isothermal Vertical Surface", *4th World Conference on Experimental Heat Transfer, Fluid Mechanics and Thermodynamics*, vol. 4, pp. 2175-2181.

18. Machin, A.D., 1997, "An Experimental Study of Free Convective Heat Transfer from a Vertical Flat Plate in the Presence of Louvers", M.E.Sc. Thesis, *University of Western Ontario*, London.

19. Machin, A.D., Naylor, D., Harrison, S.J., Oosthuizen, P.H., 1998, "Experimental Study of Free Convection at an Indoor Glazing Surface with a Venetian Blind", *International Journal of HVAC & R Research*, vol. 4, no. 2, pp. 153-166.

20. Ye, P., 1997, "Effect of Venetian Blinds on Overall Heat Transfer through Window Systems: A Finite Element Numerical Solution", M.Sc. Thesis, *Queen's University*, Kingston.

21. Phillips, J., Naylor, D., Oosthuizen, P.H., Harrison, S.J., 2001, "Numerical Study of Convective and Radiative Heat Transfer from a Window Glazing with a Venetian Blind", *International Journal of HVAC&R Research*, vol. 7, no. 4, pp. 383-402.

22. Phillips, J., Naylor, D., Harrison, S.J., Oosthuizen, P.H., 1999, "Free Convection from a Window Glazing with a Venetian Blind: Numerical Model Development", *Transactions of the CSME*, vol. 23, no. 1B, pp. 159-172.

23. Duarte, N., 2000, "An Experimental Study of Free Convective Heat Transfer from a Vertical Plate in the Presence of Heated Venetian Blinds", M.E.Sc. Thesis, *University of Western Ontario*, London.

24. Naylor, D., Duarte, N., Petryk, J., Machin, A.D., 2001, "Flow and Temperature Field Visualization of a Window with a Heated Louvered Blind", *Journal of Flow Visualization and Image Processing*, vol. 7, pp. 243-253.

25. Duarte, N., Naylor, D., Oosthuizen, P.H., Harrison, S.J., 2001, "An Interferometric Study of Free Convection at a Window Glazing with a Heated Venetian Blind", *International Journal of HVAC & R Research*, vol. 7, no. 2, pp. 169-184.

26. Oosthuizen, P.H., Sun, L., Harrison, S.J., Naylor, D., Collins, M., 2005, "The Effect of Coverings on Heat Transfer from a Window to a Room", *Heat Transfer Engineering*, vol. 26, no. 5, pp. 47-65.

27. Collins, M., Harrison, S.H., Naylor, D., Oosthuizen, P.H., 2002, "Heat Transfer from an Isothermal Vertical Surface with Adjacent Heated Horizontal Louvers: Numerical Analysis", *Transactions of the ASME Journal of Heat Transfer*, vol. 124, pp. 1072-1077.

28. Collins, M., Harrison, S.H., Naylor, D., Oosthuizen, P.H., 2002, "Heat Transfer from an Isothermal Vertical Surface with Adjacent Heated Horizontal Louvers: Validation", *Transactions of the ASME Journal of Heat Transfer*, vol. 124, pp. 1078-1087.

29. Naylor, D., Shahid, H., Harrison, S.J., Oosthuizen, P.H., 2006, "A Simplified Method for Modeling the Effect of Blinds on Window Thermal Performance", *International Journal of Energy Research*, in press.

30. Shahid, H. and Naylor, D., 2005, "Energy Performance of a Window with a Horizontal Venetian Blind", *Energy & Buildings*, vol. 37(8).

31. Garnet, J.M., Fraser, R.A., Sullivan, H.F., Wright, J.L., 1995, "Effect of Internal Venetian Blinds on Window Center-Glass U-Values", *Proceedings of the Window Innovations '95*, pp. 273-279.

32. Garnet, J.M., 1999, "Thermal Performance of Window with Inter-Pane Venetian Blinds", M.A.Sc. Thesis, *University of Waterloo*, Waterloo.

33. Yahoda, D.S. and Wright, J.L., 2004, "Heat Transfer Analysis of a Between-Panes Venetian Blind Using Effective Longwave Radiative Properties", *ASHRAE Transactions*, vol. 101, pp. 455-462.

34. Naylor, D. and Collins, M., 2004, "Evaluation of an Approximate Method for Predicting the U-Value of a Window with a Between-Panes Louvered Shade", *Proceedings of CHT-04, ICHMT International Symposium on Advances in Computational Heat Transfer*, Norway, pp. 1-10.

35. Huang, N., 2005, "Thermal Performance of Double Glazed Windows with Inter-Pane Venetian Blinds", M.A.Sc. Thesis, *University of Waterloo*, Waterloo.

36. Curcija, D., 1992, "Three-Dimensional Finite Element Model of Overall, Nighttime Heat Transfer Through Fenestration System", Ph.D. Dissertation, *University of Massachusetts*, Massachusetts.

37. Gray, D.D and Giorgini, A., 1975, "The Validity of the Boussinesq Approximation for Liquids and Gases", *International Journal of Heat and Mass Transfer,* Great Britain, Vol. 19, pp. 545-551.

38. Oosthuizen, P.H. and Naylor, D., 1999, "Introduction to Convective Heat Transfer Analysis", *McGraw-Hill*, New York.

39. FLUENT 6.2 Documentation, 2005, *Fluent Incorporated*, Evanston, Illinois.

40. Curcija, D. and Goss. W.P., 1993, "Two-Dimensional Natural Convection Over the Isothermal Indoor Fenestration Surface – Finite Element Numerical Solution", *ASHRAE Transactions*, vol. 99(1), pp. 247-287.

41. Celik, I., 1993, "Numerical Uncertainty in Fluid Flow Calculations: Needs for Future Research", *ASME Journal of Fluids Engineering*, vol. 115, pp. 194-195.

42. Roache, P. J., Ghia, K. N., and White, F.M., 1986, "Editorial Policy Statement on the Control of Numerical Accuracy", *ASME Journal of Fluids Engineering*, vol. 108, pp. 2.

43. Lai, B. and Naylor, D., 2003, "Numerical Study of Free Convective Heat Transfer from a Between-the-Glazing Venetian Blind Window Assembly", *Proc. 19th Canadian Congress of Applied Mechanics*, Calgary, Alberta, pp. 384-385.

44. Naylor, D. and Machine, A.D., 2001, "The Accuracy of Beam-averaged Interferometric Temperature Measurments in a Three-Dimensional Field", *Experimental Heat Transfer*, vol. 14, no. 3, pp. 217-228.

45. Bevans, J.T. and Dunkle, R.V., February 1969, "Radiation interchange within an enclosure", *ASME Journal of Heat Transfer*, vol. 82(1), pp. 1-7.

46. Hottel, H.C., 1967, "Radiative Transfer", *McGraw-Hill*, New York.